

**ADVANCED COMPONENTS OF MICROFLUIDIC SYSTEMS FOR  
BIOANALYTICAL APPLICATIONS**

by

**Minsoung Rhee**

A dissertation submitted in partial fulfillment  
of the requirements for the degree of  
Doctor of Philosophy  
(Chemical Engineering)  
in The University of Michigan  
2009

Doctoral Committee:

Professor Mark A. Burns, Chair

Professor David T. Burke

Associate Professor Joanna Mirecki-Millunchick

Associate Professor Michael J. Solomon

© Minsoung Rhee 2009  
All Rights Reserved

*In memory of Grandmother*

## Table of Contents

Dedication .....	ii
List of Tables .....	vi
List of Figures .....	vii
List of Appendices .....	x
Abstract .....	xi
 Chapter	
1. Introduction .....	1
1.1. Background .....	1
1.2. Organization of this dissertation .....	11
2. Drop Mixing in a Microchannel for Lab-on-a-chip Platforms .....	15
2.1. Introduction .....	15
2.2. Theoretical Modeling .....	17
2.3. Materials and Methods .....	20
Device Fabrication .....	20
Fluid Control and Image Acquisition .....	20
Image Processing .....	21
Simulation methods .....	21
2.4. Results and Discussion .....	22
Analytical Solution .....	22
Drop Mixing Simulations .....	32
Experimental Verification .....	33
2.5. Conclusions .....	36
Acknowledgement .....	37
Figures .....	38
Appendix .....	53
References .....	54
3. Membranous Bypass Valves for Discrete Drop Mixing and Routing in Microchannels .....	57



3.1. Introduction	57
3.2. Materials and Methods	58
Device Fabrication	58
Fluid Control and Image Acquisition	59
Image Processing	59
3.3. Results and Discussion	60
Membranous air bypass valves	60
The modified Péclet number	61
Drop mixing in three different regimes	62
Comparison of mixing experiment results with theoretical modeling	63
Membranous check valves for drop routing	64
3.4. Conclusions	66
Acknowledgement	66
Figures	67
References	76
4. Microfluidic Assembly Blocks	78
4.1. Introduction	78
4.2. Materials and Methods	80
Mold Fabrication	80
Block Fabrication	80
Block Assembly	81
Fluid Control and Image Acquisition	81
Cell Culture	82
4.3. Results and Discussion	83
Microfluidic Assembly Block Concept	83
Bonding and Sealing	84
Block Shapes	86
Applications	88
4.4. Conclusions	90
Acknowledgement	90
Tables	91

Figures .....	93
Appendix .....	101
Bonding Techniques .....	102
Block Shapes .....	102
Visualization of microfluidic laminar flows .....	103
Tables .....	105
Figures .....	107
References .....	116
5. Digital Pneumatic Microprocessors for Microfluidic	
Large-Scale Integration .....	118
5.1. Introduction .....	118
5.2. Concepts .....	119
5.3. Materials and Methods .....	121
5.4. Results and Discussion .....	122
5.5. Conclusions .....	127
Figures .....	129
Appendix .....	135
Logic Pumping and Routing .....	135
Portability .....	136
Tables .....	137
References .....	139
6. Conclusions .....	140

## List of Tables

Table 4-1. Exemplary Standard Microfluidic Assembly Blocks in the study .....	91
Table 4-S1. Various bonding strategies for assembly of MAB .....	105
Table 4-S2. Various block shapes and their assembly .....	106
Table 5-S1. Truth Table for Pneumatic NOR Logic Gate .....	137
Table 5-S2. Truth Table for Pneumatic NAND Logic Gate .....	137
Table 5-S3. Truth Table for Pneumatic XNOR Logic Gate .....	138
Table 5-S4. Truth Table for Pneumatic XOR Logic Gate .....	138
Table A-1. Summary of the statistical translocation properties of six polymers characterized at 25.0°C .....	159
Table B-1. Nanopores from various preparation procedures .....	183

## List of Figures

Figure 2-1. Mixing Model. ....	38
Figure 2-2. Analytical Quantification of Mixing. ....	40
Figure 2-3. Velocity profiles for a drop of $\varepsilon=7$ . ....	41
Figure 2-4. COMSOL Simulation. ....	42
Figure 2-5. Simulated interlayering progress for $Pe^*=2000$ and $\varepsilon=7$ . ....	43
Figure 2-6. Mixing Progress. Concentration changes in two domains ....	44
Figure 2-7. Calibration curve for the trypan blue 0.4% solution ....	45
Figure 2-8. Photo of the mixing channel and the MBV filled with the blue solution ..	46
Figure 2-9. The use of MAB to coalesce two drops ....	47
Figure 2-10. Convective Mixing Progress ( $Pe^*=132$ ). ....	48
Figure 2-11. Dispersive Mixing Progress ( $Pe^*=6$ ) ....	49
Figure 2-12. Diffusive Mixing Progress ( $Pe^*=0.4$ ) ....	50
Figure 2-13. Comparison between a straight and a curved channel ....	51
Figure 2-14. Mixing time comparison among theoretical predictions, simulations, and experimental results ....	52
Figure3-1. A schematic of the use of 2D MBV to coalesce two drops. ....	67
Figure3-2. 3D MBV ....	68
Figure3-3. The aspiration rate measurements with various membrane interfacial area and the applied vacuum strength ....	69

Figure3-4. Average concentration changes in left and right .....	70
Figure3-5. Mixing time comparison among theoretical predictions, simulations, and experimental results .....	71
Figure3-6. Membranous Valve at different pressures applied .....	72
Figure3-7. Membrane Check Valve. ....	73
Figure3-8. Selective Routing. ....	74
Figure3-9. A plot of flow rates against the internal pressure, depending on the shape of membranes. ....	75
Figure 4-1. A schematic of the basic concept of the MAB approach. ....	93
Figure 4-2. Microfluidic Assembly Blocks .....	94
Figure 4-3. The effect of inter-block gaps on the evaporation rate. ....	95
Figure 4-4. The cross alignment key system .....	96
Figure 4-5. Demonstration of the valve module working in an assembled device. ....	97
Figure 4-6. <i>E. Coli</i> cell culture in the MAB assembled device. ....	98
Figure 4-7. Exemplary systems for complex biochemical assays. ....	99
Figure 4-8. Large-scale Assembly .....	100
Figure 4-S1. The overall fabrication process for MAB .....	107
Figure 4-S2. Plot of the number of SU-8 2025 spin coating .....	108
Figure 4-S3. The distribution of block thicknesses .....	109
Figure 4-S4. Inter-block bonding by capillary effect .....	110
Figure 4-S5. Schematics of the devices .....	111

Figure 4-S6. The cross alignment block-and-base system	112
Figure 4-S7. The channeled base system	113
Figure 4-S8. Demonstration of diffusive mixing in laminar flows	114
Figure 4-S9. The design of the two-layer valve module	115
Figure 5-1 Concepts and the fundamental Pneumatic Inverter	129
Figure 5-2 Various Pneumatic Logic gates.	130
Figure 5-3. Advanced Pneumatic Circuits	131
Figure 5-4. Various digital pneumatic microprocessors	132
Figure 5-5. Programmable digital pneumatic microprocessors	133
Figure 5-6. Specialized microprocessors	134
Figure 5-S1. Membranous Pump	136
Figure A-1. A molecular model of translocation events	160
Figure A-2. A single-base mismatch abolishes the binding of an oligonucleotide to a tethered DNA strand within the engineered nanopore	161
Figure A-3. Schematic representation of the molecular components and processes employed for synthesis of transmembrane protein rotaxanes	162
Figure B-1. Early prototype nanopore device.	184
Figure B-2. Ion beam sculpting to make nanopores	185
Figure B-3. TEM images of a silicon oxide nanopore of the starting size	186
Figure B-4. Illustration of the method for fabrication of MWNT membranes.	187

## List of Appendices

A. Nanopore Sequencing Technology: Research Trends and Applications .....	144
A.1 Introduction .....	144
A.2 Molecular Discrimination Using Nanopores .....	146
A.3 Modifications of Nanopore Detection .....	151
A.4 Conclusions .....	156
Tables .....	159
Figures .....	160
References .....	163
B. Nanopore Sequencing Technology: Nanopore Preparations .....	169
B.1 Introduction .....	169
B.2 Protein Nanopore Preparation .....	170
B.3 Synthetic Nanopore Fabrications .....	174
B.4 Conclusions .....	182
Tables .....	183
Figures .....	184
References .....	188

## **ABSTRACT**

### **ADVANCED COMPONENTS OF MICROFLUIDIC SYSTEMS FOR BIOANALYTICAL APPLICATIONS**

**by**

**Minsoung Rhee**

Chair: Mark A. Burns

The need for detailed understanding of fundamental and advanced components towards the widespread use of microfluidic systems are addressed in this dissertation. First, to understand mixing in microfluidic lab-on-a-chip systems, discrete droplet mixing in microchannels was examined using mathematical modeling, simulations, and experiments. The microfluidic mixing occurs in three distinct regimes (diffusion-dominated, dispersion-dominated, and convection-dominated) depending on the Péclet



number and the droplet dimensions. Using mathematically developed asymptotic curves, it was possible to predict the mixing time and required channel distance for any Péclet numbers. The mixing of typical drops (~3000um long) in microchannels (100~500um) resulted in mixing times of 0.001~10000 seconds depending on the drop velocity. Simulations and experiments of the mixing of two discrete drops agreed well with the theoretical limits.

Second, novel microfluidic components for discrete drop mixing and routing in lab-on-a-chip systems have been developed. The membranous air bypass valve (MBV) in PDMS allows air to pass through but stops liquid. Using two-dimensional and three-dimensional MBVs, the trapped air between discrete drops was rapidly removed at the aspiration rate of ~65nL/s. MBVs with semicircular membranes could also act as fluidic diodes that allow only unidirectional flow at operating pressures of 12~24kPa. Complex drop routing was possible with multiple fluidic diodes embedded.

Third, a user-friendly device construction methodology using prefabrication of microfluidic assembly blocks in PDMS was introduced to allow users to build custom microfluidic systems without any fabrication expertise. Complete sealing was done by

applying adhesive materials such as the PDMS curing agent and UV-curable glues between blocks. Using the square blocks of the size of  $16\text{mm}^2$ , we demonstrated common microfluidic applications including laminar flow development, valve control, and cell culturing.

Finally, digital pneumatic microprocessors have been developed as universal on-chip control platforms to multiplex a single pneumatic input. Logic components such as AND, NOR, flip-flops, and shift-registers were constructed and linked to compute, store, and parallelize serially-encoded input signals. The resulting parallel outputs were used to control multiple valves, pumps, channels, and chambers, independently. By significantly reducing the need for external controllers, digital pneumatic microprocessors could facilitate the widespread use of microfluidic systems.

# **Chapter 1**

## **Introduction**

### **1.1 Background**

Microfluidics has proven its unique advantages that have attracted researchers in biology, chemistry, and medicine, including reduced reagent consumption, favorable reaction kinetics, ability to rapidly prototype devices, high throughput potentialities, the possibility of integration and automation, and decreased analysis time. Microfluidics can also provide more realistic in vitro environments for small-scale biological species of interest. In specific, microstructures offer the length scales comparable to the intrinsic dimensions of cells and tissues. One can physically isolate single cells in microfluidic structures while allowing them to exchange small molecules between the cells and the surrounding fluids.

Besides its most obvious characteristics from the miniaturized scale, microfluidics also exploits less obvious characteristics of fluids in microchannels, such as laminar flow and surface effects. In microfluidic channels, the fluid flow is dominated by viscous dynamics and is thus laminar. Adjacent streams of fluids in microchannels flow in parallel, and the mixing occurs only by diffusion across the interface between the fluids. This laminar flow behavior allows for the generation of precise concentration

gradients that are perpendicular to the fluid flow and have sufficient temporal and spatial stability. While laminar flow is advantageous in many microfluidic applications such as separation, sorting, and cell studies, it can also be a nuisance in other processes where fast mixing is necessary for rapid reaction.

### **Current Technology**

Since the seminal works by Manz in the early 1990s, two decades of microfluidic research have yielded a wealth of techniques to improve biomedical assays through both the miniaturization of conventional macroscale techniques, as well as the development of novel microfluidic analytical methods.

In recent years, microfluidic systems have been increasingly used in biomedical and biological applications. Microfluidics offers a wide range of interesting and new applications, starting from alternatives of conventional bench-top analysis systems to novel in-vivo applications, particularly for drug delivery. Most recently, microfluidic-based approaches made a significant impact in the area of chemical synthesis especially in organic and medicinal chemistry. Microparticles with various sizes and shapes can be produced either using specialized microfabrication techniques or by controlled operation in microfluidic device. Combined with proper coatings, such microparticles provide effective site-specific delivery, especially for peptide and protein-based drugs. Microfluidic technologies are also powerful tools for tissue engineering. The use of microfluidic technologies in tissue engineering ranges from transplantable microfabricated constructs to fabrication of physiological mockups for understanding the biology of organs.

Nevertheless, the earliest and most developed applications of microfluidic

technologies have been in analysis primarily focused on biological analyses. Over the past decades, genomic research has observed powerful microfluidic techniques with applications ranging from genotyping to clinical diagnosis. Since the completion of human genome sequencing, there has been an increasing demand for rapid, high throughput genetic analysis throughout microfluidic formats. The most widespread analytical microfluidic systems are the lab-on-a-chip devices built to analyze DNA and RNA. Such devices typically rely on on-chip polymerase chain reaction (PCR) and electrophoretic separation for analysis.

As one of the key components in most genetic assays, PCR has been studied extensively and successfully incorporated in microsystems. Enhanced heat transfer of extremely small sample volumes allows for efficient thermocycling. Other genetic analysis techniques, including DNA sequencing, reverse transcript PCR, various enzyme reactions, and capillary electrophoresis (CE) have also been successfully performed in microfluidic devices. Significant advances in pathogen detection can be achieved from microfluidic portable devices. For instance, a recently developed lab-on-a-chip device for the detection of influenza integrates multiple analytical processes for sequential operations including valves for fluidic handling, computerized temperature control with integrated heaters for PCR, a reaction chamber for restriction endonuclease digestion and a separation channel for electrophoresis. Recently, integrated microsystems that are capable of quickly collecting genetic information from raw biological samples have been also developed. Microfluidics has also found its extended capability as being a platform for proteome profiling. Microfluidic technologies also have the potential to revolutionize forensic DNA testing with state-of-the-art analytical technology. On-chip PCR would prove to be instrumental in future DNA sequencing and genotyping devices that hold a

great promise in the future of genomic research in the post-genome era.

### **Future Devices**

The microfluidic technological impact has long been anticipated. Although there is no doubt about the advantages of miniaturization, the field is arguably not where it was envisioned ten years ago. Although a few microfluidic systems are now commercially available for applications such as DNA analysis, protein crystallization, and performing simple chemical reactions, the field continues to search for a high impact application, and remains a vibrant research area with researchers tackling the challenges hindering its widespread routine use.

For instance, a gap typically exists between the technology developers mostly in engineering and potential users especially in the life sciences. To date, most microfluidic systems have been optimized for one specific task, and reconfiguration is generally not possible. However, current custom microfluidic devices are relatively expensive to manufacture due to the equipment and expertise required. Additionally, these devices are competing with conventional macro-scale platforms with which most potential users are accustomed. The high cost and the level of expertise required for microfabrication thus deters non-expert users from using microfluidic systems. Recently, a unique assembly approach for microdevice construction has been proposed to facilitate the use of microfluidic systems by non-experts such as clinicians, cell biologists, police officers or public health officials. Non-expert users can assemble devices with the blocks in minutes without the need for expensive clean-room facilities, using pre-fabricated microfluidic assembly blocks on plain glass slides.

Healthcare is considered one of the most promising areas among various microfluidic applications ever since the advent of bioanalytical microsystems. New types of microfluidic bioassay monitoring patients' responses to medical treatments have been actively developed. In addition to such monitoring tools for therapy, integrated microsystems equipped with sensory and actuation capabilities can perform more efficient drug delivery than conventional drug intake. Fully integrated microfluidic drug delivery systems are believed to revolutionize the health-care industry.

Development of simple assays for physicians' and home uses is another important task that the microfluidics field faces ahead. For healthcare alone, the potential market for simple and inexpensive diagnostics seems to be incredibly promising. There has been tremendous need in global healthcare for diagnosing communicable and non-communicable diseases worldwide. Microfluidics is an enabling technology that will create opportunities for point-of-care (POC) devices that can perform analyses hitherto possible only with roomful equipment in the clinical laboratory. Such POC microfluidic devices can facilitate early and accurate diagnoses and also improve the epidemiological surveillance of diseases. In the future, healthcare providers will shift from treating diseases to anticipating and preventing them. Home tools with complex diagnostic capabilities will expedite the personalization of medical care. Consequently, microfluidic platforms are the most plausible technology for such a paradigm shift in health care.

Environmental monitoring is another important application that can benefit from the use of microfluidic devices. The anticipated market for portable devices to monitor air or soil is ever increasing due to the recent attention on environmental issues. For example, portable microfluidic sensors can be customized to measure pH, the activity of microbes, the amount of nutrients (or contaminants), and the level of various ions from soil samples.

The same principle of sensory systems can be applied to chemical weapon detection as well.

The food industry has been seeing increasing demand for maintaining quality and safety of food. Portable microfluidic devices are a natural fit to perform various analysis tasks for food safety because the analysis must be done even in most remote settings or all around in our everyday life such as home, at work, and even at restaurants. Recent concerns on human-communicable diseases such as avian influenza and mad cow disease even make food and agriculture monitoring more important. Consequently, more food scientists are now alert to the recent developments in microfluidic sensors.

### **Integration**

For widespread use of microfluidic devices, part of the technological challenges lies in sample pre-treatment. Running real-life fluid samples like blood, however, brings more problems than using a purified laboratory solution. Besides blood, the use of non-invasive samples such as saliva and urine are also pursued for microfluidic analyzers. Since clinical and environmental samples are often complicated, the samples must be prepared in advance before introduced into the device. Automation and integration of the sample preparation steps in the microfluidic device is thus preferred. Pretreatment steps to be integrated typically include sampling, extraction, filtration, pre-concentration, and dilution. However, development of effective devices for sample pretreatment or fractionation still remains a challenge to the practical application of micro-analytical systems.

Although microfluidics has seen the rapid development of versatile structures including valves, mixers, and pumps, there have been no standardized generic



components that can be utilized in most of the microfluidic devices. Moreover, the realization of complex microfluidic systems also requires the integration of such generic components into complete, functional systems. A fully integrated microfluidic device is expected to perform rapid and reproducible measurements since it may eliminate the need for error-prone human operations and huge external control equipment; exclude potential environmental contamination; and reduce analysis time. More importantly, such integration may allow for high throughput analysis through parallelized or multiplexed devices with greatly reduced cost per analysis. Nevertheless, integration and packaging of a number of independent components into a single system is not a trivial task. The full integration not only requires well functioning modular components but also solid communications between individual components. Another barrier for full integration is to miniaturize electrical and thermal controls. When electrokinetic flows, electromechanical pumps/valves, or temperature controls are required, one should consider that the nearby high voltages or thermal distribution can cause unfavorable local reactions. Hence, proper thermal and electrical isolation is important for microfluidic integration.

### **Automation**

Automation also remains a substantial hurdle for microfluidic systems. For integrated devices with minimal human involvements, automation is necessary. Since many potential microfluidic applications require a large number of pneumatic valves, pumps, and other components, many of which require complex control systems, the need for complex control imposes practical limits on the widespread use of integrated microfluidic systems. Other than conventional pressure-driven flow or electroosmosis flow, a novel scheme for the movement of fluids will be revolutionary, particularly if

they are easily integrable and inexpensive to build. Automation of sample introduction can further reduce possible complications caused from the interface between the macroscopic and the microscopic. Using robotic interfaces that transfer fluids from standard microtiter plates into their microfluidic chips has been proposed, but it is limitedly applicable to specific devices with matching ports. Interfacing microfluidic devices with existing laboratory instrumentation and equipment may prove advantageous to develop standardized fluidic platforms that are simple and versatile enough to enable their use in both academic and industrial environments.

## **Detection**

Due to the reduced analysis volume of samples, the sensitivity of microfluidic detection also becomes another crucial challenge. The reduction in analysis volumes often yields insufficient numbers of analytes to detect, compromising the sensitivity and performance. The inflated surface-to-volume ratio in microfluidic devices is also problematic for detection since most biological samples tend to non-specifically bind to microchannel surfaces, deteriorating the capability of differentiation in detection. Specialized coating of microfluidic channels is thus required to reduce non-specific adhesion to improve analysis. In addition, the complicated optical interfacing and expensive detecting instrumentation limit the capability of microfluidic devices. Hence, there is a growing interest to couple and integrate optical components into microfluidic devices for biotechnology and analytical chemistry. Both sensitivity and scalability must be considered at the same time to choose the detection method for microfluidic devices. Whereas microfluidics has been successful in integrating fluidic and reaction tasks on a chip, major optical components including the light source, sensors and lenses have

remained off the chip, mainly because such detection schemes required huge instruments that were not easily scalable to microscale dimensions. Optofluidics is thus a burgeoning field to combines optics and microfluidics on the same integrated chip. With the advances in optical spectroscopy and microscopy, it will be possible to integrate sensitive micro-optical components in microfluidic platforms.

Recently, there have been various attempts to manufacture microfluidic large-scale integration (mLSI) systems with thousands of integrated micromechanical valves and control components. The mLSI enables hundreds of independent assays to be performed in parallel to quantitatively measure the reproducibility of biochemical experiments. For instance, a large-scale integrated microfluidic chip recently developed can perform 256 independent experiments in separate micro-chambers that are individually addressable using integrated pneumatic valves. However, the need for a large number of dedicated external control lines imposes practical limits on the scalability of integrated microfluidic systems and such large-scale systems are still missing solid sample preparation and read-out skills. More research has to be directed towards reliability of microfluidic large-scale integrated systems for different quantitative tests.

### **User-friendliness**

Unlike the fully integrated high throughput systems, there are needs for such devices that are typically used to provide extremely specific and simple information about a small number of samples. Widespread use of these simple devices for point-of-care applications is another major target of truly portable microfluidic devices. Microfluidic devices integrated into a hand-held format will be extremely useful where proper laboratory access is not available or ultra-fast on-site analysis time is required. For

instance, the use of microfluidic devices in developing countries poses more challenges than that in developed countries with well-equipped laboratories does. Military and border patrols, forensic tests, and personal bedside healthcare are other examples that may benefit from those point-of-care devices. The devices must reliably perform under various constraints such as cost limitation, absence of trained workers, lack of electricity, and unfavorable weather conditions. For such point-of-care devices, a user-friendly interface is a key to pervasive use. These devices must have simple macroscopic inputs that take real-world samples in their intact form and should employ user-friendly diagnostic result displays such as a simple yes/no indicator.

### **Information**

Microfluidics holds tremendous potentials to enrich the analysis on a variety of chemical and biomedical information that can be disseminated to the individual. Macro-scale analysis systems for extracting such information have demonstrated their utility for decades but their use was constrained within well-equipped laboratories since they are expensive, large and difficult to operate. As a result, the analysis information has been physically isolated and temporally infrequent. However, future microfluidic devices would rather empower health-care workers and patients with important health-related information even in extremely poor settings. Considering the wide range of potential chemical and biomedical tests, microfluidic analysis systems in the future can be high-density and frequent, resulting in pervasive analysis information. There will be thus strong demands for software that can manage the vast amount of information produced by those ubiquitous microfluidic systems. Consistently, informatics will extend its viability to the ever increasing microfluidic information to analyze significant patterns

and other statistical data in the information.

## **Summary**

Microfluidics brings the advantages of small volumes of fluids, reagents, and waste. Besides those obvious characteristics, the field however has very strong backgrounds in multidisciplines. The phenomena in microfluidics involve many unique aspects of physics, chemistry and biology, which originates from the small scales. Although integration of many microfluidic components has shown the possibility of the advent of revolutionary microfluidic systems, the existing technologies for pumps, valves, and on-chip reagent storage are also in need of improvement.

The eventual availability of cheap microfluidic assay systems will produce an ever-increasing amount of raw data for health care, agriculture, and environmental studies. Storage, manipulation, and processing of those data will become another daunting task and a focus of future research, moving the center of microfluidic research from microfabrication engineers to mathematicians and geneticists. The field of microfluidics just has left its infancy. The innate advantages of microfluidics are too attractive to ignore; undoubtedly, we will see microfluidic devices successfully replace conventional bench-top systems in the near future.

## **1.2 Organization of the dissertation**

In chapter 2, fundamental mixing in microchannels is presented by theory, simulations and experiments for discrete drops. The mixing occurs in three different

regimes (diffusion-dominated, dispersion-dominated, and convection-dominated) depending on the Péclet number ( $Pe$ ) and the drop dimensions. Introducing the modified Péclet number ( $Pe^*$ ), we show asymptotic curves that can be used to predict the mixing time and the required distance for mixing for any Péclet numbers ( $Pe^*$ ) and any droplet dimensions. Simulations of the mixing experiments using COMSOL are also performed for further verification. In the experimental work, a PDMS microchannel with a membrane air bypass valve is presented to facilitate droplet mixing by removing the air between drops. This approach enables precise control of the mixing and merging site. Experimental, simulation, and theoretical results are compared and verify that mixing can occur in fractions of a second to hours, depending on the parameters used.

In Chapter 3, extended forms of novel microfluidic components for discrete drop mixing in microchannels are presented. The membranous air bypass valve (MBV) in PDMS allows air to pass through but stops liquid. Using the two-dimensional and three-dimensional MBVs, the trapped air between the discrete drops is aspirated so that the sequentially arranged drops can come in contact. The merged drop then moves at a set velocity to achieve mixing. Modifications of MBVs for additional functionalities are further investigated. With semicircular membranes, MBVs act as fluidic diodes that allow only unidirectional flow at certain threshold pressures. Such a diode-like functionality enables complex drop and flow routing.

Chapter 4 describes a novel assembly approach for microdevice construction using prefabricated microfluidic components. Although microfluidic systems are convenient platforms for biological assays, their use in the life sciences is still limited mainly due to the high-level fabrication expertise required for construction. This approach involves prefabrication of individual microfluidic assembly blocks (MABs) by

fabrication experts and the following assembly by non-expert users who can assemble the blocks on plain glass slides to build their devices in minutes without any fabrication steps. Exemplary assembled devices demonstrate common microfluidic applications including laminar flow development, valve control, and cell culture.

Finally, in Chapter 5, unique designs of microfluidic digital pneumatic circuits are presented. These “pneumatic digital microprocessors” operate on serially encoded command signals and produce parallel outputs that can be utilized to control various pneumatic active components. Pneumatic circuits comprise inverters, flip-flops, logic gates, latching circuits, and shift registers; such circuits are then integrated to form advanced microprocessors to perform complex parallel operations of numerous individually addressable valves while the number of control inputs is fixed at one. In comparison with their electronic counterparts, several straightforward analogies are available. Equipped with computational capability, the processors accept serially encoded commands as inputs and produce parallel outputs to address multiple valves, pumps, channels, or chambers, independently. By significantly reducing the need for external controllers, the pneumatic digital microprocessor can be a potent universal on-chip platform to facilitate ubiquitous use of microfluidic devices.

In Appendix A, a detailed investigation on nanopore sequencing technology is available. Nanopore sequencing that is one of the most promising technologies being developed as a cheap and fast alternative to the conventional Sanger sequencing method. Protein or synthetic nanopores have been used to detect DNA or RNA molecules. Although none of the technologies to date has shown a single-base resolution for *de novo* DNA sequencing, there have been several reports of alpha-hemolysin protein nanopores being used for basic DNA analyses, and various synthetic nanopores have been fabricated.

This appendix will examine current nanopore sequencing technologies including recent developments of new applications. Continuously, current technologies to prepare a variety of nanopores are reviewed in Appendix B. As of today, there have been two general approaches to prepare nanopores for nucleic acid analysis. Organic nanopores such as *alpha-hemolysin* pores are commonly used for DNA analysis, while synthetic solid-state nanopores have been developed using various conventional or non-conventional fabrication techniques. In particular, synthetic nanopores with smaller sizes than *alpha-hemolysin* pores have been prepared primarily by electron beam-assisted techniques, exhibiting more robustness and better dimensional adjustability. This appendix will review current methods of nanopore preparation, ranging from organic pore preparations to recent developments of synthetic nanopore fabrications.



## Chapter 2

### Drop Mixing in a Microchannel for Lab-on-a-chip Platforms

#### 2.1 Introduction

Over the past decade, microfluidic systems have been widely used for various biochemical reaction operations due to the low consumption of reagents, more precise control of reactions, and high-throughput fabrication of the devices [1-3]. Biochemical processes such as drug delivery, sequencing, enzyme reactions and protein folding often involve reactions that require mixing of reactants for initiation. Sufficiently rapid mixing in such platforms is thus key to the effective functioning of the microfluidic devices [2, 4]. However, in many microfluidic applications, rapid mixing is a major challenge because of the laminar and uniaxial flow by the low Reynolds Number (Re) flow (typically  $Re < 100$ ). These low values of Re affirm that viscous forces overwhelm inertial forces, and the resulting mixing of concurrent reagent streams is purely diffusive. Despite the scale of microfluidic devices, the time for this pure diffusive mixing is often unacceptably long. For instance, for proteins with diffusion coefficients on the order of  $D = 10^{-7} \text{ cm}^2/\text{s}$ , mixing by diffusion across a  $200 \text{ }\mu\text{m}$  channel would result in a mixing time of  $t = w^2/D$  or  $\sim 0.5 \text{ h}$ . This slow transport time scale has become a bottleneck for many

high-throughput microfluidic tests and has negative implications on microfluidic device fabrication.

There are many designs of mixing systems to alleviate such limitations. A basic T-shaped micromixer was used for the measurement of analyte concentrations of a continuous flow system [5, 6]. Likewise, a similar Y-mixer was adopted to investigate the nonlinear diffusive mixing of fluorescein [7]. Micromixers can be used as sensors in environmental monitoring [8] or in reaction kinetics studies [9, 10]. Rapid mixing in the range of microseconds is required in some reaction studies or to understand the early events of protein folding [11, 12]. Mixing is also one of the essential functions in lab-on-a-chip (LOC) platforms for complex chemical reactions [3, 13, 14].

A variety of micromixers to accelerate mixing have been described in the literature [15, 16]. From the viewpoint of enhancing the mixing process, micromixers can be categorized as passive or active. Passive micromixers rely on geometrical properties of channel shape to induce complicated fluid-particle trajectories or to increase interfacial areas and thus greatly enhance mixing. The mixing process in these systems is dominated entirely by diffusion or chaotic advection. Various passive mixers that have been reported include techniques such as hydrodynamic focusing [17], multi-lamination [18-20], packed-bed mixing [21, 22], injection [23], chaotic advection [24-26], and droplet mixing [27-29]. Passive micromixers often require deliberate fabrication of channel geometry, but do not require external actuators. The resulting passive structures are robust in operation and easily integrated in a more complex lab-on-a-chip system. In contrast, active micromixers accommodate one or more of the externally-generated disturbance forces such as pressure [30], temperature [31], electrokinetics [32], magnetics [33] and acoustics [34]. Accordingly, the structures of active micromixers must incorporate the

corresponding external sources and typically require more involved fabrication processes than passive mixers although the resulting devices usually perform better.

Mixing in microfluidic systems occurs not only in a continuous flow but also between two drops in a discrete or batch operation. While most micromixers are used in continuous-flow systems, several studies have been reported on microfluidic mixing in batch systems [3, 13, 14, 35-38]. As opposed to continuous-flow systems, mixing in batch systems can be enhanced by convection [39]. During the course of drop transportation, the internal circulation streamlines of liquid in a moving discrete drop [40] allows convective mixing as well as molecular diffusion. In addition, the isolated volume helps reduce axial dispersion along the channel and contamination between sample volumes [28].

I present in this chapter a quantitative study on discrete drop mixing in microchannels. Operational parameters such as drop length, channel dimensions, and drop velocity are investigated theoretically to estimate the effective mixing time and the corresponding mixing channel length. Three different regimes are classified and explored in detail: diffusion dominates convection, convection dominates diffusion, and both convection and diffusion are important. The theoretical model is then verified using COMSOL Multiphysics simulations and tracer dye experiments.

## **2.2 Theoretical Modeling**

We assume a pressure driven flow in a slit-type microchannel ( $w \gg d$ ) (Figure 2-1a, 1b). Because of this aspect ratio, we can further assume that the mass transfer is independent of the channel width direction ( $z$ -axis) and thus use a two-dimensional

model. The liquid inside a discrete drop moving in a microchannel experiences internal circulation within itself [40, 41] (Figure 2-1c). The internal circulation of liquid plays a decisive role in the exchange of solutes between drops and thus enhances mixing as a number of experimental and computational studies have shown [42-44]. For computational simplicity, we assume that the viscosity and density of the liquid are constant over the volume. Additionally, the diffusion coefficient of the solute in the liquid is assumed to be constant and axis-independent.

Drops in the microchannel can be oriented in two different ways: sequential (Figure 2-1a) or parallel (Figure 2-1b). Most of the continuous-flow mixing systems have liquid samples that flow parallel at their inlets although the orientation can be altered using channel geometries [24, 45]. For discrete drop systems, sequential drop arrangement is usually preferred in order to maximize the use of interlayering produced by internal circulation [39]. The striations produced by the circulation create diffusion distances that are a fraction of the channel depth thus greatly reducing diffusion times. However, for parallel drops, no such interlayering occurs and the mixing is inefficient [46]. Consequently, for this study, we will only consider sequential drops.

When the combined sequential drops move along the channel, the solute can either be transported convectively or diffusively to a region of different concentration. The governing transport equation for the slit-channel model is simplified as follows [39].

$$\frac{\partial c}{\partial t} + U(y) \frac{\partial c}{\partial x} = D \left( \frac{\partial^2 c}{\partial x^2} + \frac{\partial^2 c}{\partial y^2} \right) \quad (2.1)$$

$$\text{where } U(y) = 0.5U_d \left( 1 - 3 \left( \frac{y}{d/2} \right)^2 \right). \quad (2.2)$$

Equation (2.2) states that the convective flow in the channel produces a parabolic velocity profile in the channel height (y-axis).

To quantify mixing, the mass fraction deviation is often used [47]. Mass fraction deviation can be calculated by the following equation,

$$\delta = \sqrt{\sum_i f_i (\theta_i - \bar{\theta})^2}, \quad (2.3)$$

where  $f_i$  is the fraction of each domain,  $\theta_i$  is the average dimensionless concentration of each domain, and  $\bar{\theta}$  is the final average dimensionless concentration when mixing is 100% complete ( $\bar{\theta}=0.5$ ). For the mixing system presented in this study, there are two domains: one with the concentration of  $c_{\max}$  ( $\theta_1=1$ ) initially and the other with zero concentration ( $\theta_2=0$ ) initially. The ratio of the mass fraction deviation,  $\delta$ , to the initial mass fraction deviation ( $\delta_0$ ) is maximum at the start and equal to 1. As mixing progresses, the value decreases and, when the combined drop becomes fully homogenized (constant concentration over the whole volume), the mass fraction deviation equals 0.

Since almost infinite time is required in order for  $\delta/\delta_0$  to become zero, we must define a specific time when we may consider the mixing is sufficiently complete. Accordingly, we assume that the effective mixing time  $t_{\text{mix}}$  is the time that elapsed until the drop is mixed 90% ( $\delta/\delta_0 \leq 0.1$ ). The mixing is then considered complete when  $\theta_1 < 0.55$  and  $\theta_2 > 0.45$ , respectively. Note that when convection dominates solute transport, a damped oscillation in  $\theta_i$  occurs. In such cases, we can estimate the mixing time by seeking the shortest time,  $t_{\text{mix}}$ , in which  $\delta(t)/\delta_0 \leq 0.1$  for  $t > t_{\text{mix}}$ .

## 2.3 Materials and Methods

### Device Fabrication

The prototypical mixing device was manufactured using the standard soft-lithographic technique [48]. The SU-8 (MicroChem) resist was spun on a bare silicon wafer to make the mold for fluidic channels and pre-baked on the hot plate for 5 min at the 65°C and for 20 min subsequently at the 95°C. After the exposure to 365 nm UV light, the coated wafer was post-baked for 1 min at the 65°C and for 10 min subsequently at the 95°C. The successive 15 min development resulted in the ~80µm thick mold. The depth and width of the channel were analyzed on a surface profiler (Alpha-Step 500, KLA-Tencor). A mixture of PDMS prepolymer and curing agent (5:1 w/w, Sylgard 184, Dow-Corning) was cast against the SU-8 mold and cured at 150°C for 18 min. The cured PDMS cast was carefully removed from the mold and diced into individual dies. For each die, four injection holes were drilled by an aluminum needle. Meanwhile, a glass cover slide (Dow Corning) was spincoated with a 10:1 PDMS mixture and cured to have a thin (~50µm) PDMS layer on the glass side. To bond the device and the glass lid, the PDMS replica and the PDMS-coated glass slide were then oxidized in the UV ozone cleaner (Jelight Company, Inc.) for 25 min and brought into conformal contact at 85°C in a convective oven for 2 hours.

### Fluid Control and Image Acquisition

Each injection port in the device was connected through syringes to a computer-controlled setup, which consisted of four sets of two-way solenoid valves (Numatech). Each solenoid valve could perform a pulsed air pressure (~ 3 psi) injection or a pulsed

vacuum suction. The switches to pressure and vacuum were programmed and operated by LabView (National Instruments). Liquid reagents were also loaded via the syringes with aid of the computerized pressure control. The experiments were performed on the device oriented on a stage of a stereomicroscope (Olympus SZX12). During the mixing progress, in situ imaging was recorded using a digital camera (Nikon Coolpix 4500) with a capture rate of 30 frames/s and then transferred to the computer for further analysis.

### **Image Processing**

A blue dye (Trypan blue 0.4% solution, Sigma-Aldrich) and a colorless liquid (DI water) were used to characterize the mixing performance in this study. The luminance intensity images were recorded and transferred to the computer for evaluation. The RGB images captured were converted into grayscale images expressing only 256 levels of the luminance. In order to rectify light disturbance, a reference background picture was used and the grayscale values of the mixing pictures were subtracted from the background picture. A computer program was written to analyze the luminance levels of the pixels along a line drawn at the center across the mixing channel. In order to remove the high frequency noise, the finite impulse response (FIR) filter was employed during the image processing.

### **Simulation methods**

Two-dimensional simulations were performed using COMSOL Multiphysics software, a commercial finite element package (COMSOL Inc. Burlington, MA). As the channel width ( $\sim 1000\mu\text{m}$ ) is much larger than the depth ( $\sim 80\mu\text{m}$ ), 2-D simulations offer sufficient information to probe the feature of the transport process without requiring

considerable amounts of computation time. Figure 2-1b shows the droplet dimension and arrangement used in these simulations. The calculated internal circulatory flow and the parabolic velocity profile were also illustrated. The upper and lower walls were set to move in the negative x-direction with the velocity  $-U_d$  to simulate the drop velocity  $U_d$  in the positive x-direction. The front and back edges of the slugs were set as nonmoving and no-slip walls. The diffusion coefficient of the solute in water used in the simulations was based on the value estimated from the experiments,  $D=1 \times 10^{-10} \text{ m}^2/\text{s}$ . Other parameters used in the simulations were adopted from the software material library for liquid water.

## 2.4 Results and Discussion

### Analytical Solution

The relative importance of convection to diffusion in mass transport is usually expressed as a dimensionless number, the Péclet number (Pe), where  $Pe=U_d d/D$ . Since the time required for complete mixing (uniform concentration) will depend on the drop size and velocity ( $U_d$ ) as well as the diffusivity of the solute (D), the Péclet number is useful to estimate the mixing time. Although a direct analytical solution to the Eq (2.1) is not available, the equation can be further simplified to estimate the mixing time when the Péclet number is within certain ranges: (i) when Pe is very small, (ii) when Pe is in an intermediate range, and (iii) when Pe is very large. In the following sections, we describe the analytical solutions for these three drop mixing regimes through several simplifications.

#### Diffusion-dominated Mixing.



When the Péclet number is very small ( $Pe \ll 1$ ), convection is very slow compared to diffusion and the solute is transported entirely by diffusion. Since there is no convection and therefore no disturbance in the y direction, the y-axis dependence can be neglected and Eq (1) can be simplified as

$$\frac{\partial c}{\partial t} = D \frac{\partial^2 c}{\partial x^2}. \quad (2.4)$$

Initial conditions for Eq (2.4) are,

$$c = c_{\max} \quad 0 \leq x \leq L/2 \quad (2.5)$$

$$c = 0 \quad L/2 < x \leq L. \quad (2.6)$$

As the front and back walls are the ends of drop, we have no flux boundary conditions as,

$$\frac{\partial c}{\partial x} = 0 \quad \text{at } x=0 \text{ and } x=L. \quad (2.7)$$

Eq (2.4)-(2.7) give a cosine series solution as follows.

$$\theta = \frac{c}{c_{\max}} = 0.5 + \sum_{\substack{n=1 \\ \text{odd}}}^{\infty} (-1)^{(n-1)/2} \frac{2}{n\pi} \exp\left(-\frac{t}{\tau_L} n^2 \pi^2\right) \cos\left(n\pi \frac{x}{L}\right) \quad (2.8)$$

where  $\tau_L = L^2/D$  and  $\theta$  is the dimensionless concentration of the solute, which is a function of the axial position (x) and time (t).

The average dimensionless concentration of the two domains corresponding to Eq (2.5) and (2.6) respectively can be calculated by the following equations:

$$\theta_1 = \frac{1}{L/2} \int_0^{L/2} \theta(x) dx = \sum_{\substack{n=1 \\ \text{odd}}}^{\infty} \frac{4}{(n\pi)^2} \exp\left(-\frac{t}{\tau_L} n^2 \pi^2\right) \quad (2.9)$$

$$\theta_2 = \frac{1}{L/2} \int_{L/2}^L \theta(x) dx = 0.5 - \sum_{\substack{n=1 \\ \text{odd}}}^{\infty} \frac{4}{(n\pi)^2} \exp\left(-\frac{t}{\tau_L} n^2 \pi^2\right). \quad (2.10)$$

Based on the above expressions, the mass fraction deviation is given by

$$\frac{\delta}{\delta_0} = \frac{1}{0.5} \sqrt{\sum_i f_i (\theta_i - \bar{\theta})^2} = \sum_{\substack{n=1 \\ \text{odd}}}^{\infty} \frac{8}{(n\pi)^2} \exp\left(-\frac{t}{\tau_L} n^2 \pi^2\right). \quad (2.11)$$

where  $\bar{\theta} = 0.5$  and  $\delta_0 = 0.5$ . The smallest value of  $t$  ( $t_{\text{mix}}$ ) to meet the condition that  $\delta/\delta_0 \leq 0.1$  in Eq (11) is given by  $0.21\tau_L$ . The mixing time can be further non-dimensionalized with the reference diffusion time  $\tau_D = d^2/D$  and thus,

$$\tau_{\text{mix}} = \frac{t_{\text{mix}}}{\tau_D} = 0.21 \frac{\tau_L}{\tau_D} = 0.21 \frac{L^2/D}{d^2/D} = 0.21 \varepsilon^2 \quad (2.12)$$

where  $\varepsilon = L/d$  is the aspect ratio.

In Figure 2-2a, the diffusion-dominated mixing time is plotted at various drop aspect ratios. Note that the mixing time is neither dependent on the drop velocity nor  $Pe$  but is proportional to the square of the drop aspect ratio,  $\varepsilon$ . Since the mass transport is caused entirely by diffusion, the mixing time becomes independent of  $Pe$ , but as the drop size gets longer, the mixing time increases because the length for diffusion along the drop increases.

Dispersion-dominated Mixing.

For  $1 \ll Pe \ll \pi^2 \varepsilon$ , the mixing can be described by Taylor dispersion [49]. For slit-type channels, the Taylor dispersion coefficient,  $D_{TD}$ , is given by the following relationship [49]:

$$D_{TD} = \frac{U_d^2 d^2}{210D} = \frac{1}{210} Pe^2 D. \quad (2.13)$$

The effective diffusion coefficient [50] is then written as

$$D_{eff} = D + D_{TD} = D + \frac{U_d^2 d^2}{210D} = \left(1 + \frac{1}{210} Pe^2\right) D. \quad (2.14)$$

The diffusion coefficient in the right-hand side of Eq (2.3) can be replaced with  $D_{eff}$  or even  $D_{TD}$  without significant loss of accuracy because  $Pe$  is much greater than the unity.

The replacement of  $D$  results in a mixing time of

$$\tau_{mix} = \frac{t_{mix}}{\tau_D} = 0.21 \frac{\tau_{TD}}{\tau_D} = 0.21 \frac{L^2 / D_{TD}}{d^2 / D} = 44.1 \frac{\varepsilon^2}{Pe^2}. \quad (2.15)$$

When the transport is dominated by Taylor dispersion, the mixing time is proportional to the inverse square of  $Pe$ , indicating that the mixing is enhanced as the drop velocity increases or the drop aspect ratio decreases.

To better explain the correlation between mixing and the aspect ratio, a modified Péclet number [4], or a similar dimensionless number [39], has been suggested in the literature. The main idea behind this modification is that when convective mixing occurs, convection and diffusion usually develop in different directions. Thus, for a system with a high aspect ratio, the Péclet number provides insufficient information about the importance of convection and diffusion. The modified Péclet number is defined by,

$$Pe^* = \frac{\text{diffusive time scale}}{\text{convective time scale}} = \frac{d^2/D}{L/U_d} = \frac{Pe}{\varepsilon}. \quad (2.16)$$

In our previous study [39], a similar dimensionless number was defined as the ratio of the drop velocity ( $U_d$ ) versus the critical interlayering velocity,  $\pi^2 \left(\frac{L}{d}\right) \frac{D}{d}$ . The proposed dimensionless number corresponded to  $\frac{1}{\pi^2} Pe^*$  and sufficiently accounted for the combined effect of the aspect ratio and the Péclet number. Note that the term  $\pi^2$  appears because of the nature of the concentration profile in a slit-type channel. If the diffusive time scale in Eq (2.16) is replaced by  $\frac{d^2}{\pi^2 D}$ , which has been derived from the method that Taylor described for a cylindrical system [49], a different modified Péclet number can be obtained as,

$$Pe^{**} = \frac{\text{diffusive time scale}}{\text{convective time scale}} = \frac{1}{\pi^2} \frac{d^2/D}{L/U_d} = \frac{Pe^*}{\pi^2} = \frac{Pe}{\pi^2 \varepsilon}. \quad (2.17)$$

For simplicity, we use the modified Péclet number defined in (2.16) in this study. Using this modified Péclet number, Eq (2.15) can be now rewritten by

$$\tau_{mix} = \frac{t_{mix}}{\tau_D} = 44.1(Pe^*)^{-2} \quad (2.18)$$

and the dependency of the dispersion-dominated mixing time on  $Pe^*$  can be seen in Figure 2-2a. The mixing time is independent of the aspect ratio as a function of  $Pe^*$ . This is because the modified Péclet number already includes the effect of the aspect ratio.

### Convection-dominated Mixing.

When the drop velocity is sufficiently fast ( $Pe^* \gg \pi^2$ ), multiple layers develop due to the internal circulatory flow that are not destroyed by vertical diffusion. In this case, Eq (3) can be solved only numerically. To extend the availability of an analytical solution for this mixing regime, we developed an approximate expression.

After a certain mixing time  $t_C$ , the drop travels  $N = U_d t_C / L$  drop lengths and makes  $n = N/3 = U_d t_C / 3L$  internal circulations for a sufficiently high aspect ratio. The internal circulations cause the solute layers to fold over themselves every half circulation, and thus the number of foldings ( $N_F$ ) correspond to  $N_F = 2n$  or  $N_F = 2N/3$ . Due to the nature of merging and splitting in the internal circulatory flows, each folding event produces a different number of layers: when the circulatory flow splits from the center line to the upper and lower boundaries (near the front end), it produces  $3N_F$  layers, whereas when the flow merges from the boundaries to the center line (near the back end), it only produces  $1.5N_F$  horizontal layers. Since the two kinds of folding occur in an alternating manner, we assume that the circulation would create  $2.25N_F$  or  $9N_F/4$  layers. Thus, the number of layers ( $N_L$ ) can be calculated as a function of the number of drop lengths that the drop travels using the equation

$$N_L = \frac{9}{4} N_F = \frac{3}{2} N. \quad (2.19)$$

Mixing occurs when the solutes diffuse between two adjacent layers. When there are  $N_L$  layers within the depth  $d$ , the interlayer distance,  $s$ , is approximated as  $s=d/2N_L=d/3N$ . If the interlayering continues until the solute diffuses to complete mixing (90%), the radial diffusion reference timescale  $0.21s^2/D$  must be balanced with  $t_c$  (i.e.,  $t_c=0.21s^2/D$ ). The mixing time is then calculated as follows:

$$\tau_{mix} = \frac{t_{mix}}{\tau_D} = \frac{t_c}{\tau_D} = (0.21)^{1/3} \left(\frac{1}{3}\right)^{2/3} \left(\frac{L/U_d}{d^2/D}\right)^{2/3} = 0.286(Pe^*)^{-2/3}. \quad (2.20)$$

Figure 2-2a illustrates the plot of the convective mixing time versus  $Pe^*$ . Note that this convection-enhanced mixing is most effective near the upper and bottom walls of the channel, where the solutes are stretched into thinner lamellae due to the higher velocity. At the center, the solutes are more persistent and stretched on longer timescales. The inference leading to Eq (2.20) circumvents this singularity and is based on the assumption that all of layers are equidistant. At longer mixing timescales, it is suggested that the mixing time corresponds to a  $Pe^{-1/2} \ln Pe$  scaling [51]. In addition, we should note that Eq (2.20) tends to slightly underestimate the mixing time because the  $y$ -directional flow is neglected in its derivation. This  $y$ -direction flow near the front and back ends of the drop would make the rate of layer formation slower, especially when the drop aspect ratio ( $\epsilon$ ) is small.

In our previous study [39], we theoretically showed that for convection-dominated mixing, the mixing time can be estimated by assuming that the drop would be first displaced three drop lengths and then stop. After stopping, the drop would then mix only by vertical diffusion between layers. Although this approach provides very practical estimations applicable to typical microfluidic experiments, its validity is limited because of the assumption that no diffusion would occur during drop transportation. As a result, this approach tends to overestimate the mixing time, excluding the effect of the accompanying diffusion (Figure 2-2b). Nonetheless, it is often very informative to estimate the mixing time when the possible drop displacement is predetermined. For instance, if the distance the drop will travel in a microfluidic device is fixed, mixing must be accomplished in this length. Figure 2-2b shows the mixing time estimated by this simplified approach at various drop displacement distances. It is clear that at higher  $Pe^*$ , the mixing time decreases as the drop displacement increases.

Combined Solution.

Combining Eq (2.12), (2.18) and (2.20), an asymptotic approximating line can be obtained for sufficiently long drops ( $\epsilon > 10$ ).

$$\tau_{mix} = \frac{1}{\frac{1}{0.21\epsilon^2} + \frac{1}{44.1Pe^{*-2} + 0.286Pe^{*-2/3}}} \quad (2.21)$$

For smaller drops ( $\epsilon < 10$ ), it is more accurate to separate Eq (2.21) into two asymptotic lines for two different regimes as in

$$\tau_{mix} = 0.21 \varepsilon^2 \frac{1}{1 + \frac{\varepsilon^2}{210} Pe^{*2}} \quad \text{when } Pe^* < \pi^2 \text{ and} \quad (2.21a)$$

$$\tau_{mix} = 44.1 Pe^{*-2} + 0.286 Pe^{*-2/3} \quad \text{when } Pe^* > \pi^2 \quad (2.21b)$$

The combined dimensionless mixing time,  $\tau_{mix}$ , is a function of the aspect ratio and the modified Péclet number, as shown in Figure 2-2a. Considering that there are basically three different mixing regimes, it is noteworthy that the dispersion-dominated mixing regime tends to shrink as the aspect ratio decreases. This is because as the drop size decreases at a constant drop velocity, the diffusion and convection timescales become comparable to each other, and thus the intermediate region becomes smaller.

Another problem of great relevance to experimentalists is to find the optimal geometry to give the lowest possible mixing time for a given solute. When designing and fabricating a micromixer, the drop displacement required for complete mixing (the length of mixing channel) must be determined. A dimensionless displacement for mixing,  $\lambda_{mix}$ , can be defined as the ratio of the displacement versus the drop length,

$$\lambda_{mix} = \frac{U_d t_{mix}}{L} = \tau_{mix} \left( \frac{d^2/D}{L/U_d} \right) = \tau_{mix} (Pe^*) \quad (2.22)$$

Consequently,

$$\lambda_{mix} = 0.21 \varepsilon^2 (Pe^*) \quad \text{for diffusion-dominated mixing when } Pe^* \ll \pi^2/\varepsilon$$

$$\lambda_{mix} = 44.1 (Pe^*)^{-1} \quad \text{for dispersion-dominated mixing when } \pi^2/\varepsilon \ll Pe^* < \pi^2, \text{ and}$$

$$\lambda_{mix} = 0.286 (Pe^*)^{1/3} \quad \text{for convection-dominated mixing when } Pe^* \gg \pi^2.$$



Combining the expressions yields an asymptotic equation that is valid for the entire area :

$$\lambda_{mix} = \frac{Pe^*}{\frac{1}{0.21\varepsilon^2} + \frac{1}{44.1Pe^{*-2} + 0.286Pe^{*-2/3}}} \quad (2.23)$$

Figure 2-2c plots the estimated displacement required for mixing as a function of the modified Péclet number, at various aspect ratios. When  $Pe^*$  is very small, the displacement is proportional to  $Pe^*$  or the drop velocity, because the drop is constantly moving even though the movement does not accelerate diffusive mixing. In contrast, the required displacement in the Taylor dispersion-dominated mixing regime ( $\pi^2/\varepsilon \ll Pe^* \ll \pi^2$ ) decreases with  $Pe^*$ , since the convective flow greatly improves mixing efficiency. Finally, when the flow is too fast ( $Pe^* \gg \pi^2$ ), the required displacement increases algebraically with  $Pe^*$ , although the mixing time decreases. This is because the internal circulatory flows constantly reproduce layers, stretching fluid elements, and thus the drop has to travel a longer distance until the diffusive mixing is complete. Note that for typical microfluidic conditions ( $10 < Pe^* < 1000$ ), the required drop displacement distant never exceeds three drop lengths, as we noted in our previous study [39].

The drop size is another important factor to determine when designing microfluidic devices. Since the channel depth is unchangeable after fabrication, one can control the input volume of drop in order to adjust the drop length. Figure 2-2d plots the mixing time as a function of the drop aspect ratio at various  $Pe^*$ . In general, as the aspect ratio increases, the mixing time also increases. However, when the aspect ratio is very high (e.g., a continuous flow system) at a certain modified Péclet number ( $\varepsilon \gg \pi^2/Pe^*$ ),

the mixing process follows the Taylor-dispersion scheme and the mixing time becomes independent on the aspect ratio. Furthermore, when  $Pe^* \gg \pi^2$ , the aspect ratio does not affect the mixing time as denoted above.

### **Drop Mixing Simulations**

Computer simulations were performed to confirm the theoretical modeling results. To simulate the complex mixing process in microchannels, an incompressible Stokes and a convection-diffusion mass transport were numerically solved simultaneously. The upper and lower walls move in the negative x-direction with the velocity  $-U_d$ . This motion simulates a stationary drop moving through a straight channel at the velocity of  $U_d$ . Combined with the no-slip boundary conditions at the front and back ends of the drop, the internal circulatory flows inside the drop were simulated as illustrated in Figure 2-1c.

Figure 2-3 depicts the velocity profiles in the x- and y-directions for a drop of  $\epsilon=7$ . The fluid velocity in the x-direction  $U_x(y)$  can be estimated from Hagen–Poiseuille law in the area far from the front and back ends, whereas the fluid velocity in the y-direction  $U_y(x)$  is zero along the drop except for the vicinity of the front and back ends. When the drop flows through the curved region, the velocity profiles change depending on the curvature and the channel width. For a 1mm wide channel and a radius of curvature of 4.2mm, an approximately 17% increase from the straight-channel  $U_d$  at the outer wall and a 17% decrease at the inner wall result from the curved flow. Since the flow is laminar, no change of the drop orientation is expected.

In Figure 2-4, the mixing progress in a straight channel for  $Pe^*=0.4$  (a),  $Pe^*=6$  (b), and  $Pe^*=132$  (c) were simulated, respectively. Note that the mixing for  $Pe^*=0.4$  and

$Pe^*=6$  is dominated by diffusion and Taylor-dispersion, respectively. No apparent sign of convective transport by internal circulation is observed. In contrast, interlayering is observed in Figure 2-4c indicating that convection has a significant role in mixing for  $Pe^*=132$ . Figure 2-5 illustrates the simulated interlayering progress for  $Pe^*=2000$ . The layers remain for an extended time because the convective transport is much faster than the diffusive transport.

Figure 2-6 shows how the concentration of the merged drop changes during the mixing process. The blue line represents the concentration of the domain that initially contained the solute ( $c=c_{max}$ ), and the green line shows the concentration of the domain initially without the solute ( $c=0$ ). Note that the concentration change for the dispersion-dominated mixing (Figure 2-5b) conforms to the behavior of diffusive transport (Figure 2-5a) but with a shorter timescale. This behavior was predicted from the theoretical modeling in the previous section, because the diffusion coefficient,  $D$ , could be replaced with the dispersion coefficient,  $D_{TD}$ . However, for the convection-dominated mixing, the concentrations of both domains are oscillating, and gradually converging due to the internal circulation. The frequency of oscillation increases as  $Pe^*$  increases because at the higher drop velocity the drop can travel a longer distance before complete homogenization.

### **Experimental Verification**

One of the common mixing quantification techniques is using a tracer dye to determine the extent of mixing. From a simple calibration process, the concentration of trypan blue dye was considered proportional to the intensity of the recorded image (Figure 2-7). When the solute in the drop produces layers, the apparent image intensity

does not correctly reflect the layered concentration differences, but is considered reflecting an average concentration through the layered structure. The recorded images were analyzed in a grayscale mode, the background image was subtracted from the image to eliminate intensity fluctuations, and high frequency noise was removed by finite impulse response (FIR) filtering.

Aligning two drops sequentially is not straightforward. Thus, we developed a membrane bypass valve (MBV) to aid in drop positioning (Figure 2-8). The PDMS MBV is made of a thin ( $\sim 30\mu\text{m}$ ) PDMS membrane connected to atmosphere or a vacuum source. The MBV allows air to pass but not liquid. Figure 2-9 illustrates the use of MBV to coalesce two drops. The trapped air between two drops can be either drawn off by a vacuum source connected to the MBV (Figure 2-9a, 9b) or by applying air pressure from the both ends to push two drops towards the center and the trapped air out to atmosphere (Figure 2-9c). During the soft-lithographic fabrication of the MBV, the higher fraction of curing agent than the manufacturer-recommended amount was used in order to make the device less elastic and thus to reduce unwanted deformation of the embedded PDMS membrane.

For a given micromixer with fixed geometric dimensions, one can alter the mixing condition ( $Pe^*$ ) by controlling the drop velocity. Figure 2-10 shows the mixing progress at a high  $Pe^*$  ( $\sim 132$ ), starting from the initial state when the two drops fuse and an interface develops, to the state of complete mixing when the drop has traveled along the channel. Note that the merged drop rapidly mixes within a few seconds. This phenomenon was investigated via theoretical modeling and simulations in the previous sections. Figure 2-9b shows the average concentrations of the left and right domains. The

oscillating concentrations gradually converges with time until complete homogenization, as was shown in the simulations.

In the intermediate range of  $Pe^*$  ( $\sim 6$ ) (Figure 2-11), however, the mixing occurs slower and a different mixing mechanism is observed. The convective interlayering is combined with diffusive spreading. Because of this axial spreading, the mixing is greatly enhanced compared to pure diffusion mixing. When  $Pe^*$  is small ( $\sim 0.4$ ) the merged drop has been displaced 63 mm for  $\sim 10000$  seconds back and forth along the channel but the mixing is quite incomplete (Figure 2-12). The extended time required for complete mixing causes the drop to be exposed to air for hours resulting in a significant loss of drop volume due to evaporation. In addition, reduction in drop volume makes the concentration higher, possibly leading to inaccurate analysis of concentration data. The volume loss may be reduced by saturating the device environment with excessive water. Since the device is made of gas-permeable PDMS, the excessive water must cover the device top as well as the sample inlets. The resulting sacrificial evaporation of the supplied water fairly reduces the sample evaporation rate, but approximately 10-20% volume loss was still observed during the experiment. The concentration curve for the 90% mixing (dotted line) was predicted based on the results for 0-10000 seconds for the comparison purpose.

The effect of channel curvature on mixing was also investigated. The mixing experiments were performed in the microchannel that contains a curved region ( $w=1\text{mm}$  and the radius of curvature= $8.5\text{mm}$ ). As can be seen in Figure 2-3, the curvature affects the drop velocity and thus the convective transport, not diffusive transport. Since the effect of convection is negligible when the mixing is diffusion-dominated, we did not consider the effects for low  $Pe^*$ .

In Figure 2-13, the mixing progresses in the straight (a) and curved (b) channel for  $Pe^*=100$  are simulated, respectively. Interestingly, there is little noticeable difference in mixing time between the straight and curved mixing channels even at the high  $Pe^*$  of 100. A possible reason is that the influences of the accelerated drop velocity at the outer wall and the decelerated velocity at the inner wall would offset each other. In other words, the mixing is enhanced at the outer region because of the faster velocity, but the lower velocity at the inner region causes a reduced mixing

In Figure 2-14, we show that our experimental results are in good agreement with the theoretical modeling as well as simulation results. It is important to note the slight discrepancy between the theoretical modeling and the experiment results. The underestimated mixing time (shorter mixing time than the theory predicts) is most likely due to the drop fusion mechanism we employed in the experiments. When two separate drops merge by vacuum suction or air pressure push, the fused drop are prone to make a broader interface, indicating a slight degree of mixing has been already begun in the interfacial area leading to the underestimation of mixing time. On the other hand, the overestimated mixing time (longer mixing time than the theory predicts) may be attributed to the pulsed air control. To generate a pressure-driven flow, air pressure was applied in a pulsed manner, and it is likely that the measured mixing time would include non-mixing time between pulses.

## **2.5 Conclusions**

We have demonstrated a two-dimensional model in a slit-type microchannel for a discrete drop mixing microfluidic systems. Discrete drop mixing occurs in three different

regimes (diffusion-dominated, dispersion-dominated, and convection-dominated) depending on the Péclet number ( $Pe$ ) and the drop dimensions. In the theoretical section, the mixing time can be predicted for given operating parameters using an asymptotic mixing time curve. A mixing distance curve was also introduced to determine the drop transportation distance required for mixing. Computer simulations and experimental results confirmed the mixing mechanisms we assumed theoretically.

### **Acknowledgement**

This chapter has been separately published in **Rhee, M.** and Burns, M. A. (2008). *Langmuir*. **24**(2):590-601.

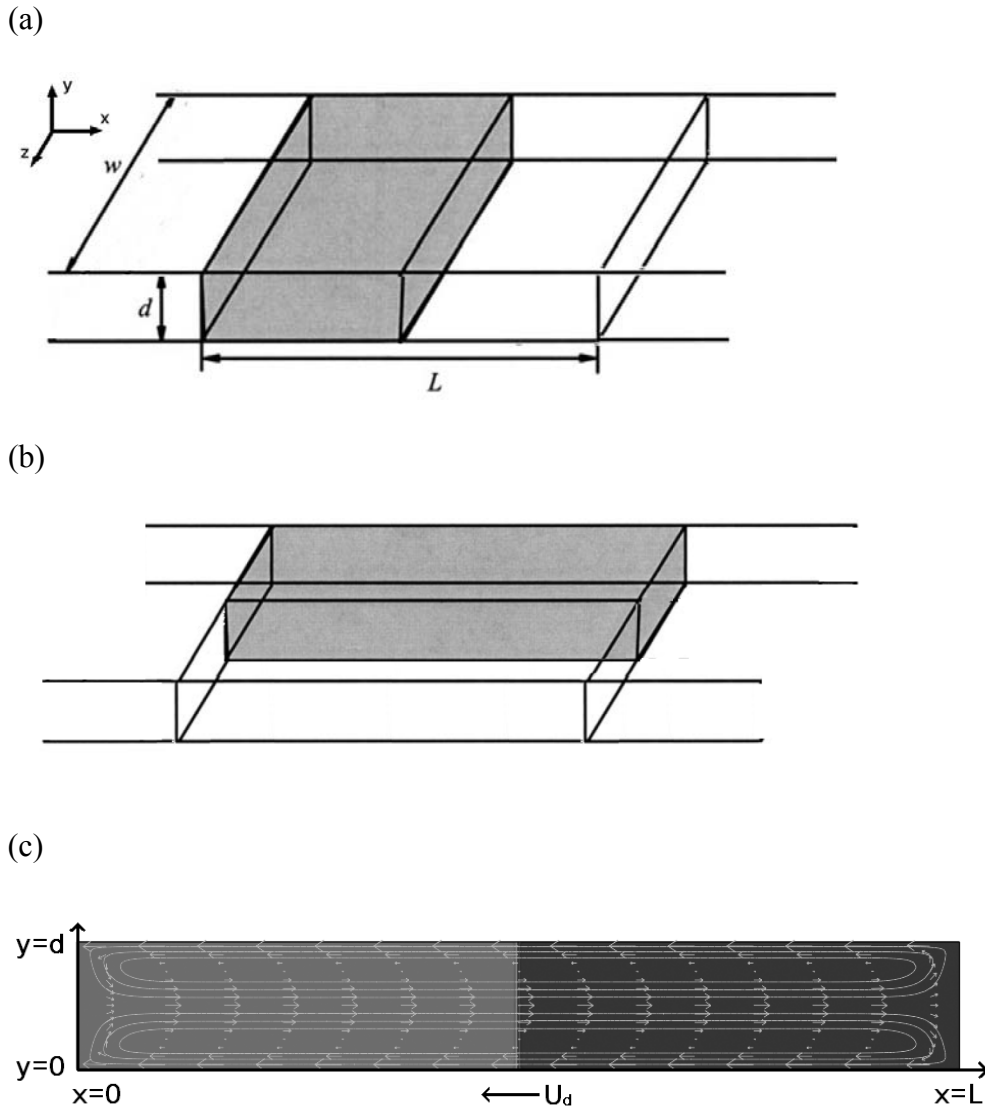
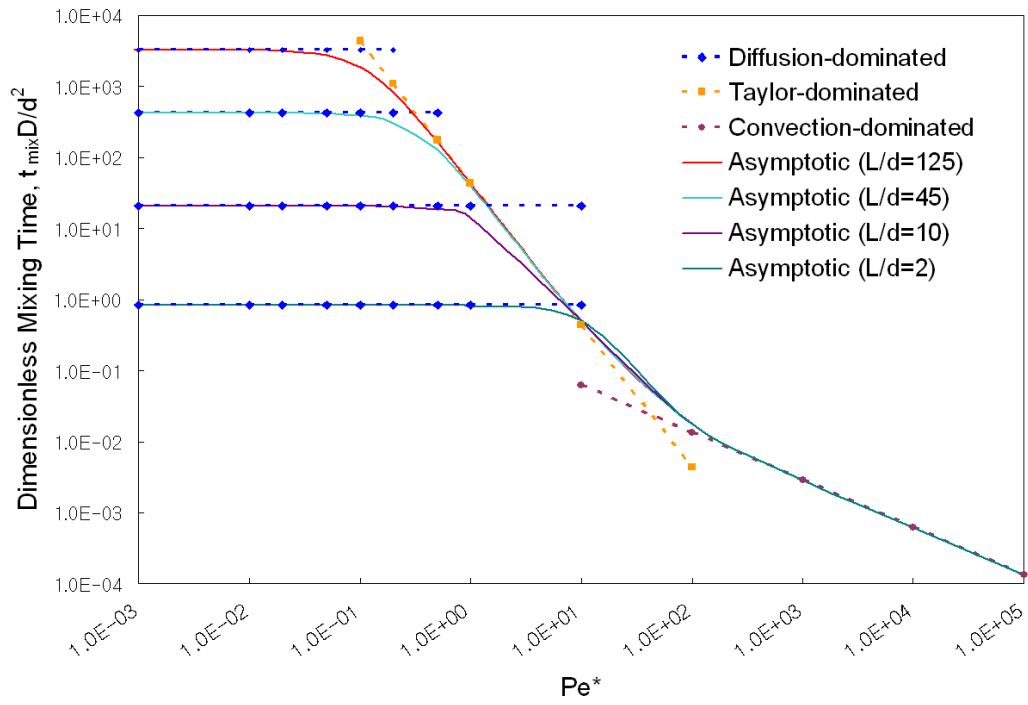


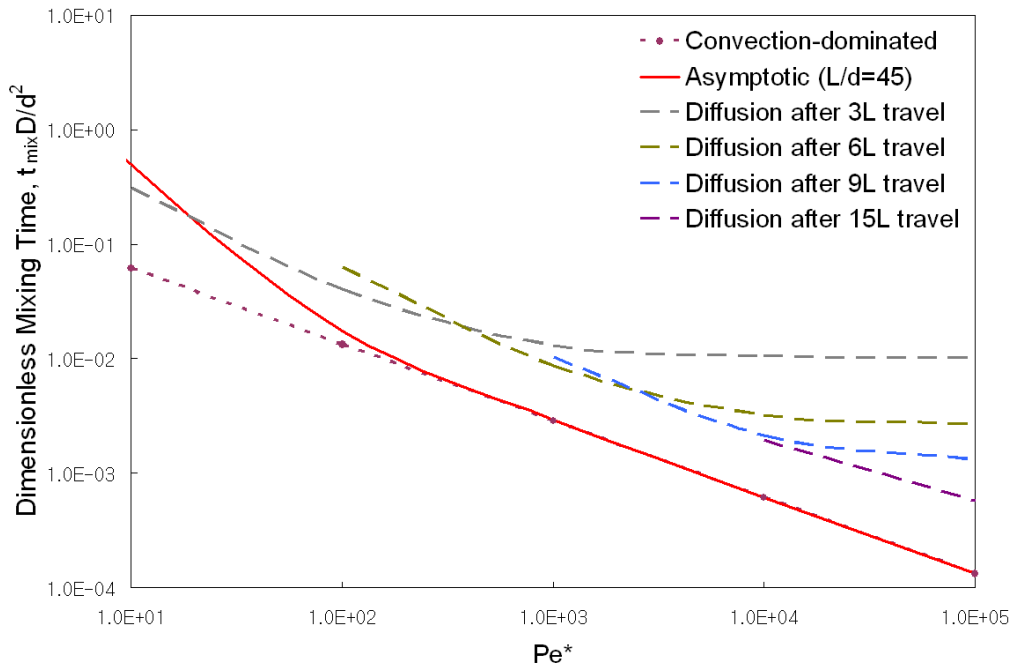
Figure 2-1. Mixing Model. (a) An axially-arranged discrete drop placed in a slit-type microchannel, where the width of the channel is much larger than the depth of the channel. (b) A radially-arranged drop. (c) Internal circulation streamlines present in a two component drop moving at a constant velocity,  $U_d$ , in a two-dimensional plane. The frame of reference is moving at  $U_d$  in the negative  $x$ -direction. The arrows represent the velocity vectors in the  $x$ - $y$  plane.



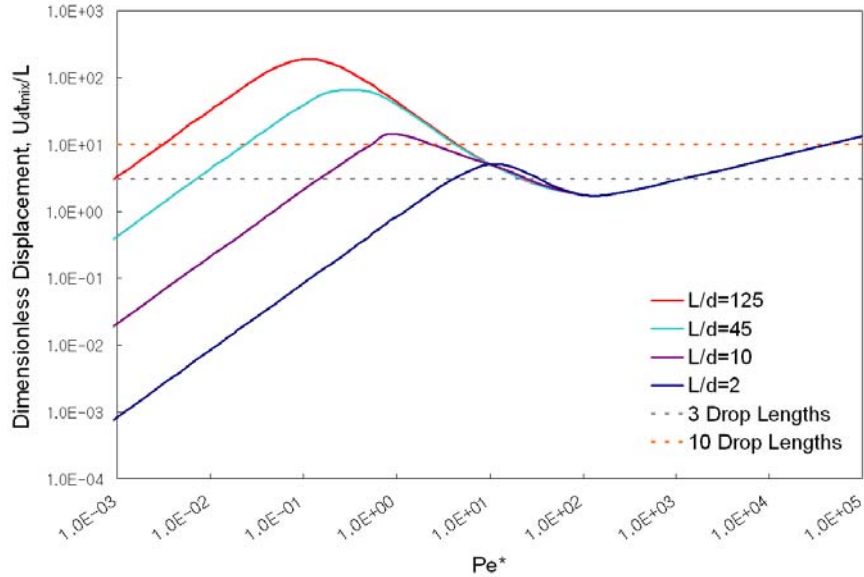
(a)



(b)



(c)



(d)

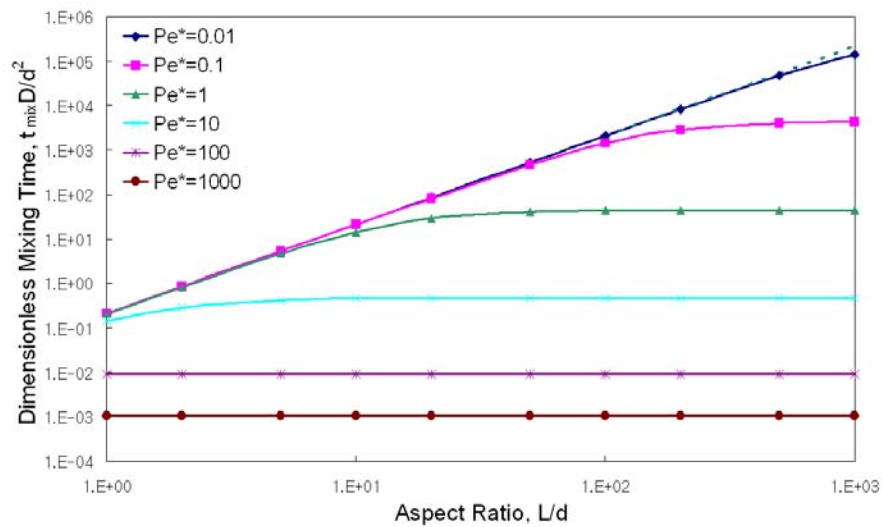
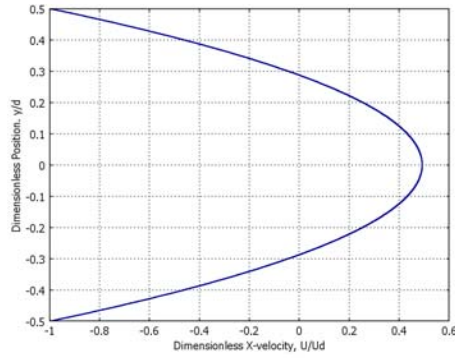
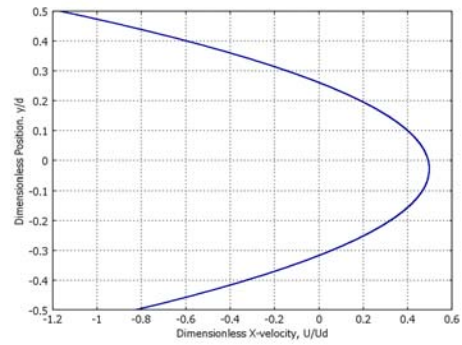


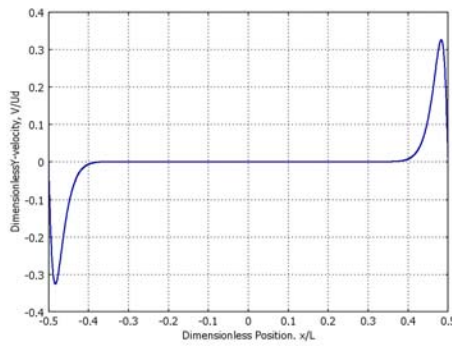
Figure 2-2. Analytical Quantification of Mixing. (a) Three different mixing regimes and asymptotic curves for mixing time at various drop aspect ratios. (b) Mixing time estimation after the drop displacement of predetermined distances. (c) Asymptotic curves for drop displacement required for mixing at various aspect ratios. (d) Mixing time as a function of the drop aspect ratio at various modified Péclet numbers.



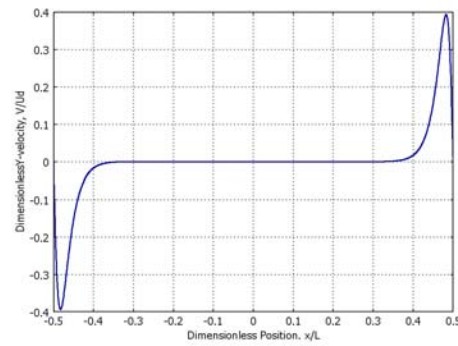
(a) straight channel: x-velocity (at  $x=0$ )



(b) curved channel: x-velocity (at  $x=0$ )



(c) straight: y-velocity (at  $y/d=0.29$ )



(d) curved: y-velocity (at  $y/d=0.29$ )

Figure 2-3. Velocity profiles for a drop of  $\varepsilon=7$ . (a) x-velocity (at  $x=0$ ) in the straight channel. (b) x-velocity (at  $x=0$ ) in the curved channel ( $w=1\text{mm}$  and the radius of curvature= $4.2\text{mm}$ ). (c) y-velocity (at  $y/d=0.29$ ) in the straight channel. (d) y-velocity (at  $y/d=0.29$ ) in the curved channel.

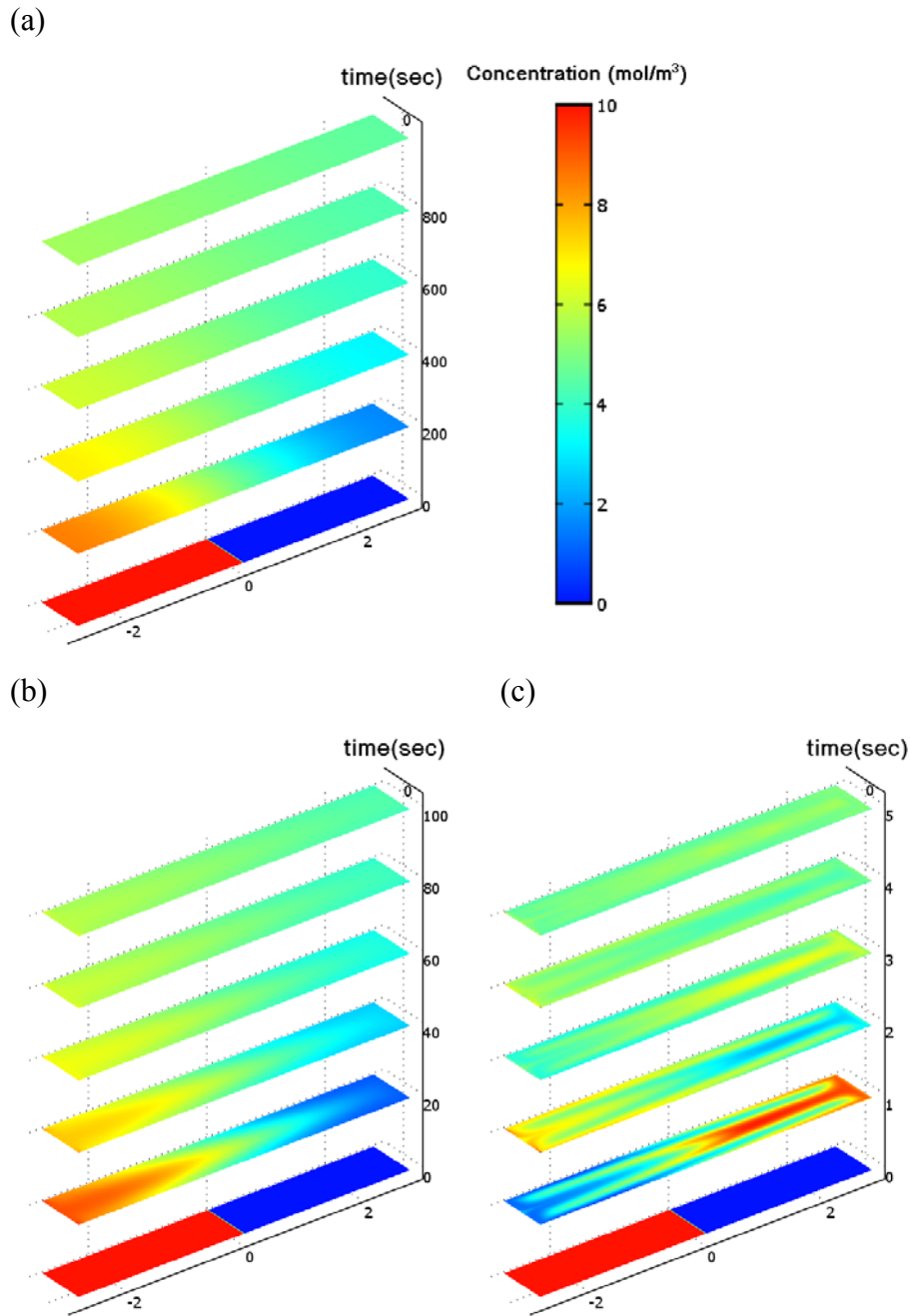


Figure 2-4. COMSOL Simulation. Concentration variation in a straight channel ( $\varepsilon=7$ ) for (a)  $Pe^*=0.4$ , (b)  $Pe^*=6$ , and (c)  $Pe^*=132$

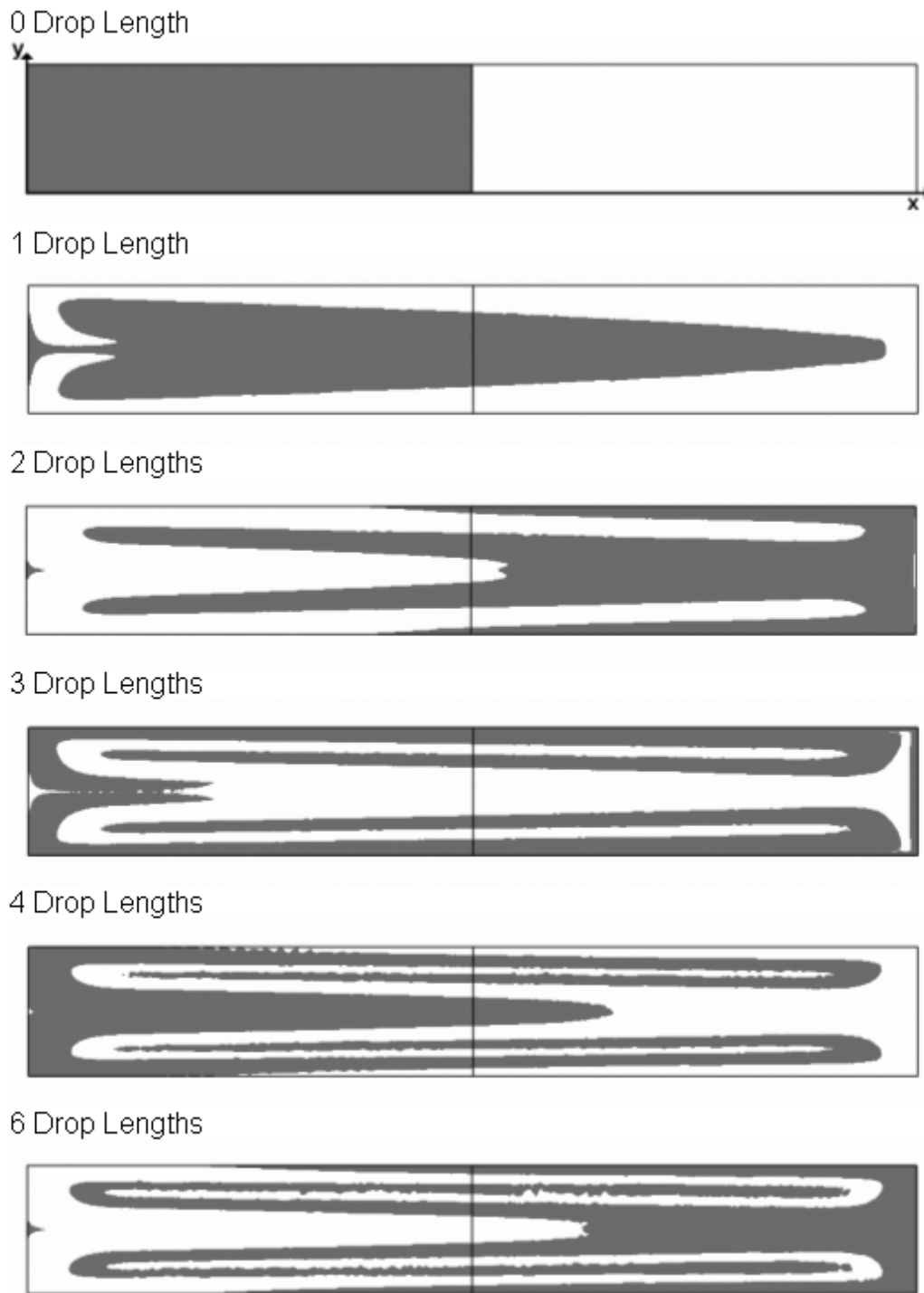
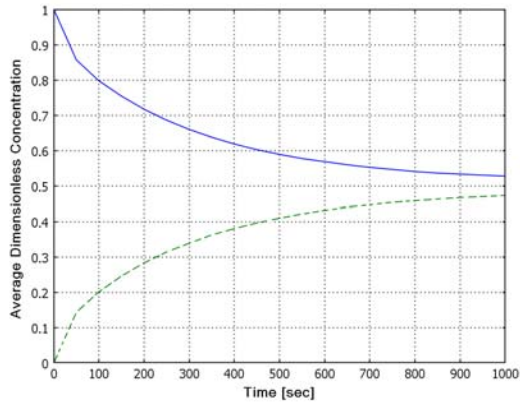
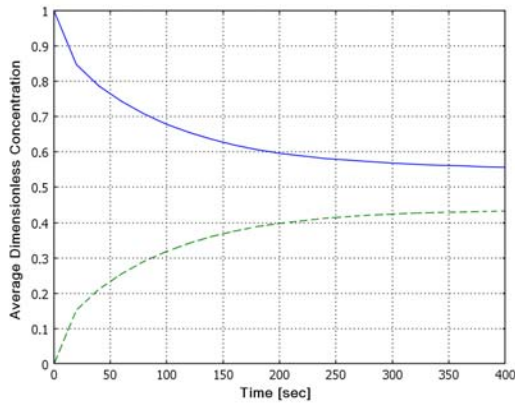


Figure 2-5. Simulated interlayering progress for  $Pe^*=2000$  and  $\epsilon=7$ .

(a)



(b)



(c)

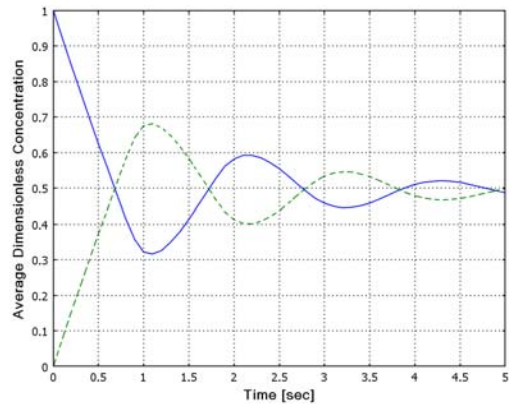


Figure 2-6. Mixing Progress. Concentration changes in two domains for (a) diffusion-dominated mixing for  $Pe^*=0.4$ , (b) dispersion-dominated mixing ( $Pe^*=6$ ), and (c) convection-dominated mixing ( $Pe^*=132$ ).

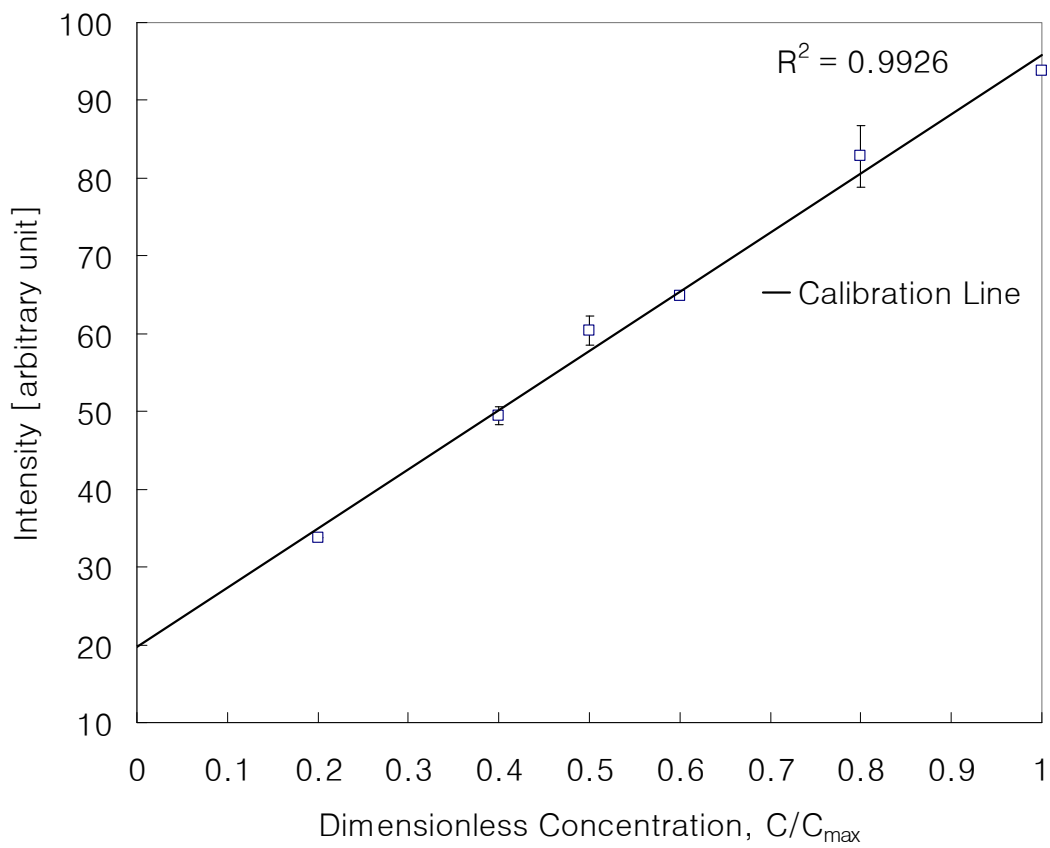


Figure 2-7. Calibration curve for the trypan blue 0.4% solution

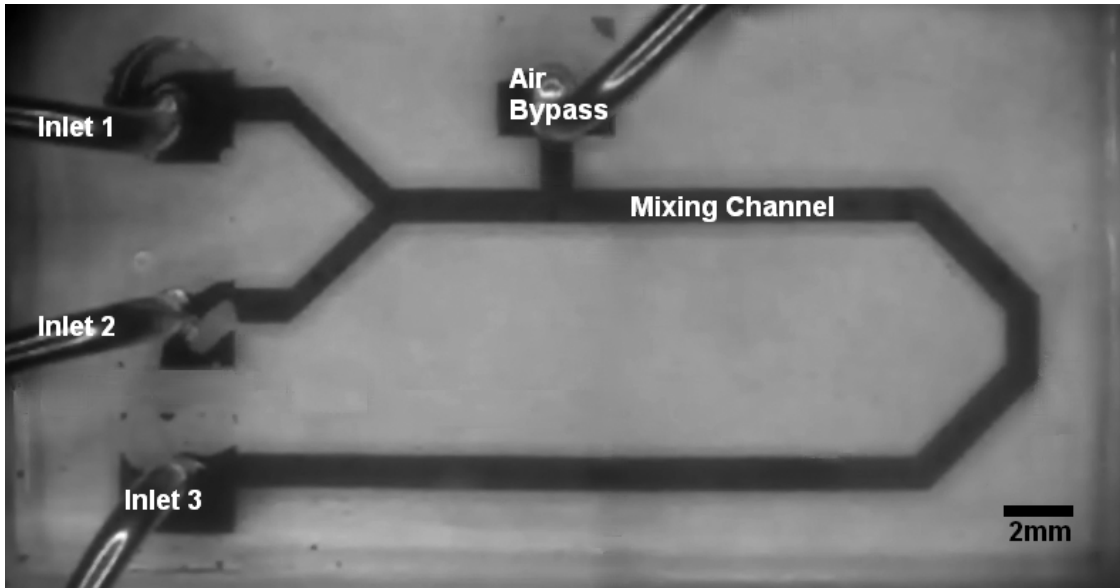


Figure 2-8. Photo of the mixing channel and the MBV filled with the blue solution.



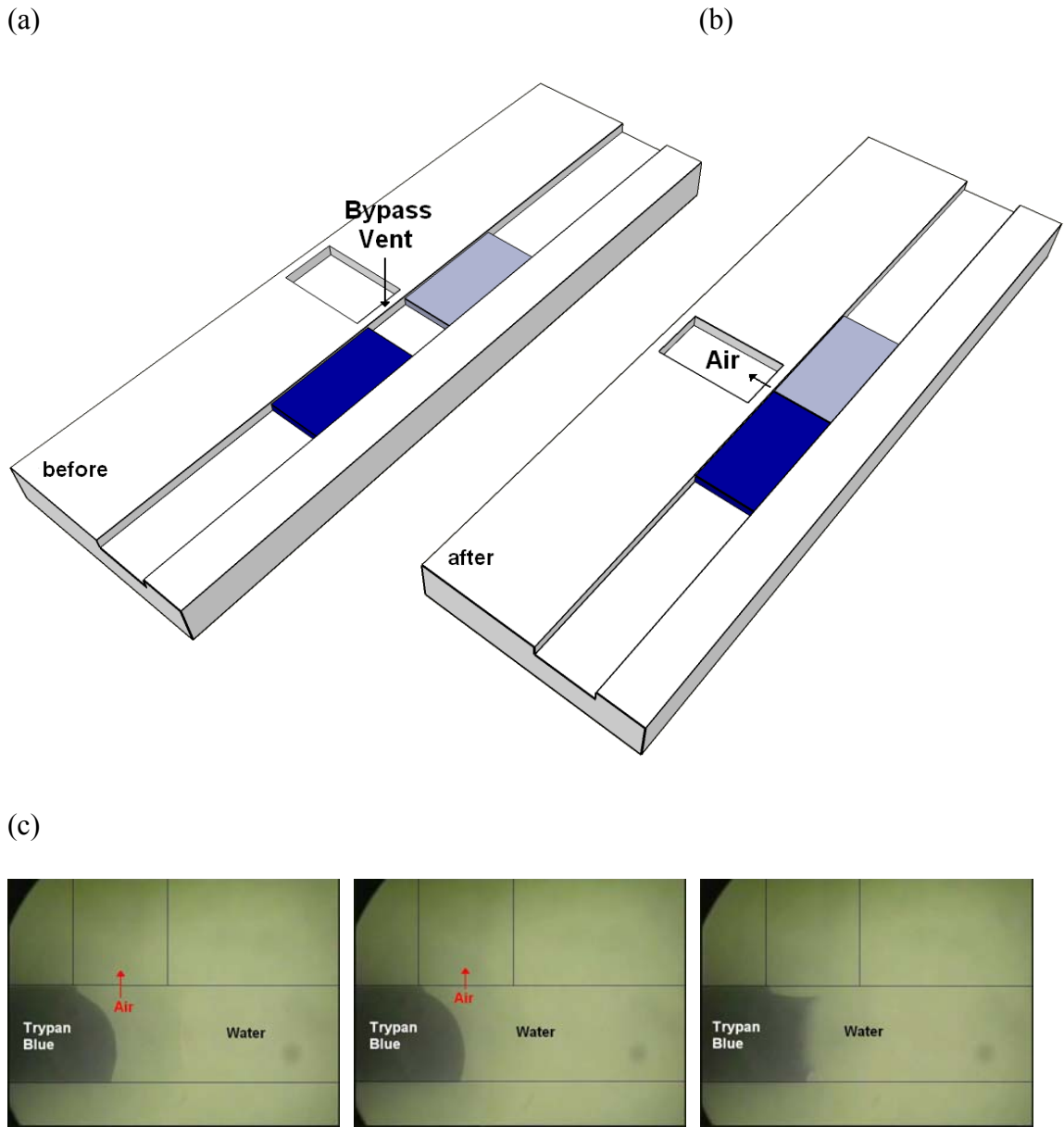
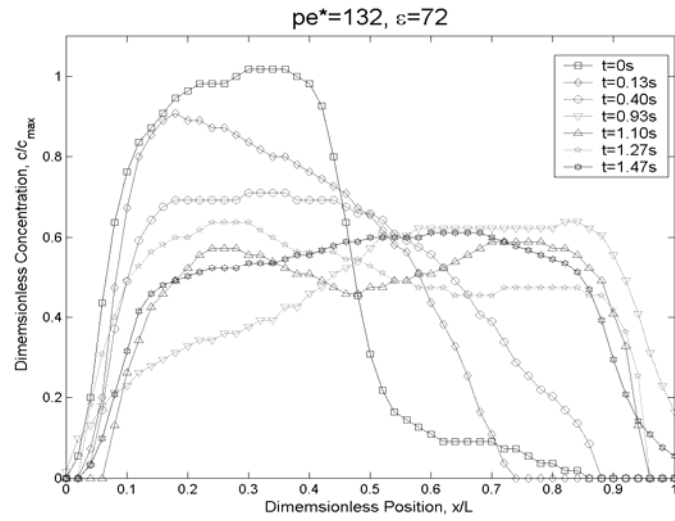
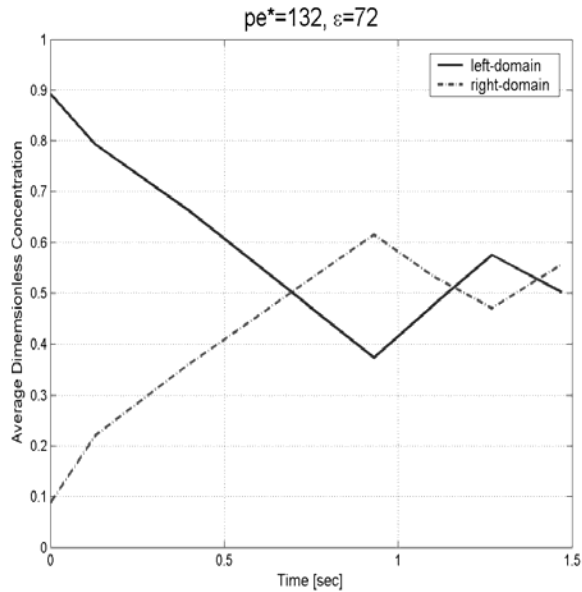


Figure 2-9. The use of MAB to coalesce two drops (a). The trapped air between two drops can be either (b) drawn off by a vacuum source connected to the MBV or (c) by applying air pressure from the both ends to push two drops towards the center and the trapped air out to atmosphere via the MBV.

(a)



(b)



(c)

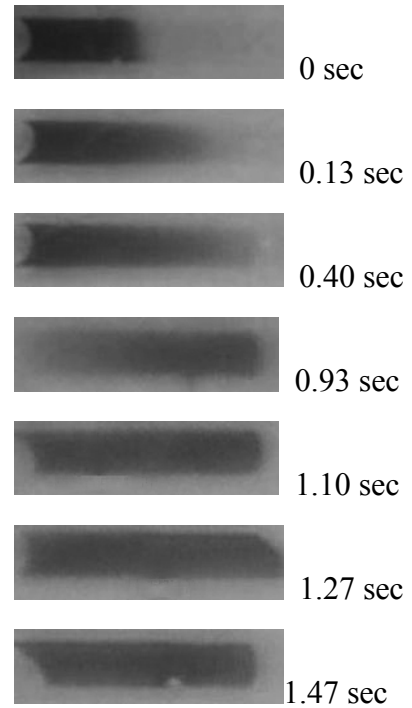
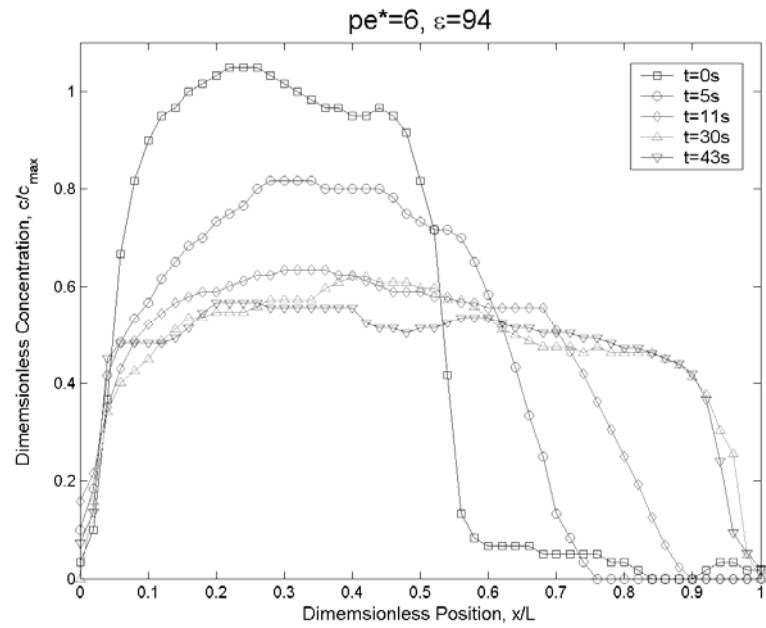


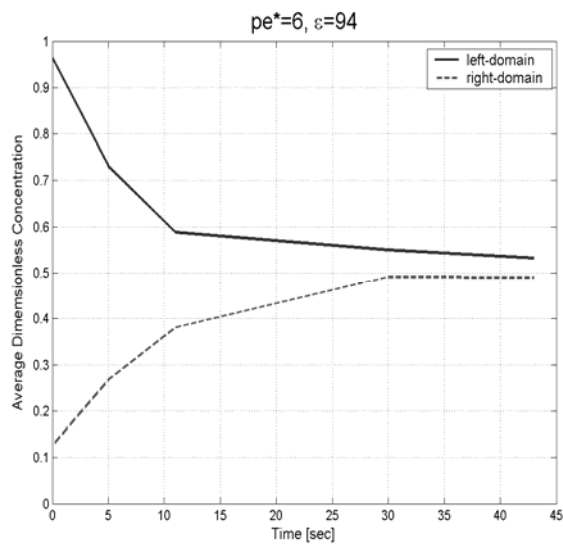
Figure 2-10. Convective Mixing Progress ( $Pe^*=132$ ).

(a) Average concentration profile at different times. (b) Concentration changes in two domains (c) Experimental photos of the drop during mixing at different times

(a)



(b)



(c)

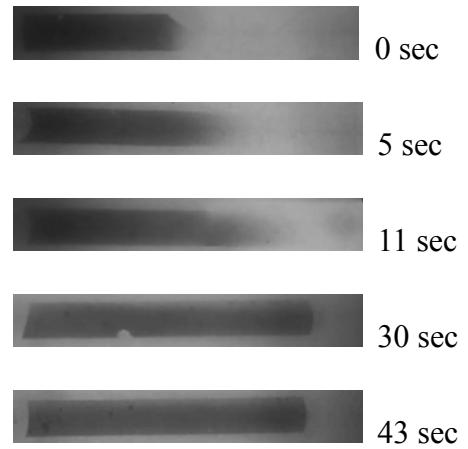
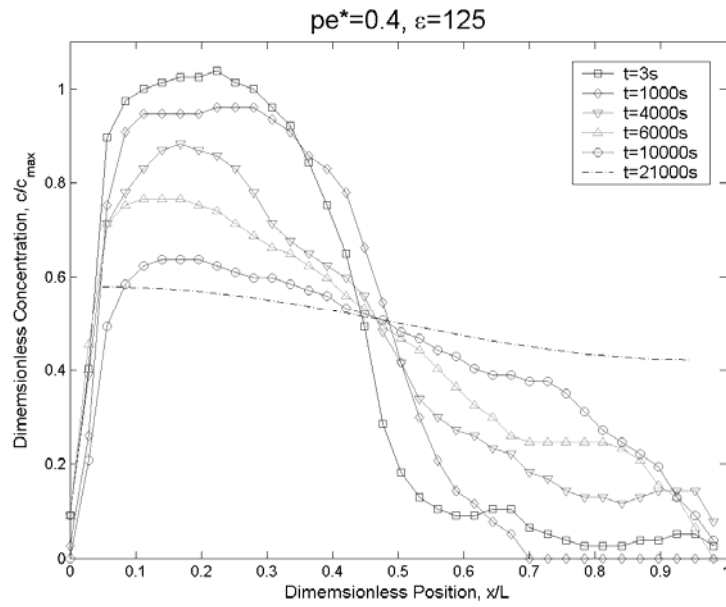


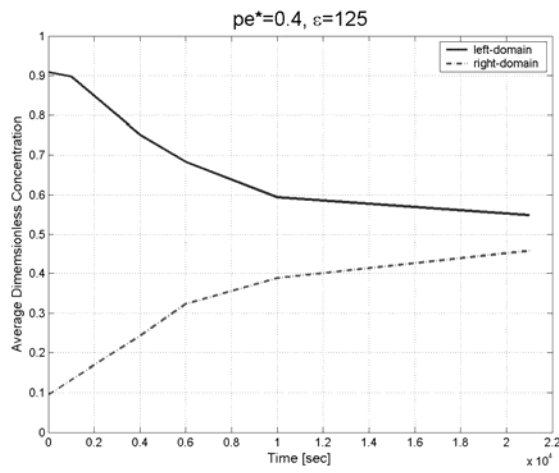
Figure 2-11. Dispersive Mixing Progress ( $Pe^*=6$ )

(a) Average concentration profile at different times. (b) Concentration changes in two domains (c) Experimental photos of the drop during mixing at different times

(a)



(b)



(c)

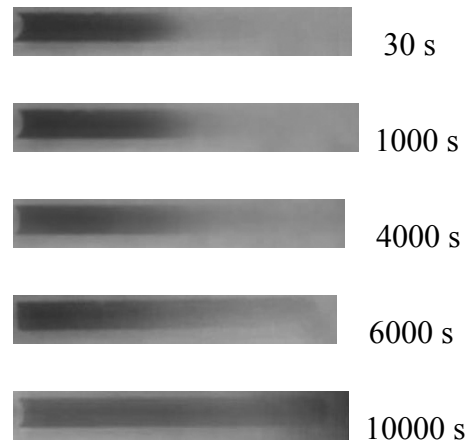
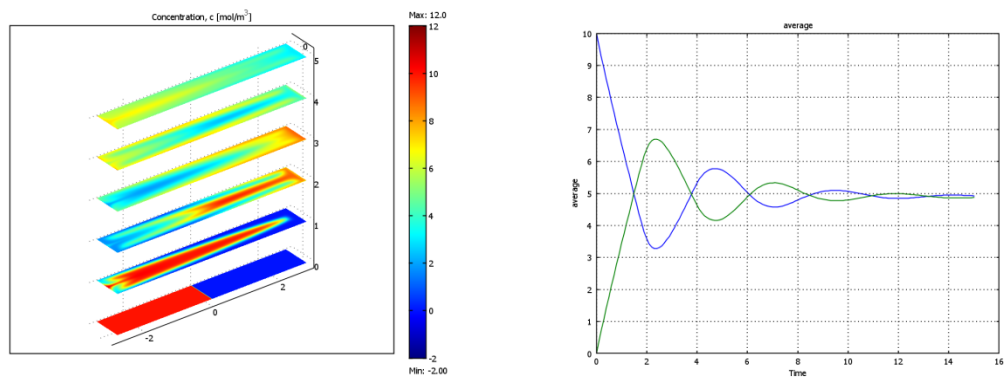


Figure 2-12. Diffusive Mixing Progress ( $Pe^*=0.4$ )

(a) Average concentration profile at different times. (b) Concentration changes in two domains (c) Experimental photos of the drop during mixing at different times

(a)



(b)

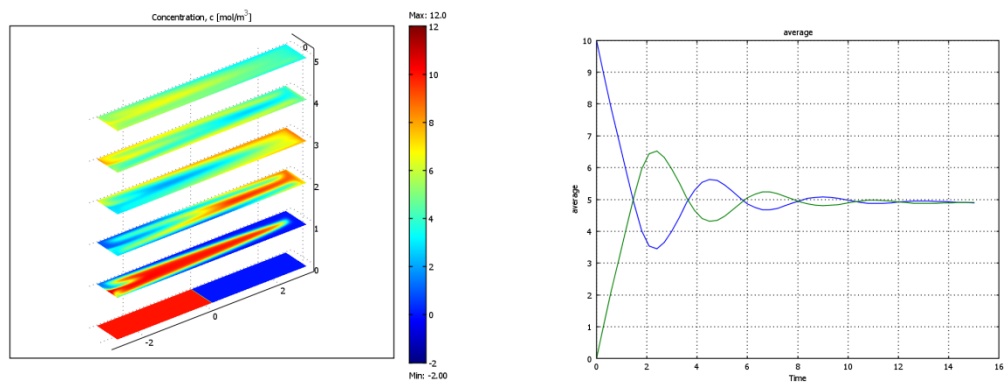


Figure 2-13. Comparison between a (a) straight and (b) curved channel ( $w=1\text{mm}$  and the radius of curvature= $4.2\text{mm}$ ) for  $Pe^*=100$  and  $\epsilon=7$ .

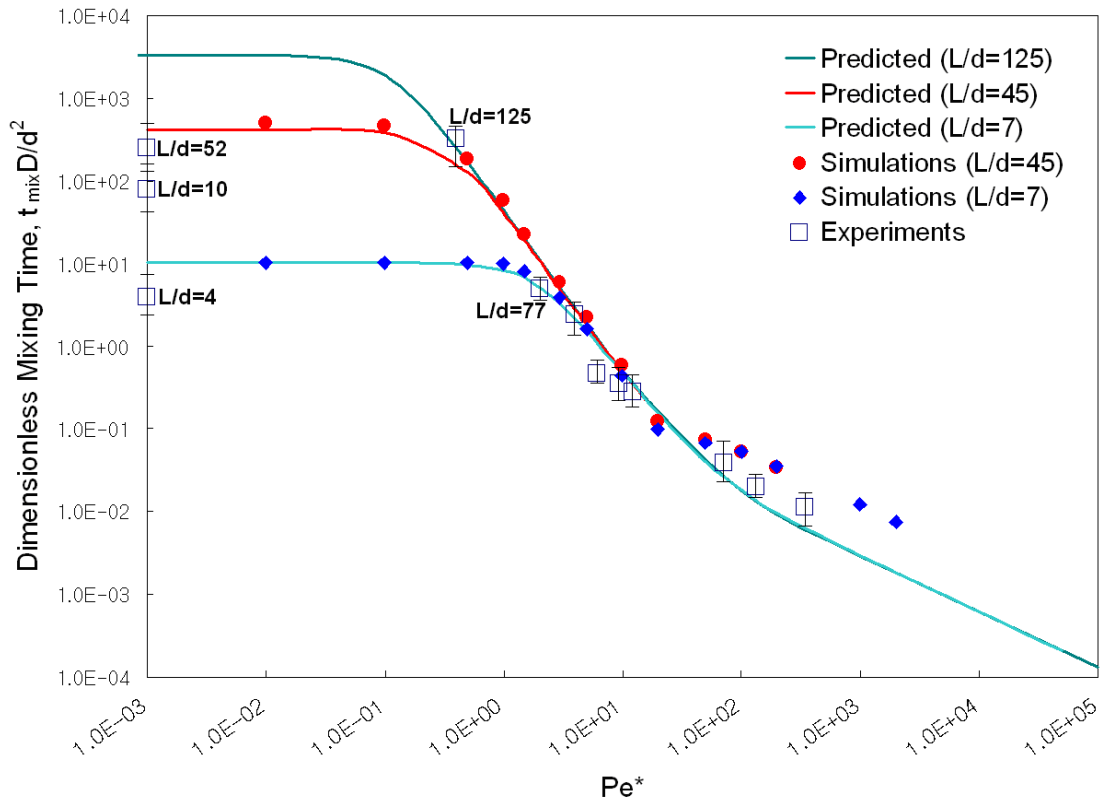


Figure 2-14. Mixing time comparison among theoretical predictions, simulations, and experimental results

## Appendix

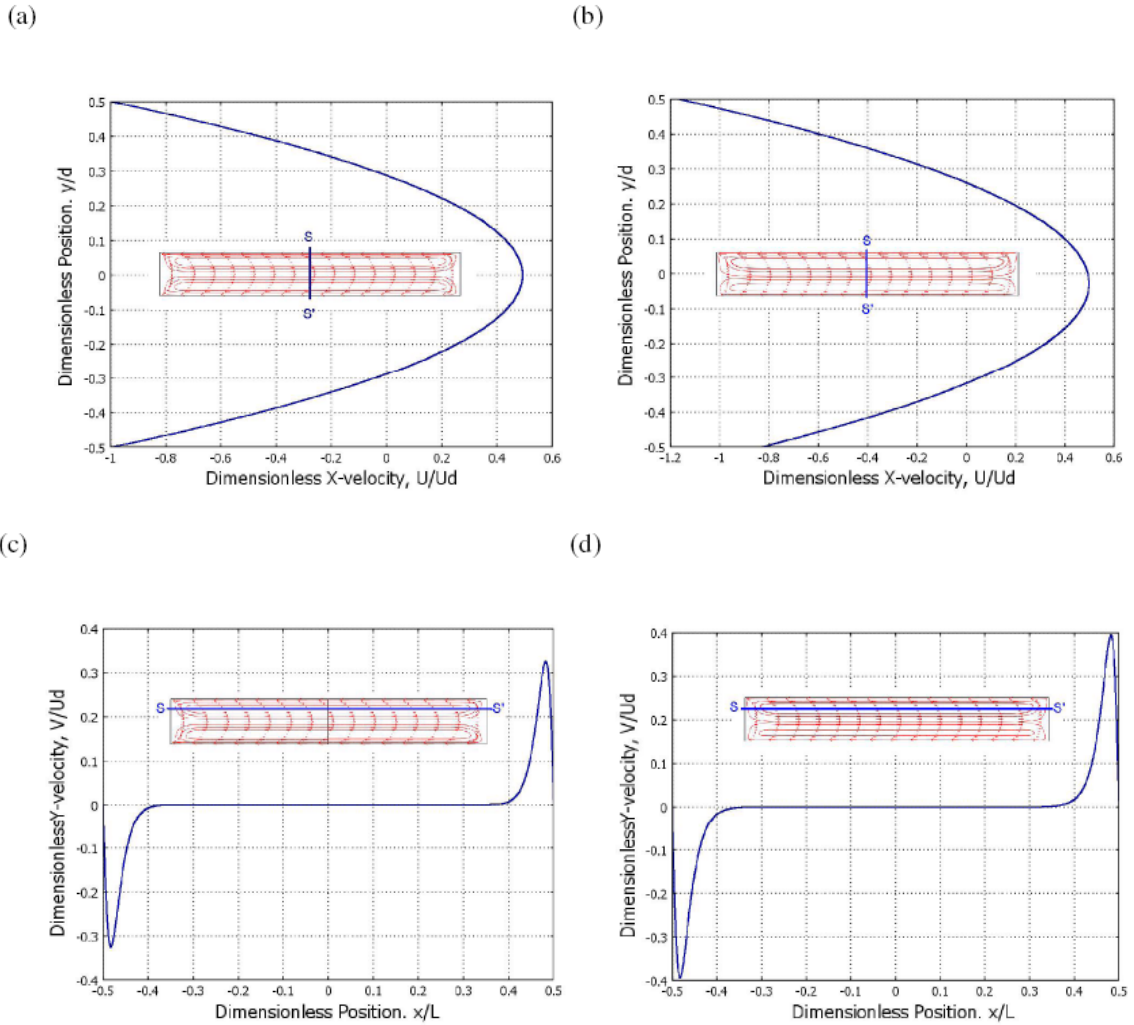


Figure 2-S1. Velocity profiles for a drop of  $\epsilon=7$  in straight and curved channels. (a)  $x$ -velocity (at  $x=0$ ,  $SS'$ ) in the straight channel. (b)  $x$ -velocity (at  $x=0$ ) in the curved channel ( $w=1\text{mm}$  and the radius of curvature= $4.2\text{mm}$ ). (c)  $y$ -velocity (at  $y/d=0.29$ ) in the straight channel. (d)  $y$ -velocity (at  $y/d=0.29$ ) in the curved channel. An approximately 17% increase from the straight-channel velocity at the outer wall and a 19% decrease at the inner wall result from the curved flow.

## References

- (1) Song, H.; Chen, D. L.; Ismagilov, R. F. *Angew. Chem. Int. Ed. Engl.* **2006**, *45*, 7336-7356.
- (2) Burns, M. A. *Science*. **2002**, *296*, 1818-1819
- (3) Burns, M. A.; Johnson, B. N.; Brahmastandra, S. N.; Handique, K.; Webster, J. R.; Krishnan, M.; Sammarco, T. S.; Man, P. N.; Jones, D.; Heldsinger, D.; Mastrangelo, C. H.; Burke, D. T. *Science* **1998**, *282* (5388), 484-487
- (4) Tanthapanichakoon, W.; Matsuyama, K.; Aoki, N.; Mae, K. *Chemical Engineering Science*, **2006**, *61*, 7386-7392.
- (5) Kamholz, A. E.; Weigl, B. H.; Finlayson, B. A.; Tager, P. *Anal. Chem.* **1999**, *71*, 5340–5347.
- (6) Hinsmann, P.; Frank, J.; Svasek, P.; Harasek, M.; Lendl, B. *Lab Chip*, **2001**, *1*, 16–21.
- (7) Wu, Z.; Nguyen, N. T.; Huang, X. Y. *J. Micromech. Microeng.* **2004**, *14*, 604–611.
- (8) Veenstra, T. T. *J. Micromech. Microeng.* **1999**, *9*, 199–202
- (9) Hadd, A. G.; Raymond, D. E.; Halliwell, J. W.; Jacobson, S. C.; Ramsey, J. M. *Anal. Chem.* **1997**, *69*, 3407–3412.
- (10) Walker, G. M.; Ozers, M. S.; Beebe, D. J. *Sensors Actuators B*, **2004**, *98*, 347–355.
- (11) Roder, H.; Shastry, M. C. R. *Curr. Opin. Struct. Biol.* **1999**, *9*, 620–626.
- (12) Kakuta, M.; Jayawickrama, D. A.; Wolters, A. M.; Manz, A.; Sweedler, A. V. *Anal. Chem.* **2003**, *75*, 956–960.
- (13) Burns, M. A.; Mastrangelo, C. H.; Sammarco, T. S.; Man, F. P.; Webster, J. R.; Johnson, B. N.; Foerster, B.; Jones, D.; Fields, Y.; Kaiser, A. R.; Burke, D. T. *Proc. Nat. Acad. Sci. USA.* **1996**, *93*, 5556-5561.
- (14) Pal, R.; Yang, M.; Lin, R.; Johnson, B. N.; Srivastava, N.; Razzacki, S. Z.; Chomistek, K. J.; Heldsinger, D. C.; Haque, R. M.; Ugaz, V. M.; Thwar, P. K.; Chen, Z.; Alfano, K.; Yim, M. B.; Krishnan, M.; Fuller, A. O.; Larson, R. G.; Burke, D. T.; Burns, M. A. *Lab Chip*, **2005**, *5*, 1024-1032.



- (15) Nguyen, N.; Wu, Z. *J. Micromech. Microeng.* **2005**, *15*, R1–R16
- (16) Ottino, J. M.; Wiggins, S. *Phil. Trans. R. Soc. Lond. A.* **2004**, *362*, 923–935
- (17) Knight, J. B.; Vishwanath, A.; Brody, J. P.; Austin, R. H. *Physical Review Letters*, **80**, 3863–3866.
- (18) Schwesinger, N.; Frank, T.; Wurmus, H. *J. Micromech. Microeng.* **1996**, *6*, 99–102.
- (19) Löb, P.; Drese, K. S.; Hessel, V.; Hardt, S.; Hofmann, C.; Löwe, H.; Schenk, R.; Schönfeld, F.; Werner, B. *Chem. Eng. Technol.* **2004**, *27*(3), 340–345.
- (20) Hessel, V.; Hardt, S.; Löwe, H.; Schönfeld, F. *AIChE Journal*, **2003**, *49*, 566–577.
- (21) He, B.; Burke, B. J.; Zhang, X.; Zhang, R.; Regnier, F. E. *Anal. Chem.* **2001**, *73*, 1942–1947.
- (22) Lin, Y.; Gerfen, G. J.; Rousseau, D. L.; Yeh, S. R. *Anal. Chem.* **2003**, *75*, 5381–5386.
- (23) Okkels, F.; Tabling, P. *Phys. Rev. Lett.* **2004**, *92*, 038301.
- (24) Liu, R. H.; Stremmer, M. A.; Sharp, K. V.; Olsen, M. G.; Santiago, J. G.; Adrian, R. J.; Aref, H.; Beebe, D. J. *J. Microelectromech. Syst.* **2000**, *9*, 190–197.
- (25) Wang, H.; Iovenitti, P.; Harvey, E.; Masood, S. *J. Microelectromech. Syst.* **2003**, *13*, 801–808.
- (26) Bertsch, A.; Heimgartner, S.; Cousseau, P.; Renaud, P. *Lab Chip*. **2001**, *1*, 56–60.
- (27) Vreeland, W. N.; Locascio, L. E. *Anal. Chem.* **2003**, *75*, 6906–6911.
- (28) Tice, J. D.; Song, H.; Lyon, A. D.; Ismagilov, R. F. *Langmuir* **2003**, *19*, 9127–9133
- (29) Burns, J. C.; Ramshaw, C. *Lab on a Chip*, **2001**, *1*, 10–15.
- (30) Bottausci, F.; Mezic, I.; Meinhart, C. D.; Cardonne, C. *Philos. Trans. R. Soc. London, Ser. A*, **2005**, *362*(1818), 10011–10018.
- (31) Tsai, J. H.; Lin, L. *Sensor Actuat. A–Phys.* **2002**, *97–98*, 665–671.
- (32) Oddy, M. H.; Santiago, J. G.; Mikkelsen, J. C. *Anal. Chem.* **2001**, *73*, 5822–5832.
- (33) Bao, H. H.; Zhong, J.; Yi, M. *Sensor Actuat B–Chem.* **2001**, *79*, 207–215.

- (34) Yang, Z.; Goto, H.; Matsumoto, M.; Maeda, R. *Sensor Actuat A-Phys.* **2001**, *93*, 266–272.
- (35) Hong, J. W.; Studer, V.; Hang, G.; Anderson, W. F.; Quake, S. R. *Nat. Biotechnol.* **2004**, *22*, 435-439.
- (36) Chou, H. P.; Unger, M. A.; Quake, S. *Biomed. Microdevices*, **2001**, *3*, 323-330.
- (37) Wang, J.; Sui, G.; Mocharla, V. P.; Lin, R. J.; Phelps, M. E.; Kolb, H. C.; Tseng, H. *Angew. Chem. Int. Ed.* **2006**, *45*, 5276-5281
- (38) Thorsen, T. ; Maerkl, S. J.; Quake, S. R. *Science*, **2002**, *298*, 580-584.
- (39) Handique, K.; Burns, M. A. *J. Micromech. Microeng.* **2001**, *11*, 548-554.
- (40) Duda, J. L.; Vrentas, J. S. *J. Fluid Mech.* **1971**, *45*, 247–260.
- (41) Kashid, M. N.; Garlach, I.; Franzke, J.; Acker, J. F.; Platte, F.; Agar, D. W.; Turek, S. *Industrial and Engineering Chemistry Research*, **2005**, *44*, 5003-5010.
- (42) Thulasidas, T. C.; Abraham, M. A.; Cerro, R. L. *Chem. Eng. Sci.*, **1995**, *50(2)*, 183-199.
- (43) Gorazd, B.; Albin, P. *Chem. Eng. Sci.*, **1997**, *52 (21/22)*, 3709-3719.
- (44) Van Baten, J. M.; Krishna R. *Chem. Eng. Sci.*, **2004**, *59*, 2535 – 2545.
- (45) Bringer, M. R.; Gerdts, C. J.; Song, H.; Tice, J. D.; Ismagilov, R. F. *Phil. Trans. R. Soc. Lond. A.* **2004**, *362*, 1087–1104
- (46) King, C.; Walsh, E.; Grimes, E. *Microfluid Nanofluid.* **2007**, *3*, 463–472
- (47) Xia, H. M.; Wan, S. Y. M.; Chew, Y. T. *Lab on a Chip*, **2005**, *5*, 748–755.
- (48) Duffy, D.; McDonald, J.; Schueller, O.; Whitesides, G. *Anal. Chem.* **1998**, *70*, 4974–4984.
- (49) Taylor, G., *Proc. R. Soc. London, Ser. A.* **1953**, *219*, 186-203.
- (50) Aris, R., *Proc. R. Soc. London, Ser. A.* **1956**, *235*, 67-77.
- (51) Gleeson, J. P.; Roche, O. M.; West, J.; Gelb, A. *SIAM J. Appl. Math.* **2004**, *64*, 1294-1310.

## **Chapter 3**

### **Membranous Bypass Valves for Discrete Drop Mixing and Routing in Microchannels**

#### **3.1 Introduction**

Rapid mixing in microfluidic systems is key to the effective functioning of biochemical processes in the devices [1-3]. However, in many microfluidic applications, rapid mixing is a major challenge because the time for diffusive mixing often exceeds processing times for other steps. This slow transport time scale can be thus a bottleneck for many high-throughput microfluidic assays.

Mixing is also one of the essential functions in lab-on-a-chip (LOC) platforms for complex chemical reactions [3-5]. Mixing in LOC microfluidic systems occurs not only in a continuous flow [6-8] but also must be controllable between two discrete drops in a batch operation. While most micromixers are used in continuous-flow systems, several studies have been reported on microfluidic mixing in batch systems [3-5, 9-10]. As opposed to continuous-flow systems, mixing in batch systems can be enhanced by convection [11]. During the course of drop transportation, the internal circulation streamlines of liquid in a moving discrete drop allows convective mixing as well as molecular diffusion. In addition, the isolated volume helps reduce axial dispersion along

the channel and contamination between sample volumes [12].

We present here a novel microfluidic component to facilitate discrete drop mixing in microchannels. This new component helps remove the air between the discrete drops that are initially isolated in different places in the channel. The merged drop then is dislocated at variously controlled velocities to accelerate mixing. By experimental verification, three different regimes are classified and compared with the theoretical modeling. Additionally, a membranous one-way check valve is introduced. The valve prevents liquid flow until the internal pressure reaches at a certain threshold pressure. The threshold pressure can be adjusted by geometry and thus one can make the valve allow the flow in one direction while stops the flow in the opposite direction.

### **3.2. Materials and Methods**

#### **Device Fabrication**

The prototypical mixing device was manufactured using the standard soft-lithographic technique [13]. The SU-8 (MicroChem) resist was spun on a bare silicon wafer to make the mold for fluidic channels and pre-baked on the hot plate for 5 min at the 65°C and for 20 min subsequently at the 95°C. After the exposure to 365 nm UV light, the coated wafer was post-baked for 1 min at the 65°C and for 10 min subsequently at the 95°C. The successive 15 min development resulted in the ~80µm thick mold. The depth and width of the channel were analyzed on a surface profiler (Alpha-Step 500, KLA-Tencor). A mixture of PDMS prepolymer and curing agent (5:1 w/w, Sylgard 184, Dow-Corning) was cast against the SU-8 mold and cured at 150°C for 18 min. The cured PDMS cast was carefully removed from the mold and diced into individual dies. For each

die, four injection holes were drilled by an aluminum needle. Meanwhile, a glass cover slide (Dow Corning) was spincoated with a 10:1 PDMS mixture and cured to have a thin (~50 $\mu$ m) PDMS layer on the glass side. To bond the device and the glass lid, the PDMS replica and the PDMS-coated glass slide were then oxidized in the UV ozone cleaner (Jelight Company, Inc.) for 25 min and brought into conformal contact at 85°C in a convective oven for 2 hours

### **Fluid Control and Image Acquisition**

Each injection port in the device was connected through syringes to a computer-controlled setup, which consisted of four sets of two-way solenoid valves (Numatech). Each solenoid valve could perform a pulsed air pressure (<3 psi) injection or a pulsed vacuum suction. The switches to pressure and vacuum were programmed and operated by LabView (National Instruments). Liquid reagents were also loaded via the syringes with aid of the computerized pressure control. The experiments were performed on the device oriented on a stage of a stereomicroscope (Olympus SZX12). During the mixing progress, in situ imaging was recorded using a digital camera (Nikon Coolpix 4500) with a capture rate of 30 frames/s and then transferred to the computer for further analysis.

### **Image Processing**

A blue dye (Trypan blue 0.4% solution, Sigma-Aldrich) and a colorless liquid (DI water) were used to characterize the mixing performance in this study. The luminance intensity images were recorded and transferred to the computer for evaluation. The RGB images captured were converted into grayscale images expressing only 256 levels of the

luminance. In order to rectify light disturbance, a reference background picture was used and the grayscale values of the mixing pictures were subtracted from the background picture. A computer program was written to analyze the luminance levels of the pixels along a line drawn at the center across the mixing channel. In order to remove the high frequency noise, the finite impulse response (FIR) filter was employed during the image processing. The recorded images were analyzed in a grayscale mode, the background image was subtracted from the image to eliminate intensity fluctuations, and high frequency noise was removed by finite impulse response (FIR) filtering.

### **3.3. Results and Discussion**

#### **Membranous air bypass valves**

The operation to align two drops sequentially in microchannels is not straightforward. To aid in drop positioning and merging, we developed two different membrane bypass valve (MBV) in PDMS: two-dimensional and three-dimensional. Each valve consists of a thin ( $\sim 30\mu\text{m}$ ) PDMS membrane facing the mixing channel and a separate bypass channel connected to atmosphere or a mild vacuum source. The membrane allows air to pass but not liquid. Figure 3-1 illustrates the use of two-dimensional MBV to coalesce two drops. The trapped air between two drops can be either drawn off through the membrane by a vacuum source connected to the MBV or by applying air pressure from the both ends to push two drops towards the center and the trapped air out to atmosphere. Similarly, three-dimensional MBV is shown Figure 3-2. The main mixing channel and the bypass channel are located in different layers, separated by a thin ( $\sim 30\mu\text{m}$ ) PDMS membrane layer. The trapped air now will be aspirated into

the above perpendicular channel where a vacuum source is connected.

The rate of air aspiration is dependent on the strength of vacuum connected to the bypass, the membrane thickness, the contact area of membrane interface, and the PDMS membrane porosity, which is affected by the mixing ratio of PDMS prepolymer and curing agent. Figure 3-3 shows the influence of membrane interfacial area and the applied vacuum strength on the aspiration rate. For three-dimensional MBVs we can flexibly control membrane interfacial area by changing the shape of both mixing and bypass channels. However, the membrane in two-dimensional MBVs has limited variation in interfacial area, since the membrane height in two-dimensional MBVs is confined to the channel depth, typically less than 100 $\mu\text{m}$ . While a two-dimensional MBV has its primary strength in more straightforward fabrication, it is less robust mechanically when high vacuum is applied.

### **The modified Péclet number**

The relative importance of convection to diffusion in mass transport is typically expressed as a dimensionless number, the Péclet number ( $Pe$ ), where  $Pe=U_d d/D$ . Since the time required for sufficiently complete mixing will depend on the drop height ( $d$ ) and velocity ( $U_d$ ) as well as the diffusion coefficient of the solute ( $D$ ), the Péclet number is useful to estimate the mixing time. To better explain the correlation between mixing and the aspect ratio, a modified Péclet number, has been suggested in our previous study [14]. When convective mixing occurs, convection and diffusion usually develop in different directions. Thus, for a drop with a high aspect ratio, the Péclet number provides insufficient information about the importance of convection and diffusion, mainly because the drop length ( $L$ ) is not considered in the Péclet number. The modified Péclet

number is defined by,

$$Pe^* = \frac{\text{diffusive time scale}}{\text{convective time scale}} = \frac{d^2/D}{L/U_d} = \frac{Pe}{\varepsilon} \quad (3.1)$$

Once the discrete drops get coalesced using the MBV, one can move the merged drop along the mixing channel at a set velocity to enhance mixing. For a given micromixer with fixed channel geometry and drop dimensions, one can alter the mixing condition ( $Pe^*$ ) by controlling the drop velocity.

### **Drop mixing in three different regimes**

The experimental mixing progress at a low  $Pe^*$  ( $\sim 0.4$ ) is shown in Figure 3-4a, starting from the initial state when the two drops fuse and an interface develops ( $t=0$  sec), to the state of complete mixing when the drop has traveled along the mixing channel. Figure 3-4a shows how the concentration of the merged drop changes during the mixing process when diffusion is dominating the mixing. The blue solid line represents the average concentration of the left domain that was initially occupied by the blue ink ( $c=c_{\max}$ ), and the green dotted line shows the average concentration of the right domain initially without the blue dye ( $c=0$ ). The merged drop has been displaced 63 mm for  $\sim 10000$  seconds back and forth along the channel but the mixing was quite incomplete. The extended time required for complete mixing can result in a significant loss of drop volume due to evaporation, since the drop will be exposed to air through the vapor-permeable PDMS top for hours. In addition, reduction in drop volume makes the concentration higher, possibly leading to inaccurate analysis of concentration data. The



volume loss may be reduced by saturating the device environment with excessive water that covers the device top as well as the sample inlets. The resulting sacrificial evaporation of the supplied water fairly reduces the sample evaporation rate, but approximately 10-20% volume loss was still observed during the experiment.

In the intermediate range of  $Pe^*$  (~6) (Figure 3-4b), however, the mixing occurs faster, and a different mixing mechanism, well-known Taylor dispersion, is observed. Because of this dispersive spreading, the mixing is greatly enhanced compared to purely diffusive mixing. Note that the concentration change for the dispersion-dominated mixing conforms to the behavior of diffusive transport but with a shorter timescale. When the modified Péclet number is small (Figure 3-4c), the merged drop travels fast and rapidly mixes within a few seconds due to the convective effects. In Figure 3-4a, the average concentrations of both domains are oscillating, and gradually converging due to the internal circulation and the concentrations gradually converge with time until complete homogenization. The presence of this oscillation confirms the convection-dominated mixing at  $Pe^*=132$ .

### **Comparison of mixing experiment results with theoretical modeling**

Figure 3-5 shows the plot of mixing time against the modified Péclet number for comparison of our experimental results with estimated curves from the theoretical modeling in our previous study [14]. Although the results are overall in good agreement with the theoretical modeling, it is important to note the slight discrepancy between the theoretical modeling and the experiment results. The underestimated mixing time (shorter mixing time than the theory predicts) is most likely due to the drop fusion mechanism using the MBV. At the moment when two discrete drops merge, they are

drawn to each other and thus forced to collide, causing the influence of convective drop transport. Therefore, the fused drop are prone to make a deeper interface, indicating a slight degree of mixing has been already begun in the interfacial area leading to the underestimation of mixing time. This pre-mixing can mislead the measurements for slow diffusive mixing, especially. On the other hand, the overestimated mixing time (longer mixing time than the theory predicts) may be attributed to the air control. For the pressure-driven flow in the mixing experiments, the pressure from one inlet was generated in a pulsed manner, and it is likely that the measured mixing time would include non-mixing time between pulses.

### **Membranous check valves for drop routing**

A one-way or check valve has become a concern in many microfluidic applications to perform tasks where backflow must be not allowed with minimal external operations. The microfluidic check valve is thus analogous to an electronic diode in function. While an electronic diode prevents current flow in one of the two directions in circuits, the fluidic check valve stops fluid flow in one direction. There have been many researchers who developed such valves that limit flow in one direction. Nevertheless, the use of such valves can be limited, since they involve a very complicated fabrication procedure due to their multi-layered design [15, 16] or the use of non-conventional materials [15, 17, 18].

Besides its unique bypass functionality, the MBV can also function as a check valve beyond its regular operational pressure (<2 psi). Depending on the pressure and membrane dimension, the membrane can be lifted and allow liquid to pass (Figure 3-6a). When the low pressure gets recovered, the membrane returns to its upright position

(Figure 3-6b).

Figure 3-7a shows that a drop of blue ink penetrates the membrane when high enough pressure has been applied. The threshold pressure can be defined as the minimum pressure applied to the membrane that can open the membrane. The shape of membrane significantly affects the threshold pressure. For instance, a round-shaped membrane in Figure 3-7b has a lower threshold pressure for the forward flow but a higher threshold pressure for the backward flow. In Figure 3-8, at a chosen appropriate pressure, the liquid could pass through the upper valve but not the lower valve, since the internal pressure was high enough to open the upper valve while the lower valve was still closed. This design using multiple check valves with different threshold pressures may allow for selective routing of liquid samples around in the device. For 20 $\mu\text{m}$  thick membranes, the flow rates were plotted against the pressure applied to the membrane, depending on the shape of membranes (Figure 3-9). The threshold pressures are observed when the flow rate is being recovered to conform its original relationship,  $Q=\Delta P/R$ , from zero.

The threshold pressure can be also increased by implementing a thicker membrane up to <50 $\mu\text{m}$ . However, the membrane valve thicker than ~50 $\mu\text{m}$  will not open without breaking the entire device, since the inherent bonding between the PDMS device and the substrate can withstand the threshold pressure of only 30-40 kPa inside the device. The membranous check valve is a single-layer, planar device that can be fully integrated with standard multi-layer soft lithography techniques. Unlike previously reported multi-layered check valves, this simple planar component can be freely arranged in any location and thus provide many design options in developing flexible microfluidic systems.

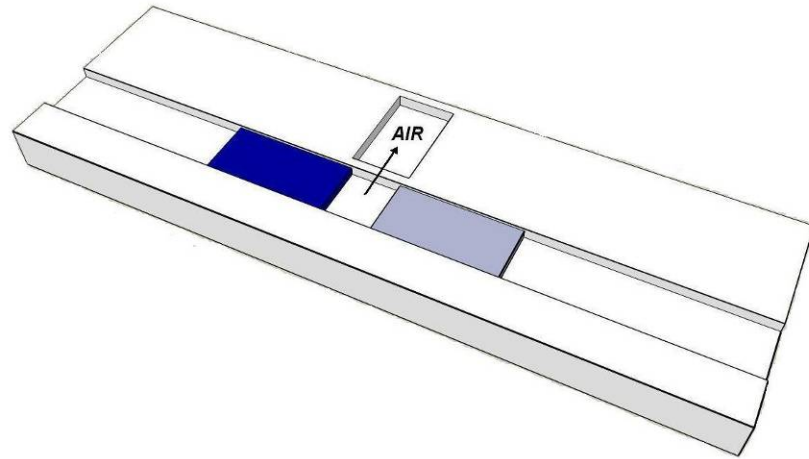
### 3.4. Conclusions

The membranous air bypass valve (MBV) structures were constructed and verified with mixing experiments. In lab-on-a-chip systems, merging two drops separated by trapped air is a challenging task. We developed two different membrane bypass valves (MBVs) in PDMS: two-dimensional and three-dimensional, respectively. The membrane in PDMS is air-permeable but prevents liquid leakage. Using the MBVs, we successfully removed the trapped air between the discrete drops and let the fused drop move at a desirable velocity to achieve effective mixing. Experimental mixing results using the MBV were in good agreement with the previous theoretical predictions. Additionally, the membranous check valve structure was investigated with routing examples. At appropriate pressures, the liquid could pass through the check valve but not at lower pressures. The planar nature of such check valves makes them particularly useful for full integration with other complicated microfluidic components.

### Acknowledgement

This chapter has been separately published in **Rhee, M.** and Burns, M. A. (2008). *Sensors and Transducers*, **3**: pp. 37-46.

(a)

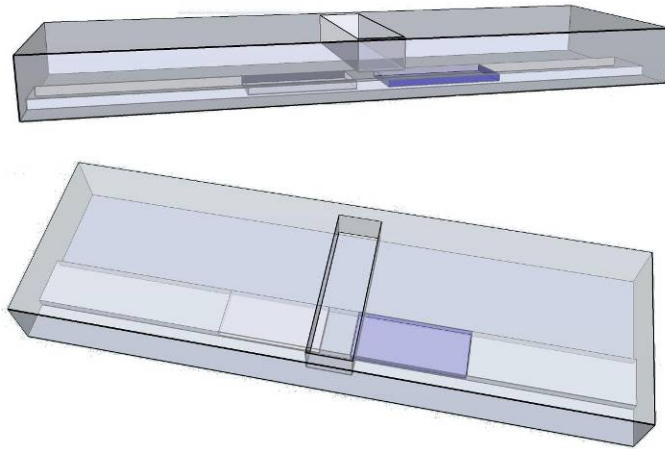


(b)

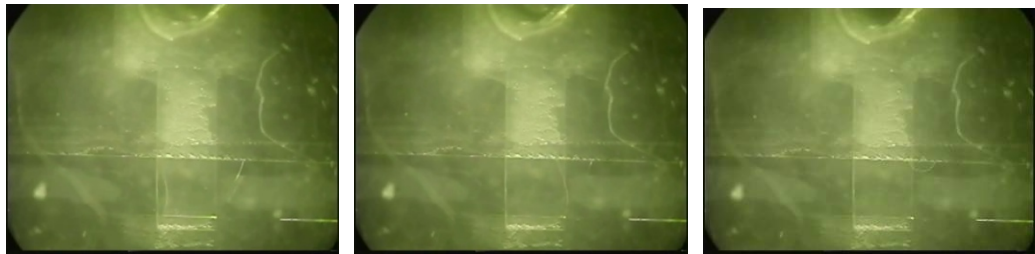


**Figure 3-1.** (a) A schematic of the use of 2D MBV to coalesce two drops. (b) The trapped air between two drops can be drawn off by a vacuum source connected to the MBV or by applying air pressure from the both ends to push two drops towards the center and the trapped air out to atmosphere via the MBV.

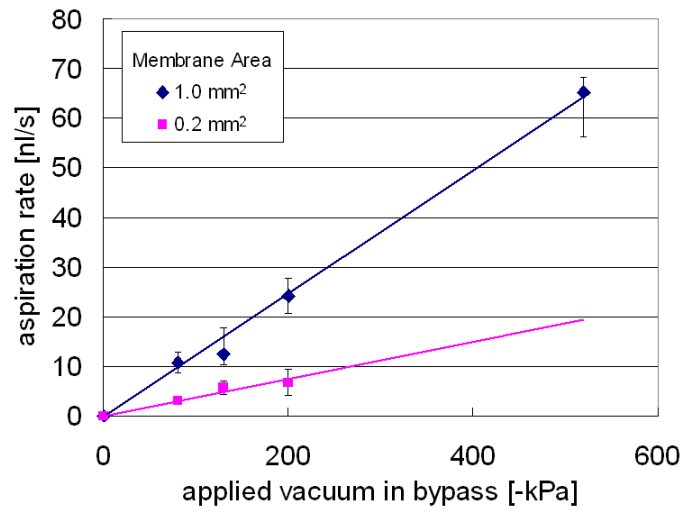
(a)



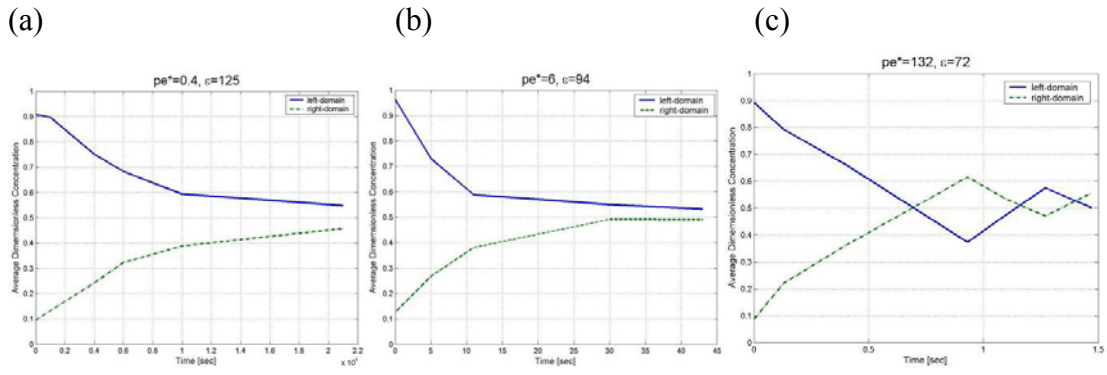
(b)



**Figure 3-2.** (a) A schematic of the 3D MBV to coalesce two drops viewed from the side and from the top. (b) The trapped air between two drops can be drawn off by a vacuum source connected to the MBV.

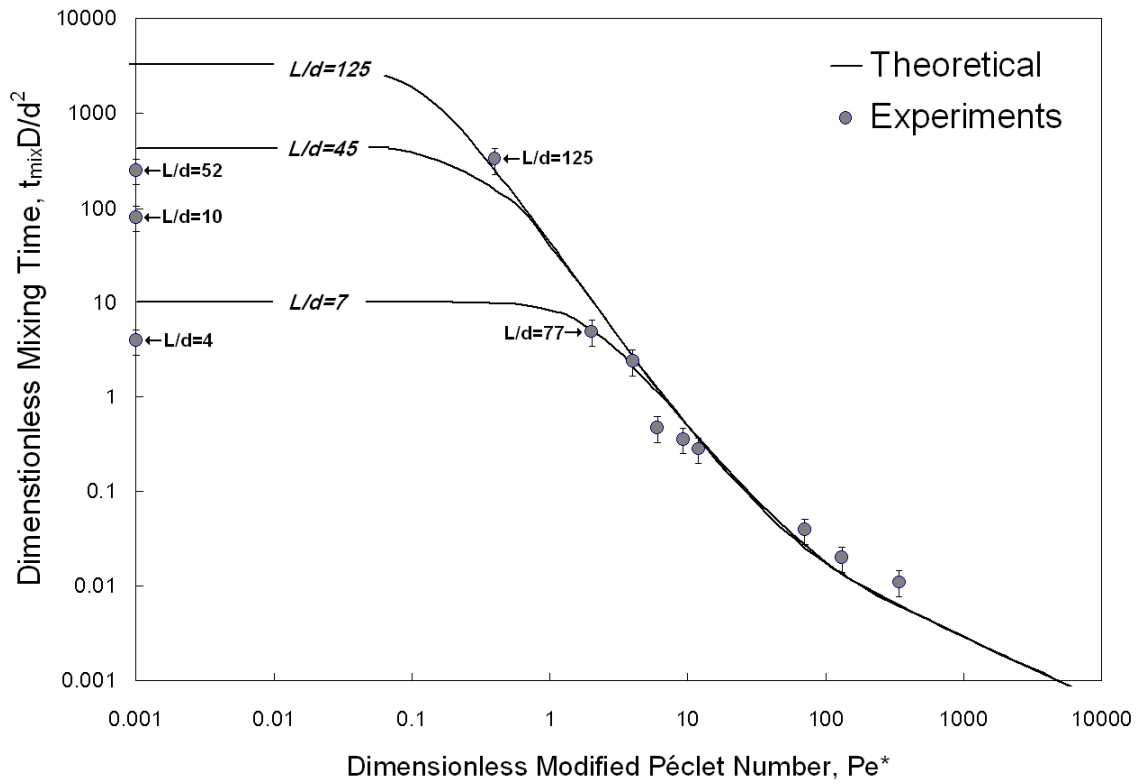


**Figure 3-3.** *The aspiration rate measurements with various membrane interfacial area and the applied vacuum strength*

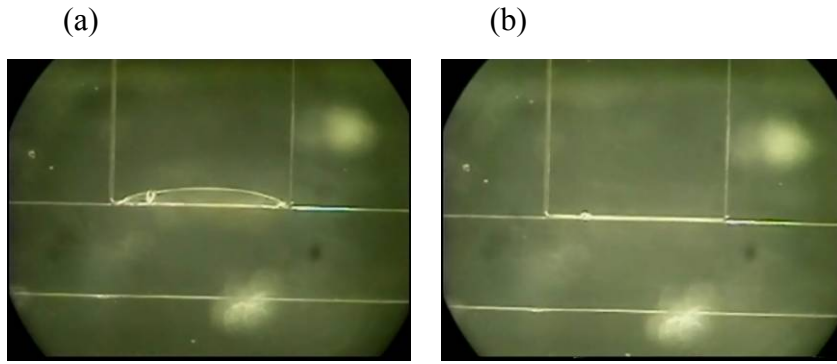


**Figure 3-4.** Average concentration changes in left and right domains (a) Diffusive Mixing Progress ( $Pe^*=0.4$ ) (b) Dispersive Mixing Progress ( $Pe^*=6$ ) (c) Convective Mixing Progress ( $Pe^*=132$ )

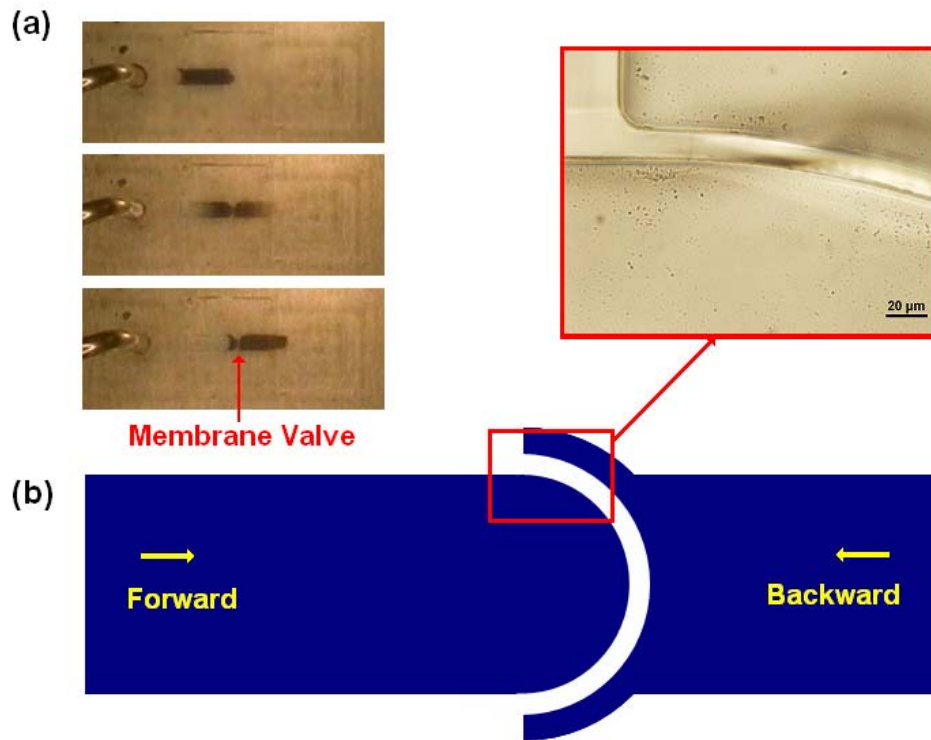




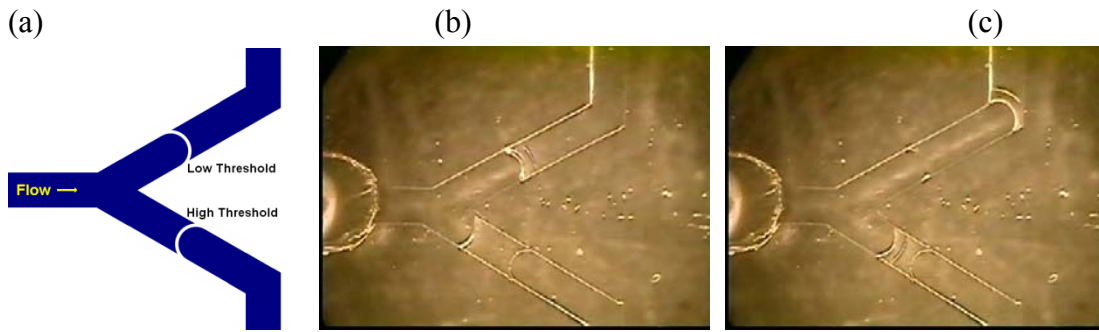
**Figure 3-5.** *Mixing time comparison among theoretical predictions, simulations, and experimental results*



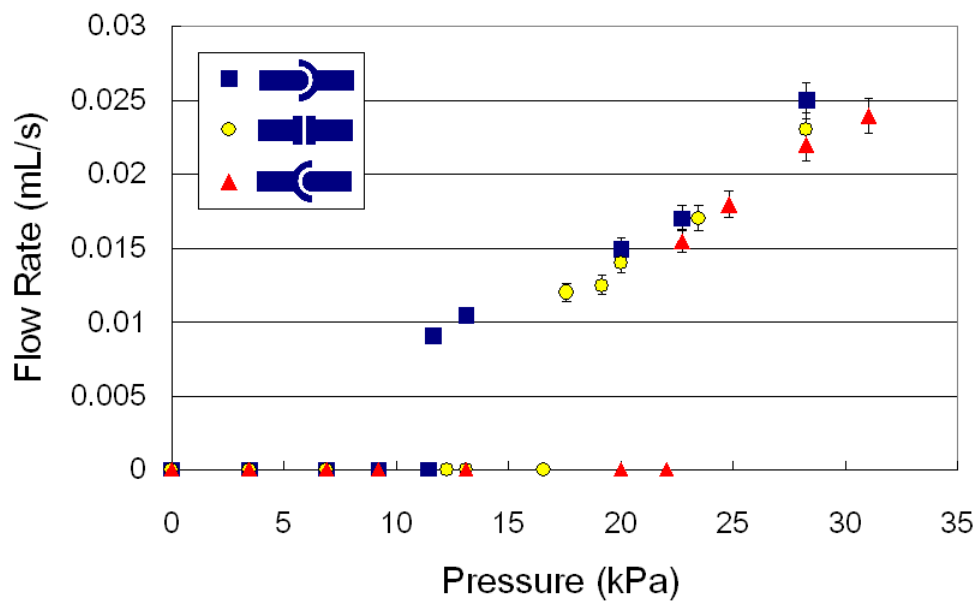
**Figure 3-6.** *Membranous Valve at different pressures applied: (a) open at >3 psi (b) closed at <1 psi.*



**Figure 3-7.** (a) A drop of blue ink penetrates the membrane check valve when high enough pressure has been applied. The device was assembled with microfluidic assembly blocks [19] (b) A round-shaped membrane of the thickness of  $20\mu\text{m}$ . The valve exhibits a lower threshold pressure for the forward flow but a higher threshold pressure for the backward flow.



**Figure 3-8.** *Selective Routing. (a) The route design with two check valves with different thresholds. (b-c) The liquid sample will continue past the upper low threshold valve but not the high threshold valve. At higher pressure, the drop will flow into both directions.*



**Figure 3-9.** A plot of flow rates against the internal pressure, depending on the shape of membranes.

## References

- [1]. Song, H.; Chen, D. L.; Ismagilov, R. F. Reactions in Droplets in Microfluidic Channels, *Angew. Chem. Int. Ed. Engl.* (45) (2006), pp. 7336-7356.
- [2]. Burns, M. A. Everyone's a (future) chemist, *Science*.(296) (2002), pp. 1818-1819.
- [3]. Burns, M. A.; Johnson, B. N.; Brahmasandra, S. N.; Handique, K.; Webster, J. R.; Krishnan, M.; Sammarco, T. S.; Man, P. N.; Jones, D.; Heldsinger, D.; Mastrangelo, C. H.; Burke, D. T. An Integrated Nanoliter DNA Analysis Device, *Science* (282), (1998), pp. 484-487.
- [4]. Burns, M. A.; Mastrangelo, C. H.; Sammarco, T. S.; Man, F. P.; Webster, J. R.; Johnson, B. N.; Foerster, B.; Jones, D.; Fields, Y.; Kaiser, A. R.; Burke, D. T. Microfabricated Structures for Integrated DNA Analysis, *Proc. Nat. Acad. Sci. USA.* (93) (1996), pp. 5556-5561.
- [5]. Pal, R.; Yang, M.; Lin, R.; Johnson, B. N.; Srivastava, N.; Razzacki, S. Z.; Chomistek, K. J.; Heldsinger, D. C.; Haque, R. M.; Ugaz, V. M.; Thwar, P. K.; Chen, Z.; Alfano, K.; Yim, M. B.; Krishnan, M.; Fuller, A. O.; Larson, R. G.; Burke, D. T.; Burns, M. A. An Integrated Microfluidic Device for Influenza and other Genetic Analyses, *Lab Chip*, (5) (2005), pp. 1024-1032.
- [6]. Hinsmann, P.; Frank, J.; Svasek, P.; Harasek, M.; Lendl, B. Design, simulation and application of a new micromixing device for time resolved infrared spectroscopy of chemical reactions in solution, *Lab Chip*, (1) (2001), pp. 16-21.
- [7]. Wu, Z.; Nguyen, N. T.; Huang, X. Y. Nonlinear diffusive mixing in microchannels theory and experiments. *J. Micromech. Microeng.* (14) (2004), pp. 604-611.
- [8]. Hadd, A. G.; Raymond, D. E.; Halliwell, J. W.; Jacobson, S. C.; Ramsey, J. M. Microchip Device for Performing Enzyme Assays. *Anal. Chem.* (69) (1997), pp. 3407-3412.
- [9]. Hong, J. W.; Studer, V.; Hang, G.; Anderson, W. F.; Quake, S. R. A Nanoliter-scale Nucleic Acid Processor with Parallel Architecture. *Nat. Biotechnol.* (22) (2004), pp. 435-439.
- [10]. Thorsen, T. ; Maerkl, S. J.; Quake, S. R. Microfluidic Large-scale Integration. *Science*, (298) (2002), pp. 580-584.
- [11]. Handique, K.; Burns, M. A. Mathematical Modeling of Drop Mixing in a Slit-type Microchannels. *J. Micromech. Microeng.* (11) (2001), pp. 548-554.
- [12]. Burns, J. R.; Ramshaw, C. The intensification of rapid reactions in multiphase systems using slug flow in capillaries. *Lab on a Chip*, (1) (2001), pp. 10-15.
- [13]. Duffy, D.; McDonald, J.; Schueller, O.; Whitesides, G. Rapid Prototyping of

- Microfluidic Systems in Poly (dimethylsiloxane). *Anal. Chem.* (70) (1998), pp. 4974–4984.
- [14]. Rhee, M.; Burns, M.A. Drop Mixing in a Microchannel for Lan-on-a-chip Platforms, *Langmuir*, (24) (2008), pp. 590-561.
- [15]. Wang, X.-Q.; Tai, Y.-C. A Normally Closed In-channel Micro Check Valve, in: 13th IEEE International Conference on MEMS (2000), pp. 68-73.
- [16]. Nguyen, N.-T.; Truong, T.-Q.; Wong, K.-K.; Ho, S.-S. Micro Check Valves for Integration into Polymeric Microfluidic Devices. *J. Micromech. Mircoeng.* (14) (2004), pp. 69-75.
- [17]. Seidemann, V.; Butefisch, S.; Buttgenbach, S. Fabrication and Investigation of In-plane Compliant SU8 Structures for MEMS and Their Application to Micro Valves and Micro Grippers. *Sens. Actuators A.* (97-8) (2002), pp. 457-461.
- [18]. Kim, D.; Beebe, D. J. A Bi-polymer Micro One-way Valve. *Sens. Actuators A.* (136) (2007), pp. 426-433.
- [19]. Rhee, M.; Burns, M.A. Microfluidic Assembly Blocks. *Lab On A Chip*, (8) (2008), pp. 1365-1373.

## **Chapter 4**

### **Microfluidic Assembly Blocks**

#### **4.1 Introduction**

Microfluidic systems have proven to be an advantageous platform for biological assays [1-5]. These systems benefit from reduced requirements for expensive reagents, short analysis times, and portability. However, the impact of microfluidics on science has not yet been fully realized. For microfluidic systems, a gap typically exists between the technology developers mostly in engineering and chemistry, and potential users especially in the life sciences. In general, significant time and expertise are required to develop customized microfluidic systems. The high cost and the level of expertise required for microfabrication deters such non-expert users from using microfluidic systems. Collaboration between microfluidic researchers and life scientists facilitate the advance of microfluidics, as does the existence of companies and academy-based microfabrication foundries where potential users may purchase customized microfluidic systems. However, such customized systems incur substantial initial costs and delays due to low volume production [6] and are less suited for prototyping or test set-ups.

Several researchers have addressed this gap between the developers and users of microfluidic systems, proposing simpler fabrication methods [7-11] as well as



construction of configurable systems [12, 13]. Duffy *et al.* introduced a method of using printed transparencies to replace the expensive chrome masks used in photolithography [7]. Direct printing to fabricate microfluidic channel molds has been also demonstrated [8, 9] and obviates the need for photolithographical mold fabrication. The fluidic channels fabricated in such fashions have a maximum height of  $\sim 10 \mu\text{m}$  and they may not be suitable for some biological applications with large cells. Larger channels can be made with solid object printing (SOP) and thermoplastics [10] although the minimum feature size is quite large ( $>250 \mu\text{m}$ ). Recently, Grimes *et al.* proposed using thermally shrinkable polystyrene sheets to directly print master molds, a clever technique that holds promise for channels in the 50-100  $\mu\text{m}$  range [11]. Instead of addressing simpler fabrication, Shaikh *et al.* focused on design flexibility [12]. They proposed a system-level microfluidic architecture that allows for easy customization. Similar modular microfluidic systems [13] have been also proposed by Grodzinski *et al.*

We demonstrate here an assembly approach for microdevice construction to facilitate the use of microfluidic systems by non-experts. Our approach involves fabrication of microfluidic assembly blocks (MABs) in PDMS followed by the construction of a full functioning microfluidic system by assembling the blocks. Assembly blocks act as basic building units to form custom devices. Each MAB has an own unique function including inlet/outlets, valves, straight/curved/bifurcated channels, and chambers. Mass production of identical blocks is also possible in a regular lab environment. Once the assembly blocks are fabricated, they can be sent to non-expert users who can assemble devices with the blocks in minutes without the need for expensive design software or clean-room facilities.

## 4.2. Materials and Methods

### Mold Fabrication

The prototypical MABs were manufactured using the standard soft-lithographic technique [14]. The overall fabrication process is depicted in Supplementary Figure 4-S1. The proposed SU-8 master mold for MAB fabrication consists of thin patterns (~ 75 to 150  $\mu\text{m}$ ) for channel network and thick patterns (~ 500 to 1200  $\mu\text{m}$ ) for grid walls. To fabricate the patterns for fluidic channels first, the SU-8 2025 (MicroChem) resist was spun on a bare silicon wafer and pre-baked on the hot plate for 5 min at the 65°C and for 20 min subsequently at the 95°C. Approximately 75  $\mu\text{m}$  thick patterns could be obtained when the spin coating was done once. After the exposure to 365 nm UV light, the coated wafer was post-exposure baked for 1 min at the 65°C and for 10 min subsequently at the 95°C. The successive development in SU-8 developer solution (MicroChem) resulted in the channel patterns with desired thickness. The thickness and width of the patterns were analyzed on a surface profiler (Alpha-Step 500, KLA-Tencor). After cleaning the surface of silicon wafer with the channel patterns in it, the same SU-8 resist was spun and pre-baked repeatedly until the desired thickness was obtained. The wafer then was carefully aligned to a chrome photomask patterned with grid walls as well as cross alignment marks. The size of grids was chosen from 4mm by 4mm up to 8mm by 8mm. The thickness of grid walls was measured with a mechanical height gauge (Mitutoyo).

### Block Fabrication

Once the SU-8 master mold was prepared, a mixture of PDMS prepolymer and curing agent (9:1 w/w, Sylgard 184, Dow-Corning) was cast against the multi-layered

mold. We slightly tilted the mold and scratched the excessive PDMS solution off, using a commercial razor blade. The mold was then moved to a flat surface and cured at 150°C for 15 min. Each cured PDMS block was carefully removed with a sharp aluminum needle from individual cells separated by the grid walls. For inlet blocks and modules, injection holes were drilled by an aluminum needle. To fabricate the bottom layer of pneumatic valve modules, channels were patterned with a ~75  $\mu\text{m}$  thickness, and a 10:1 PDMS mixture was cast and spun to have a ~150  $\mu\text{m}$  PDMS layer. The valve patterns in the thin layer were diced to fit to the upper valve module. The two layers then were carefully aligned under microscope and reversibly bonded to each other.

### **Block Assembly**

To prepare substrates on which blocks are assembled, glass cover slides (Dow Corning) were spincoated with a 10:1 PDMS mixture and cured to have a thin (~100  $\mu\text{m}$ ) PDMS layer on the glass side. In accordance with the design to be realized, we started with selection of proper MAB. The selected blocks then were carefully aligned and assembled together. Using a pair of tweezers, we put a block together as tightly as possible by horizontally pushing and releasing it toward the block that had been already placed on the substrate. Visual aids such as a high magnification stereoscope were utilized to further facilitate the alignment procedure.

### **Fluid Control and Image Acquisition**

Each injection port in the inlet blocks was connected through syringes to a computer-controlled setup, which consisted of sets of two-way solenoid valves (Numatech). Each solenoid valve could perform a pulsed air pressure injection or a

pulsed vacuum suction. The switches to pressure and vacuum were programmed and operated by LabView (National Instruments). Liquid reagents were also loaded via the syringes with aid of the computerized pressure control. The experiments were performed on the device oriented on a stage of a stereomicroscope (Olympus SZX12). For evaporation tests, the inlets and outlets were sealed with glass slits (Dow Corning). To exclude any effects of humidity and temperature, all devices were kept at the same location throughout the experiments. During the demonstrative fluidic experiments such as mixing and pneumatic valve operation, in situ imaging was recorded using a digital camera (Nikon Coolpix 4500) with a capture rate of 30 frames/s and then transferred to the computer for further analysis. A blue dye (Trypan blue 0.4% solution, Sigma-Aldrich) and an orange liquid (fluorescein) were used to characterize the mixing performance in the study. The luminance intensity images were recorded and transferred to the computer for evaluation. The RGB images captured were converted into grayscale images. The grayscale images were further corrected from the background intensity. A computer program was written to analyze the luminance levels of the pixels along a line drawn at the center across the mixing channel.

### **Cell Culture**

To perform the cell culture in the microdevice, we prepared green fluorescent protein (GFP) expressing E. Coli cells induced by arabinose. The GFPs were inserted into pET24a plasmid. The prepared bacteria cells were mixed with the culture media (Luria-Bertani, 20g/L) containing ampicillin and inserted into the microculture system by a syringe. The microculture device was then brought and kept in the reactor at the constant temperature of 36°C. The fluorescent cell images recorded from the microscope

(Olympus BX51) were moved to a computer for further analyses.

### **4.3. Results and Discussion**

#### **Microfluidic Assembly Block Concept**

We have constructed microfluidic assembly blocks (MABs) that can be selectively assembled into a custom microfluidic device within minutes at the site of use. To construct a microfluidic device, MABs are selected from a standard set of components (Table 4-1) and then assembled to form the desired channel network, as shown in Figure 4-1. Note that the block fabrication and the device assembly can be done at different locations. While the MABs are fabricated by trained engineers who have expertise on sophisticated microfabrication processes, the custom devices are readily assembled by non-expert users. Noticeably, the majority of recent microfluidic needs in the life sciences requires a very simple design of channel network and relatively wide channels. A variety of standard MABs can be produced at low cost and in large quantities, and the custom devices rapidly can be designed, assembled, and tested.

Fabrication of the MABs involves a multi-step lithography to construct the SU-8 master mold. The mold consists of thin channel patterns and thick grid patterns up to 1200  $\mu\text{m}$  in height. To achieve this thickness, multiple repetitions of spin-coating and pre-baking were incorporated [15] (Figure 4-S2). The MAB mold is then used to form the individual PDMS assembly blocks. Figures 4-2a-c show a photo of the constructed SU-8 master mold, the resulting square MABs, and a simple exemplary device assembled on a glass slide. The MABs are designed such that they can be rotated in 90° increments if a different orientation is needed. Since the coated SU-8 layer was very viscous and thick,

the spin coating tended to produce slight variations in thickness around the entire wafer. This non-uniform thickness of the grid walls resulted in fabricated blocks with a small variation in thicknesses (Figure 4-S3). However, the variation in block thicknesses does not affect the assembly process. Modifications in block shapes can further change their fabrication and assembly characteristics (see the appendix).

### **Bonding and Sealing**

The mixing ratio of PDMS prepolymer and curing agent is crucial to be able to smoothly peel the blocks from the mold. A mixing ratio greater than 10:1 resulted in elastic and flimsy blocks that ruptured during peeling. In contrast, 5:1 or smaller mixing ratios caused the blocks to tightly adhere to the mold, resulting in block damage during forced extraction. However, when such a low ratio is required, silanization of the mold may help facilitate the removal process [16]. Note that, since the SU-8 grid walls are very robust, the removed PDMS blocks have clean and flat vertical edges on their sides.

To assemble MABs into a working microfluidic device, the selected blocks are aligned on a substrate in accordance with the user's design. We investigated two types of substrates; a bare glass slide and a PDMS coated glass slide. The adhesion to both these substrates is reversible and can withstand inside pressures up to 5 psi [17], a pressure high enough to perform typical pneumatically driven flow experiments in biochemical studies. With a simple tweezer manipulation, a fairly good contact between blocks (inter-block gap less than 5  $\mu\text{m}$ ) could be repeatedly achieved within seconds (Figure 4-2d). Although all the blocks have clean vertical sides, it is important to minimize the unavoidable gaps. Visual aids such as a stereoscope are not necessary but facilitate the alignment procedure.

In addition to the bonding between the blocks and the substrate, the inter-block bonding should be hermetic to prevent liquid loss. Since the side interfacial area of each MAB available for bonding is small, the inherent adhesion on the sides of each MAB is not the major component for block-to-block adhesion, even though two adjacent blocks formed gapless contact. The substrate-block bonding and the elastic nature of the PDMS combine to add an additional horizontal compressive force to seal the component connections.

The loss of liquid from the channels is an important consideration in this and all PDMS devices. Even if every connection between blocks is hermetic, evaporation will still occur by diffusion through the top membrane of the channel. To address the time elapsed in evaporation through the PDMS, we introduced a dimensionless diffusion time to directly compare the evaporation results from various devices with different device thicknesses. The dimensionless time,  $\tau$ , is defined as,

$$\tau = \frac{t \cdot D}{h^2}. \quad (4.1)$$

In the above equation,  $t$  is the elapsed time,  $D$  is the estimated diffusion coefficient of water vapor through PDMS membrane ( $D \sim 10^{-3} \text{ mm}^2/\text{s}$ ), and  $h$  is the membrane thickness corresponding to the difference between the device thickness and the channel thickness ( $h$  ranges from 300 to 1100  $\mu\text{m}$ ). To address leakage out of imperfections in block-to-block bonding, we used a ratio of exposed interface area per fluid volume (IF) as a parameter:

$$IF = \frac{\sum_i A_i}{V} \quad \text{where } A_i = g_i \times (w + 2d) \text{ and } V = lwd \quad (4.2)$$

In this equation,  $A_i$  indicates the interfacial area exposed to air at the  $i$ -th junction and  $V$  represents the total volume of fluid sample.  $A_i$  is calculated using the average gap distance ( $g_i$ ), the channel width ( $w$ ), and the channel thickness ( $d$ ). Likewise, the fluid volume is calculated from the drop length ( $l$ ) of fluid sample and the channel dimensions. Larger IF values indicate more exposure to air at junctions. Figure 4-3a shows the effect of inter-block gaps on the evaporation rate and confirms that the gaps introduced by the MAB assembly procedure have only a minor effect on the evaporation rate.

In addition to the inherent adhesion of placing MABs on a substrate described above, we also investigated a number of other bonding techniques (Supplementary Table 4-S1). We used three adhesive substances (the PDMS mixture used to fabricate the blocks, the PDMS curing agent, and a UV-curable glue) to increase the block/block bonding. When placed around the device in contact with the blocks, the adhesive substances flow into the interfacial gap between the device and the substrate due to capillary action. Curing the adhesive then resulted in strong bonding between the surfaces (Figure 4-2e). Interestingly, the curing agent filled in inter-block gaps appeared to exhibit another advantage of further reducing the evaporation rate as shown in Figure 4-3b. Apparently, the curing agent produced denser cross-linking during polymerization than the 9:1 PDMS mixture.

### **Block Shapes**

The square block system proposed in this study has several obvious strengths in



its application, the greatest of which is that the fabrication, mold design, and block removal is straightforward. Moreover, since there are no features added to the block for such purposes as alignment, the entire block surface area can be used for fluidic structures, thus minimizing dead volume. Additionally, these square blocks are designed to have minimal interface area when two blocks are connected. As the interface area decreases, the assembly will be more straightforward and thus require less elaborate techniques to bond. The sides of square blocks are easy to clean, minimizing the effects of residual polymer and common dust.

Nevertheless, one drawback of the assembly methodology with plain square blocks rather comes from the lack of alignment keys. Slight deviations in just a few blocks may cause an overall alignment problem, especially for a large assembly task. Another applicable method for improved assembly is to constrain the blocks in pre-defined areas. The areas are created in PDMS by separately constructing a base structure that can carry a certain number of blocks. Figure 4-4a-c show one of the block-and-base approaches using cross-shaped alignment posts in PDMS and SU-8. Such alignment posts tightly confine the block position to enhance alignment.

Figure 4-4d, 4-4e, and 4-4f illustrate another block-and-base approach with a channeled base and roofed blocks. This channeled base not only defines the position of blocks by PDMS grid walls but also has interconnecting channels for each block in four directions. The resulting areas can hold the blocks in alignment but the interface area will be increased by twice, since the blocks will interface with the channeled wall rather than contact each other. The roof structure on a block acts as a cover to seal the interconnecting channel. Despite its unique merit of improved sealing, the roofed blocks cannot be assembled independently without a base structure; users must always use the

corresponding base for assembly. Another challenge is increased complication during fabrication. To create the roofed blocks, three different photomasks are needed; one for the channel network, the other for the body parts of blocks, and another for the roof parts of blocks. While each part must have a different thickness, the thickness of the body parts must be balanced with the thickness of the base. Noticeable differences in thicknesses, if any, can cause vertical gaps between the blocks and the base, resulting in poor sealing. Overall, these block-and-base systems require more careful fabrication procedures to ensure a perfect fit between the blocks and the corresponding areas in the base. If blocks are much bigger than the designated areas, the blocks will not be properly inserted; on the other hand, if the blocks are smaller, inter-block gaps will be problematic. Various block shapes and their assembly characteristics are listed in Supplementary Table 4-S2.

## **Applications**

We have used MABs to prototype a variety of microfluidic devices. In addition to fluidic channels, a common component used in microfluidic systems is a PDMS pneumatic valve to control fluid flow<sup>18</sup>. We developed an MAB of two square-block size containing a microvalve that was designed according to previous reports<sup>19, 20</sup>. Figures 5a-d demonstrate the use of working valve blocks; the valve in this MAB is closed at rest and open when vacuum is applied. Since the valve must always accompany a connection port to a vacuum source, a valve and an inlet have been modularized together (See the supporting online material). To verify its function when embedded in a device, we demonstrated a simple mixing channel network consisting of three inlet/outlet blocks, a Y-channel block, and two valve modules. When the valve is open, fluid passes through the valve to the outlet where vacuum is applied. With the valve closed, no fluid flows

although a portion of the fluid sample will remain since the closed valve will not prevent complete liquid evacuation. After the valve opens again, the fluid resumes to be drawn to the outlet. Such valve modules can be assembled with any components in the device where precise fluid control is needed and thus provide flexibility in designing complex custom devices.

As another example, we used MABs to construct a microculture system for bacterial cells. The system used two inlet blocks for sample/media injection and a cell culture module occupying the space corresponding to six square blocks. Figure 4-6a shows the successful culture results of *E. Coli* cells in the assembled microculture system. Increases in the number of grown cells were clearly shown in Figure 4-6b.

In a micro-scale environment, the addition of two streams in laminar flow results in a clean boundary between streams. A complex system using the zigzag modules to generate molecular gradients is conceptualized in Figure 4-7a. To show the working principles of such assembly, a simpler system is illustrated in Figure 4-7b that mixes the blue dye and water into an outgoing stream. The cross-sectional profile in Figure 4-7c shows a distinct gradient of blue dye concentrations at AA'. For the device, two inlet MABs were used in conjunction with a Y-channel block for merging two streams, a zigzag channel module, and an outlet block. The use of MABs can be also extended to complex biochemical assays. The conceptualized large-scale integration in Figure 4-8a illustrates a system that can perform twenty independent assays simultaneously from one sample. An independent assay unit similar to that in the above integrated device is shown in Figure 4-8b. Each unit device can perform reagent mixing, PCR, restriction digest reaction, and a separation.




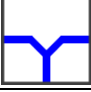
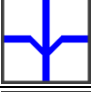

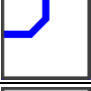

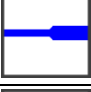

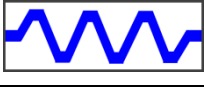

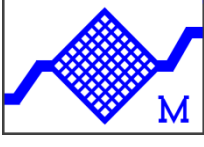
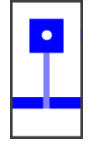
## 4.4 Conclusions



The MAB system provides a simple way for non-fluidic researchers to construct custom, complex microfluidic devices. There are several unique advantages of the MAB approach for microfluidic device constructions. The MAB approach is also ideal for selective surface modification or treatment limited to a specific section of the total device. Besides, there are no intrinsic limits in the channel thickness and the feature size. The MABs fabricated in PDMS exhibit enough durability that the blocks could be used multiple times. Non-treated square blocks were recovered six months after the initial assembly and successfully reused for a new assembly. Most importantly, the developers of MAB can manufacture a standard set of MABs that can be assembled into various custom devices. The MAB allows for full flexibility in planar configuration. The exemplary assembled devices demonstrated that the technology can be able to be used in a wide variety of applications. Non-experts users can practically mix and match the blocks to build their device with any configurations. Consequently, the proposed MAB methodology would be suitable for the recent needs since such devices with a simple configuration can be constructed within minutes in a regular laboratory environment.

## Acknowledgement

This chapter has been published in M. Rhee, M. A. Burns, *Lab Chip* **8**, 1365 (2008).

Table 4-1. Exemplary Standard Microfluidic Assembly Blocks in the study

Block Name	Schematic	Size	Function or Purpose
Inlet/Outlet		1x1	To connect the device to external tubing. The size of a hole varies. The width of a connecting channel varies.
Straight Channel		1x1	To form a plain straight channel. The channel width and height may vary.
T Channel		1x1	To add a side stream to the main stream or divide an incoming stream into two outgoing streams at 90°.
Y Channel		1x1	To merge two incoming streams to form a fused outgoing stream or divide a stream into two streams at 45°.
Ψ Channel		1x1	To merge three incoming streams to form a fused stream or divide a stream into three outgoing streams.
Cross Channel		1x1	To merge or divide stream(s) The channel width and height may vary.
90° Curved Channel		1x1	To form a 90° turn in a stream. The channel width and height may vary.
Chamber (small)		1x1	To collect samples or secure a reaction
Connector		1x1	To connect two blocks with channels of different widths
Spacer		1x1	To fill blanks between blocks or obstruct one end of a channel.
Zigzag Mixer		1x3	To enhance advective mixing in the stream. The channel geometry and width may vary. Used in molecular gradient generators.
Long Channel		1x3	To form a long plain straight channel. The channel width and height may vary. Used as separation channels.
Culture Bed		2x3	To provide separate room for cell culture. The size of a bed may vary. Patterns in the chamber may vary.
Pneumatic Valve		2x1	To control flow or separate an adjacent compartment. The valve is closed at the normal condition and opens when vacuum applied. Dark blue represents the upper layer and light blue represents the bottom layer.

Membranous Bypass Valve		2x1	<p>The Membranous bypass valve is made of a thin (&lt;math&gt;&lt;30 \mu\text{m}&lt;/math&gt;) PDMS membrane. The valve allows air to pass, but stops liquid (not to scale in the schematic). Used for fusion of two discrete drops.</p>
Chamber (large)		2x2	<p>To collect samples or secure a reaction. Used for on-chip PCR.</p>

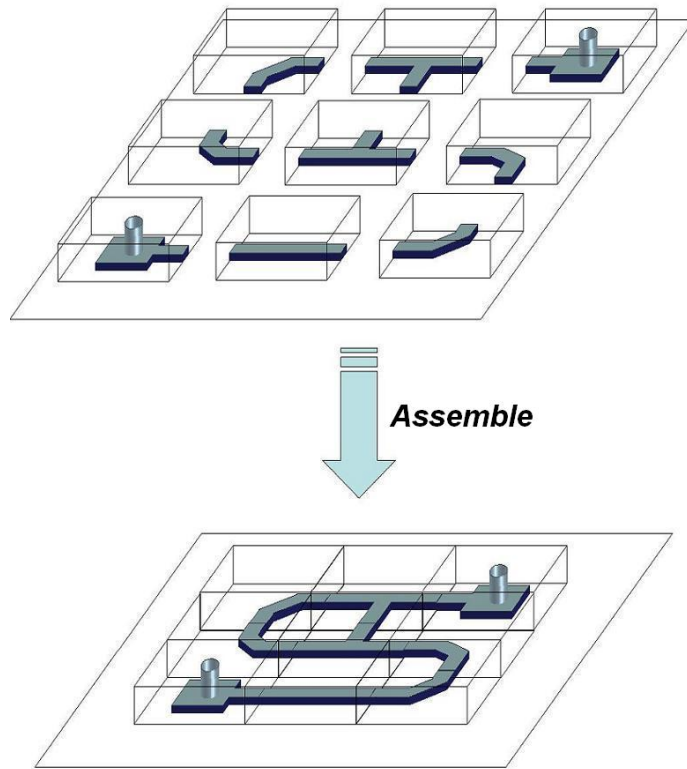


Figure 4-1. A schematic of the basic concept of the MAB approach. Users build a custom device by assembling MABs on a plain glass slide.

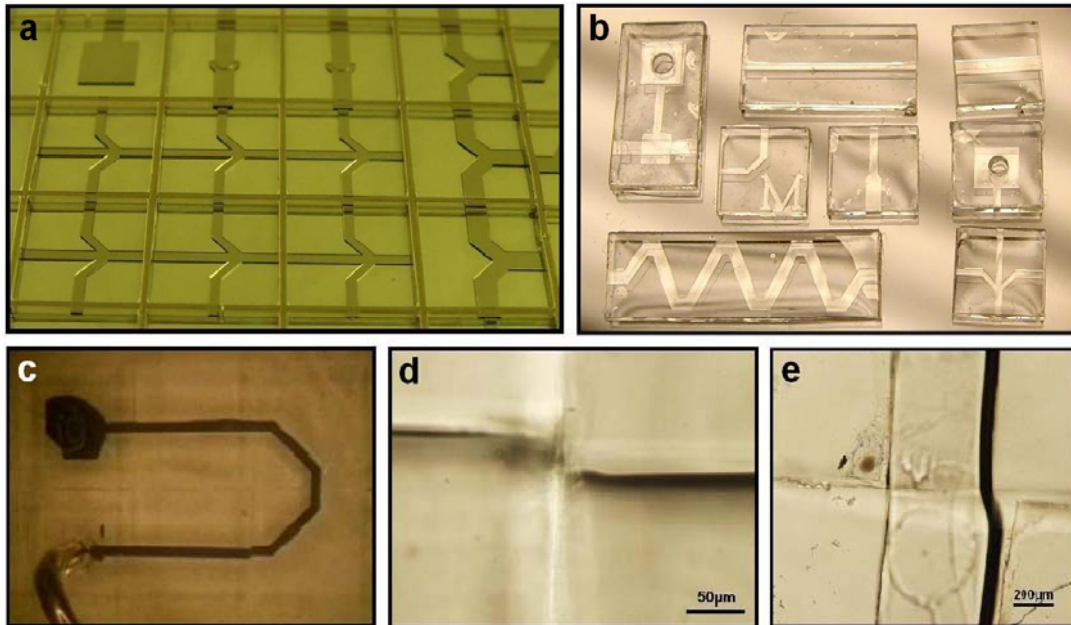


Figure 4-2. Microfluidic Assembly Blocks (a) A photo of the fabricated mold for various square blocks. (b) A photo of microfluidic assembly blocks before assembled. (c) Six square MABs were assembled on a PDMS-coated glass slide to build a basic U-turn channel, consisting of two inlet blocks, two straight blocks, and two 90° turn blocks. No post-treatment for bonding was applied. The sized of each block is 6mm x 6mm, and the channel width is 500 $\mu\text{m}$ . (d) MAB Alignments without any post-treatment for bonding, the inter-block gaps could be achieved under  $<5\mu\text{m}$ . (e) After the bonding with curing agent, the blocks were tightly sealed.



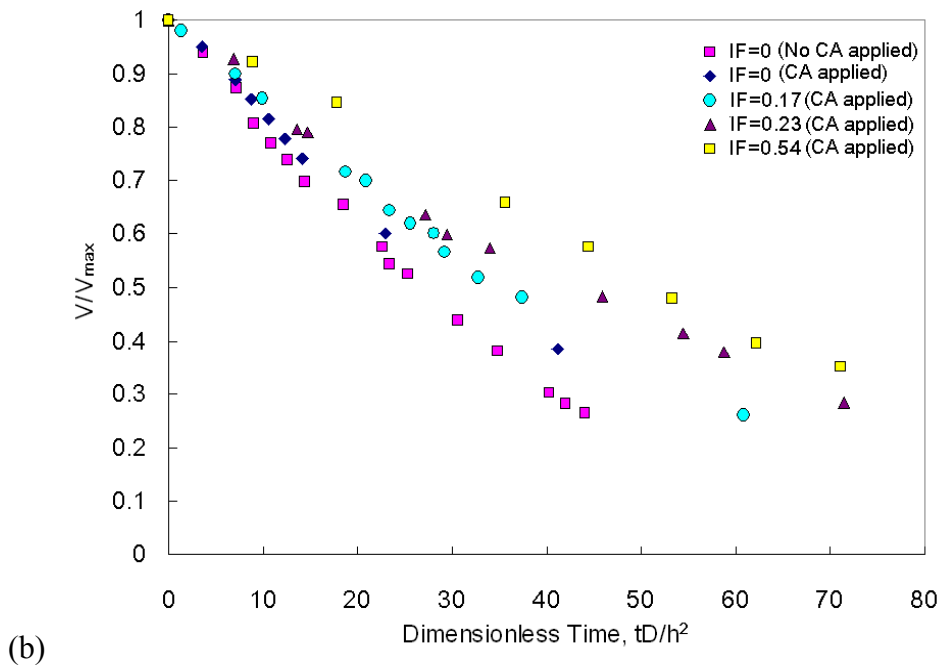
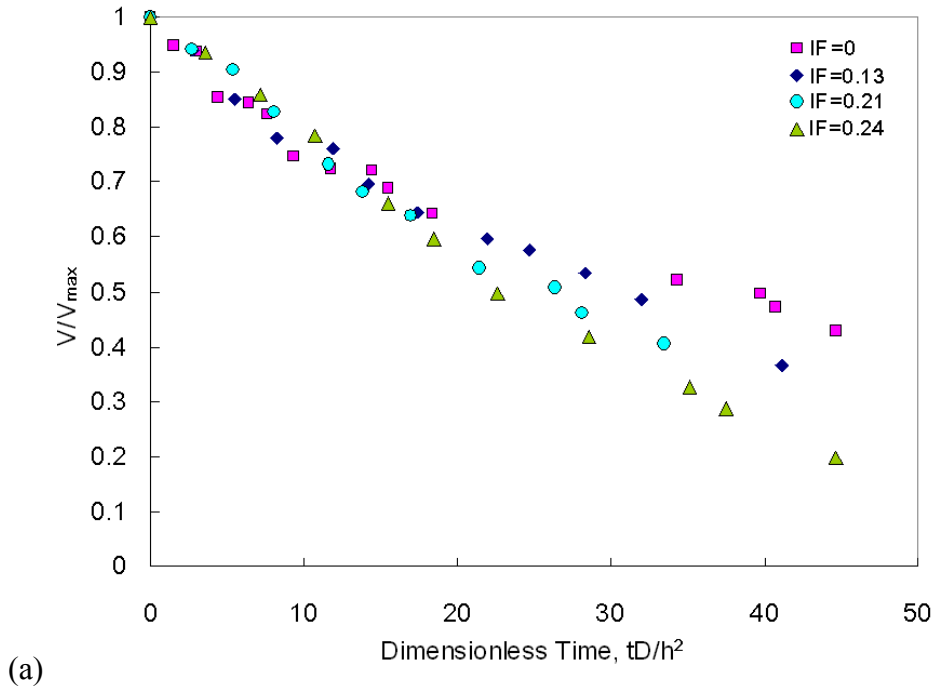


Figure 4-3. The effect of inter-block gaps on the evaporation rate. The device of IF=0 is a completely closed device while the devices of non-zero IFs have inter-block junctions. (a) No post-treatment for bonding has been applied. Open gaps expedite evaporation. (b) The devices have inter-block junctions filled with the curing agent except for the first device of IF=0. Gaps filled with the curing agent decrease evaporation rates.

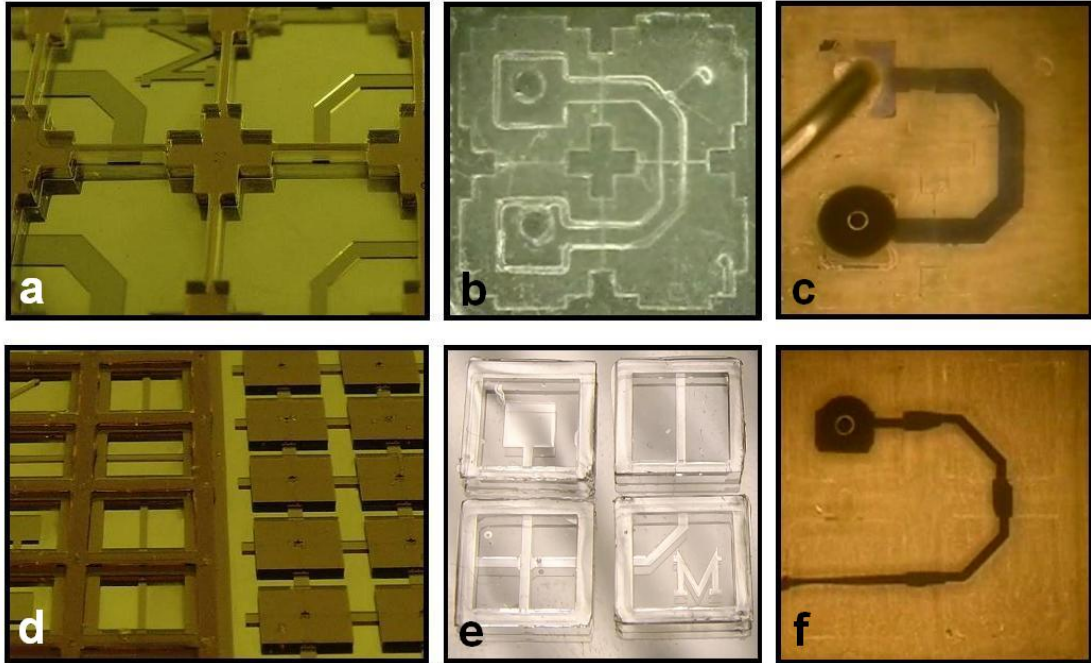


Figure 4-4. Photos of (a) the fabricated mold for the cross alignment key system, (b) the assembled device, and (c) a fluidic test. Photos of (d) the fabricated mold for the roofed blocks (left) and the channeled base (right), (e) roofed blocks. and (f) a fluidic test on an assembled device.

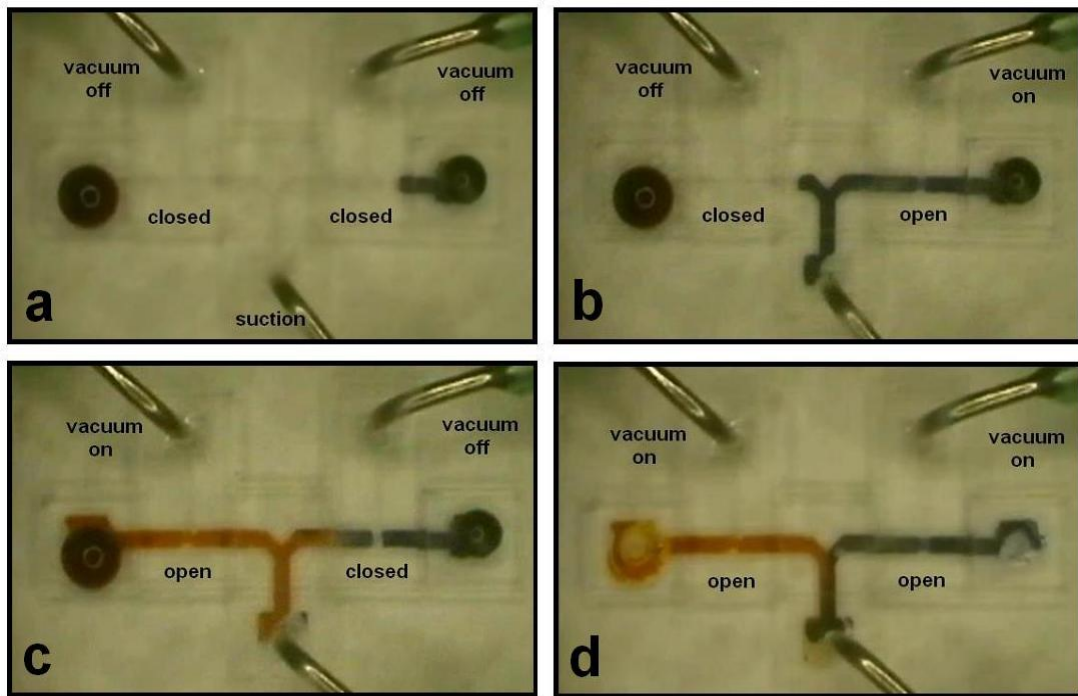


Figure 4-5. Demonstration of the valve module working in an assembled device. (a) A drop of an orange solution is placed at the left inlet while a blue drop at the right inlet. When both valves are closed, both the orange and blue drops will not move. (b) When the right valve is open in the presence of applied vacuum, the blue solution passes through the valve to the outlet where the suction exists. As the valve is closed, a portion of the fluid will stop and not be drawn further. (c) After the left valve opens, the orange solution is drawn to the outlet. (d) When both valves are open, both solutions are aspirated.

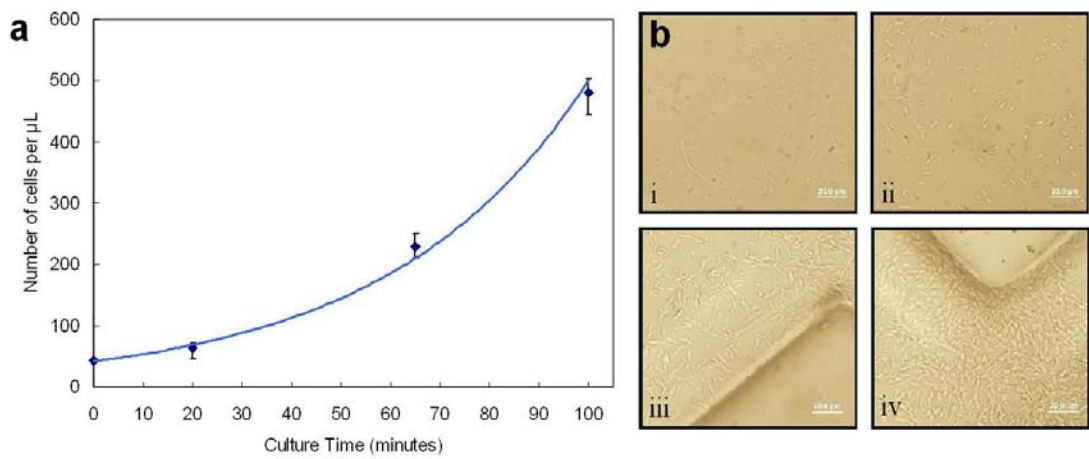


Figure 4-6. *E. Coli* cell culture in the MAB assembled device. (a) Plot of cell concentration versus culture time (b) Photos of the grown cells in the device at different culture times. (i) 0 min, (ii) 20 min, (iii) 65 min, and (iv) 100 min, respectively.

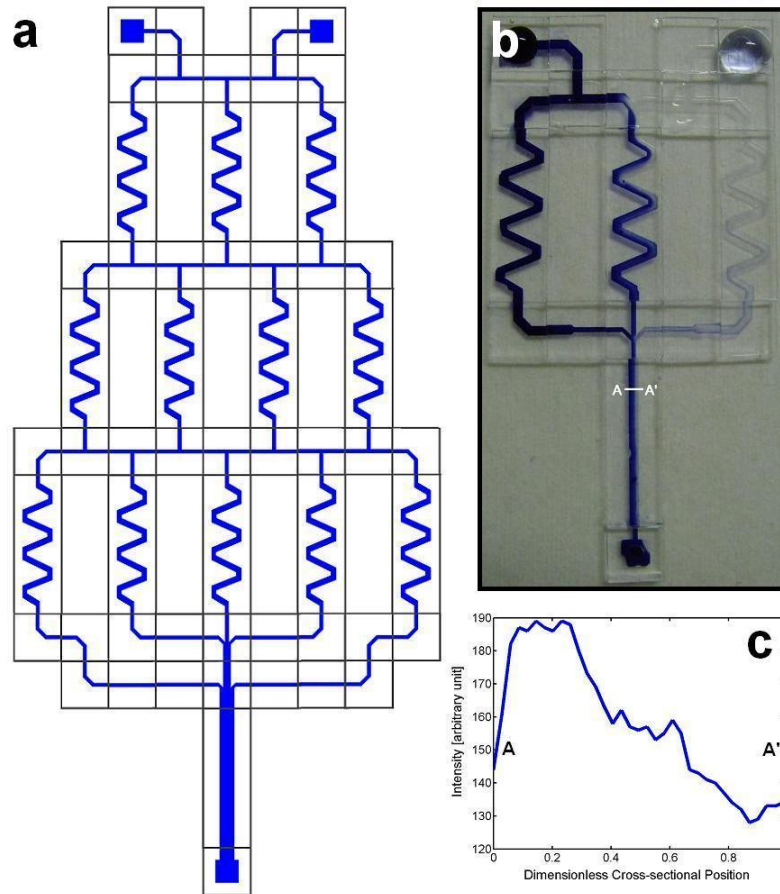


Figure 4-7. Exemplary systems for complex biochemical assays. (a) A conceptualization of a molecular gradients generator using the zigzag channel modules and other MABs that can generate five different concentration levels of the two-sample mixture. (b) Demonstration of a simpler system that mixes the blue dye and water into the outgoing stream with three different concentration levels. (c) The cross-sectional profile of blue dye concentrations at A-A' showing the concentration gradients.

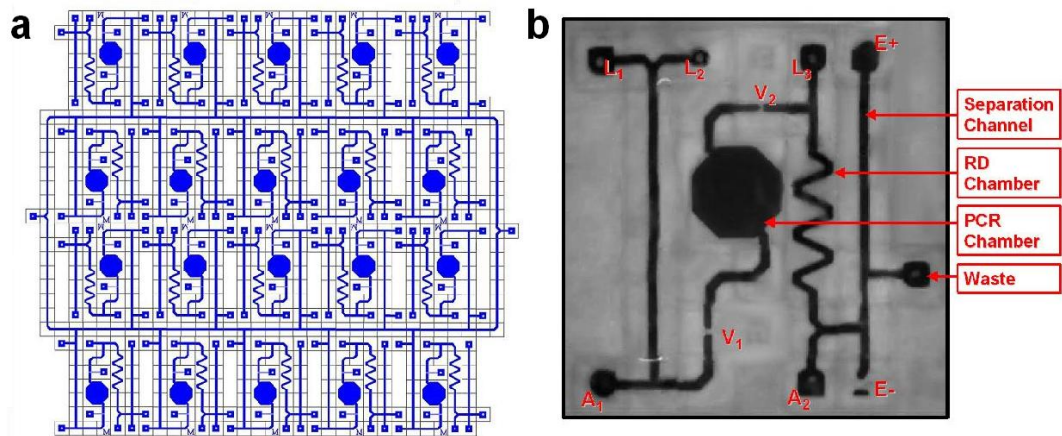


Figure 4-8. Large-scale Assembly (a) A conceptualization of a large-scale integration of a complex system that can perform twenty independent assays simultaneously from one sample. (b) Visual demonstration of an independent assay unit. Each unit device can perform reagent mixing, PCR, restriction digest reaction, and a separation. There are three liquid entries (“L1” for PCR reagents, “L2” for the sample, and “L3” for RD reagents), two pneumatic air controls (“A”), two valves (“V”), and two electrode positions (“E”).

## **Appendix**

Bonding Techniques

Block Shapes

Visualization of microfluidic laminar flows

Tables S1 to S2

Figs. S1 to S9

## **Bonding Techniques**

We investigated a number of bonding techniques (Table 4-S1), using adhesive substances (the PDMS mixture used to fabricate the blocks, the PDMS curing agent, and a UV-curable glue) to increase the block/block bonding. The adhesive not only flows into the nanometer gap between the blocks and the substrate but also fills the inter-block gaps (Figure 4-S4). For PDMS mixture filling, the device was moved to a flat surface and cured at 150°C for 15 min. The same curing process was applied for PDMS curing agent filling. For the UV-curable glue bonding, the device was transferred in the UV crosslinker immediately after the capillary action took place and cured for 10 minutes. Note that the bonding with curing agent is preferred since it is reversible, allowing for instant reuse of the MABs, and it does not require pre-mixing. Similarly, the blocks bonded with the UV-curable glue can be also recovered after immersed in water for hours. The adhesive agent cannot be loaded onto the device in excess since the adhesive will then flow in the main channels of the device, and, if large gaps exist between block, capillary action will not be able to fill them.

## **Block Shapes**

A different candidate for the unit block shape is a hexagon. This hexagon block system is preferred when the channel network of a desired device involves several oblique lines, as shown in Figure 4-S5a, rather than perpendicular lines only. In a hexagonal block, the channel can spread in six different directions. However, if the device contains a mostly perpendicular channel network, the hexagon system may not be suitable because features like 90° turns are difficult to realize in this format.

One drawback of the assembly methodology with square or hexagon blocks rather



comes from the lack of alignment keys. Slight deviations in just a few blocks may cause an overall alignment problem, especially for a large assembly task. One of the popular methods to overcome such a problem is constructing tabs that interlock on the sides of blocks. Two exemplary designs are illustrated in Figure 4-S5b-c. Blocks from both designs can be rotated by 90°, and the tabs and indentations reduce the possibility of misalignment. Moreover, the second design as seen in Figure 4-S5c has been developed to mimic the profile of jigsaw puzzle pieces. Although these modifications of block shape enable the users to assemble their device more easily, two technical challenges are imposed on the developers. First, a more careful removal of PDMS blocks from the SU-8 master mold is necessary. Due to the complex block shapes, such weak parts as narrow necks exist, increasing the possibility of damage to blocks. Second, non-square blocks naturally have more interfacial area than square ones, indicating that the side surfaces of blocks must be very clean and flat to ensure an appropriate fit. Various block shapes and their assembly characteristics are listed in Table 4-S2.

### **Visualization of microfluidic laminar flows**

We have assembled a zigzag channel network that can be used to visualize microfluidic laminar flow (Figure 4-S8). For the device, two inlet MABs were used in conjunction with a Y-channel block for merging two streams, a zigzag channel module, and an outlet block. The channel length embedded in the zigzag module corresponds to that of five consecutive straight channel square blocks. In micro-scale environments, fluid flows are mostly laminar since viscous forces overwhelm inertial forces. Such laminar flows can however become a major hurdle in micromixer application, since the mixing is mostly diffusive. Besides diffusion, chaotic advection can improve mixing

significantly. In general, chaotic advection occurs when a flow experiences special geometries in the mixing channel. To generate chaotic advection, we developed a module that contains a zigzag microchannel. Such zigzag channels produce recirculation around the turns and thus enhance advective mixing at high Reynolds numbers ( $>80$ ). For lower Reynolds numbers, the flow is laminar and the mixing process relies most on molecular diffusion at interfaces. The zigzag channel is still useful for laminar mixing, since the elongated channel length increases the interface area between two concurrent laminar streams. We measured the progress of diffusive mixing along the module by comparing the concentration distributions before the flow enters, in the middle of the zigzag channel, and after the flow exits the module. The estimated Reynolds number in repeated runs ranged from 1.1 to 4.7, which belonged to the laminar regime. Image analysis of the profiles in Figure 4-S8c showed the expected result that there was only slight diffusive mixing between streams.

Table 4-S1. Various bonding strategies for assembly of MABs

Bonding Methods	Bare Glass Substrate		PDMS coated Glass Substrate	
	Substrate-Block Bonding	Block-Block Bonding	Substrate-Block Bonding	Block-Block Bonding
Inherent Adhesion Only	Reversible Weak	Reversible Very Weak Gaps may exist	Reversible Weak	Reversible Very Weak Gaps may exist
Application of PDMS mixture (10:1)	Reversible Moderate	Irreversible Moderate Fill inter-block gaps	Irreversible Moderate	Irreversible Moderate Fill inter-block gaps
Application of PDMS Curing Agent	Reversible Weak	Reversible Moderate Fill inter-block gaps	Reversible Moderate	Reversible Moderate Fill inter-block gaps
Application of UV-curable Glue	Reversible Strong	Reversible Strong Fill inter-block gaps	Reversible Strong	Reversible Strong Fill inter-block gaps
Oxygen Plasma Treatment	Irreversible Very Strong	Very Weak May exhibit leaks	Irreversible Very Strong	Very Weak May exhibit leaks

Table 4-S2. Various block shapes and their assembly

	Plain		Tabbed		Pre-defined	
	Squares	Hexagons	Tabs and Indents	Jigsaw Profiles	Alignment keys	Channeled base
<b>Fabrication</b>						
Block removal from the mold	Easy	Easiest	Medium	Difficult (necks)	Medium	Medium (Roof)
Base structure	None	None	None	None	Cross posts	Channeled base
<b>Assembly</b>						
Block Alignment	Square Tile layout	Honeycomb layout	Non-square Tile layout	Jigsaw puzzle layout	Pre-defined polygonal slots	Pre-defined square slots
Interface	Short	Shortest	Medium	Long	Medium	Long
Sealing	Good	Good	Medium	Poor	Medium	Best

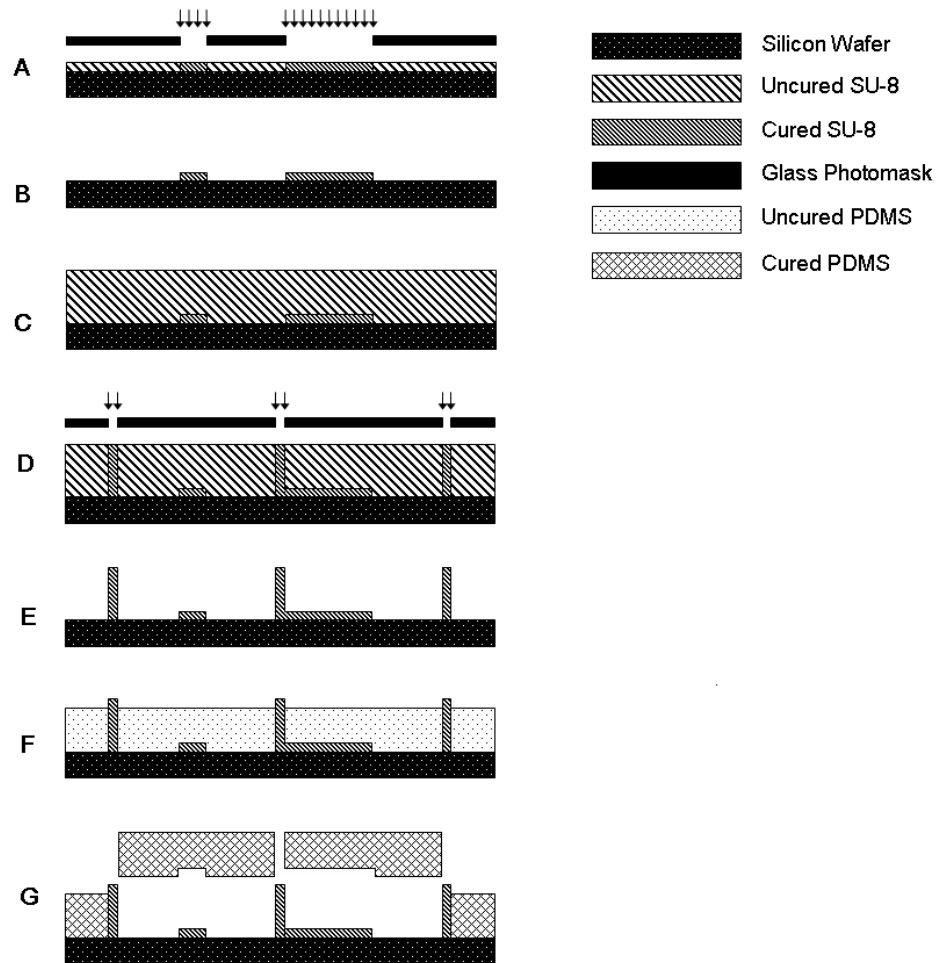


Figure 4-S1. The overall fabrication process for MAB. (a) The SU-8 resist is spun on a bare silicon wafer according to the patterns for fluidic channels and pre-baked on the hot plate for 5 min at the 65°C and for 20 min subsequently at the 95°C. The wafer is then exposed to 365 nm UV light. (b) After post-exposure baking (PEB) for 1 min at the 65°C and for 10 min at the 95°C, the wafer is immersed and developed in the SU-8 developer solution. (c) The SU-8 resist is spun and pre-baked repeatedly until the desired thickness is obtained. (d) The wafer then is carefully aligned to alignment cross marks and exposed. (e) After the PEB, the wafer is developed until the channel patterns surface. (f) A mixture of PDMS prepolymer and curing agent (9:1 w/w) is cast against the mold. Then, slightly tilt the mold and scratch the excessive PDMS solution off, using a razor blade. (g) Each cured PDMS block is carefully removed with a sharp aluminum needle.

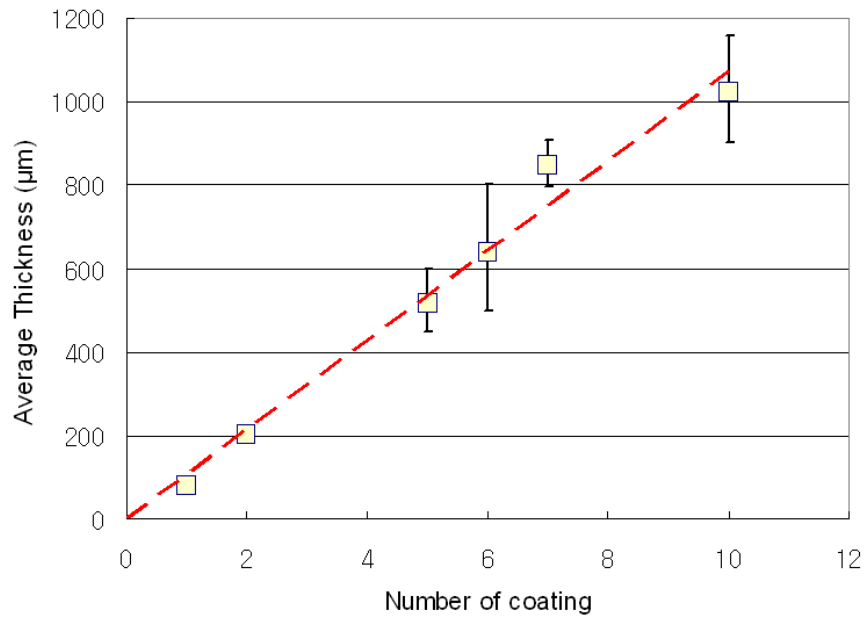


Figure 4-S2. Plot of the number of SU-8 2025 spin coating (500 rpm for 10 seconds and 1000 rpm for 30 seconds) versus the resulting average thickness of SU-8 multi-layer.

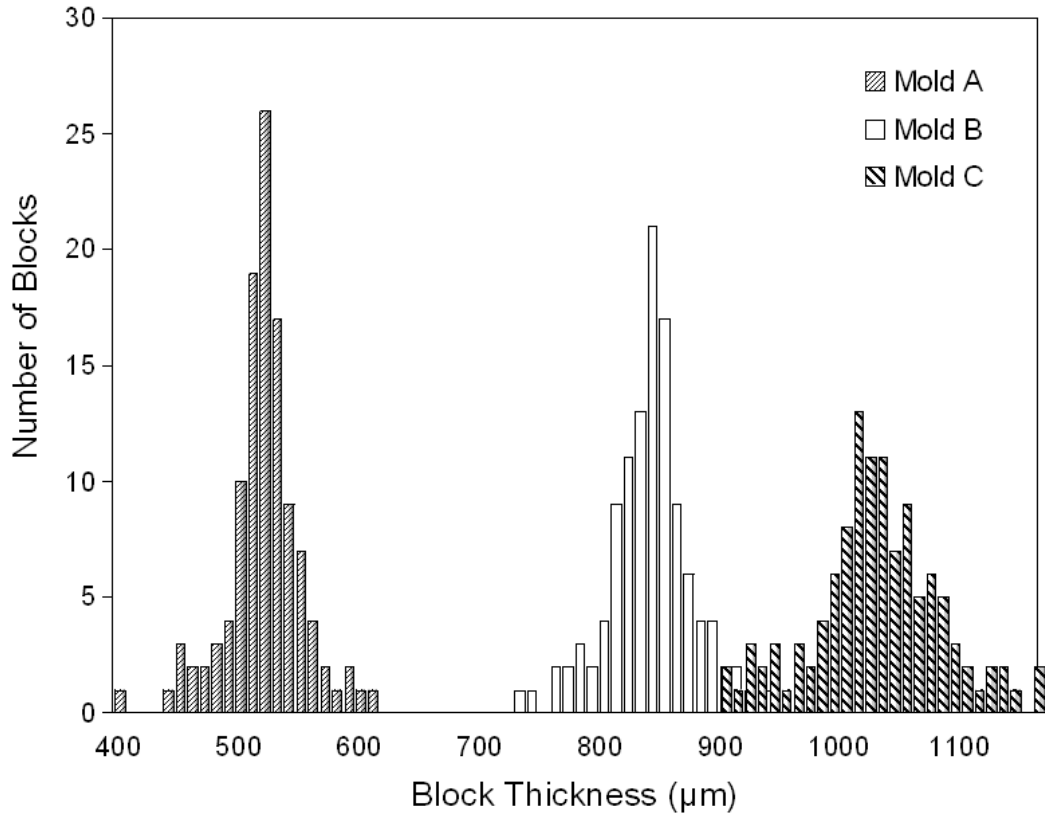


Figure 4-S3. The distributions of block thicknesses from different molds; the average thicknesses are 517  $\mu\text{m}$  from Mold A, 846  $\mu\text{m}$  from Mold B, and 1024  $\mu\text{m}$  from Mold C.

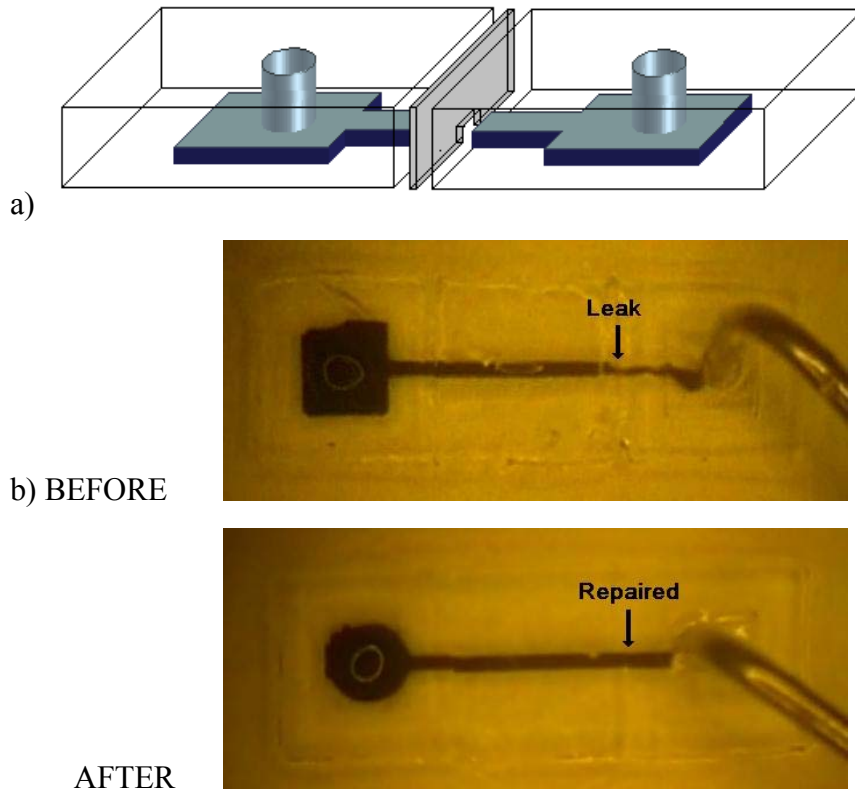


Figure 4-S4. Inter-block bonding by capillary effect. (a) The adhesive forms a thin layer between blocks to fill the inter-block gaps. (b) Post-treatment with curing agent application to remedy leaking problems. Before the treatment, the left junction was sealed well, but the right junction had a leak. Through the exposed gap, air was coming into the device. After the treatment, both junctions were completely sealed. The size of each block is 6mm x 6 mm and the channel width is 500 $\mu$ m.



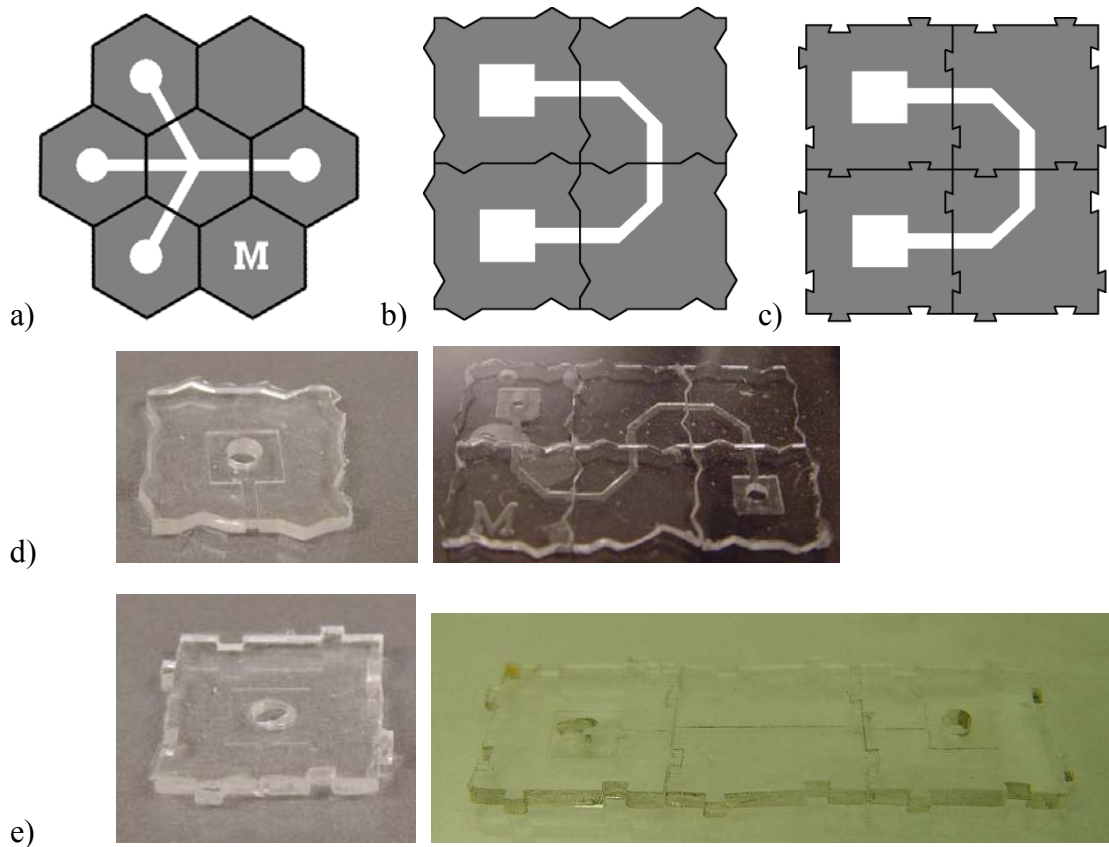


Figure 4-S5. Schematics of the devices assembled of (a) hexagon blocks, (b) tabbed blocks, and (c) jigsaw-style blocks. d) Photos of a tabbed block and an assembled device. e) Photos of a jigsaw-style block and an assembled device.

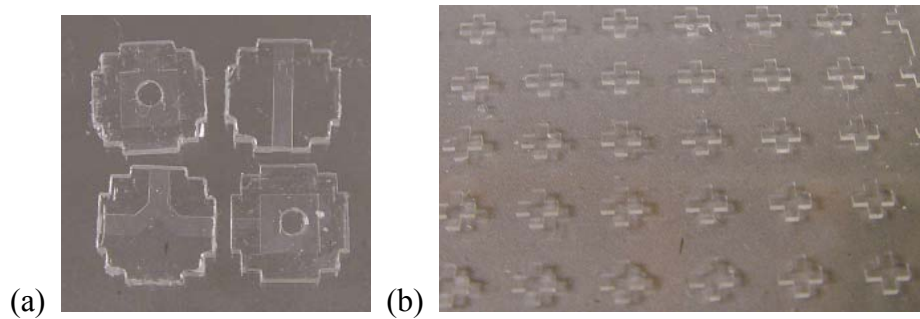
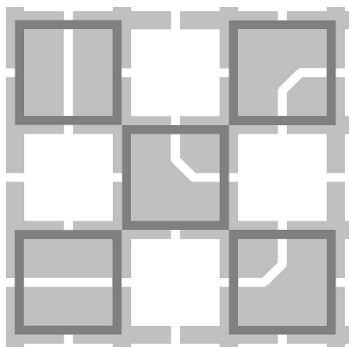


Figure 4-S6. The cross alignment block-and-base system. Photos of (a) the blocks and (b) the base with cross alignment posts.

(a)



(b)

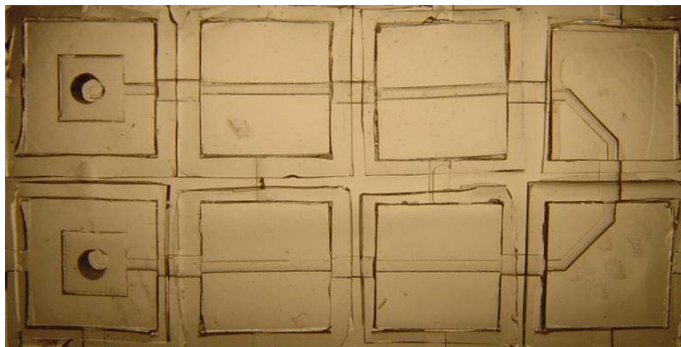


Figure 4-S7. The channeled base system. (a) Schematic of the concept. (b) Photo of an assembled device.

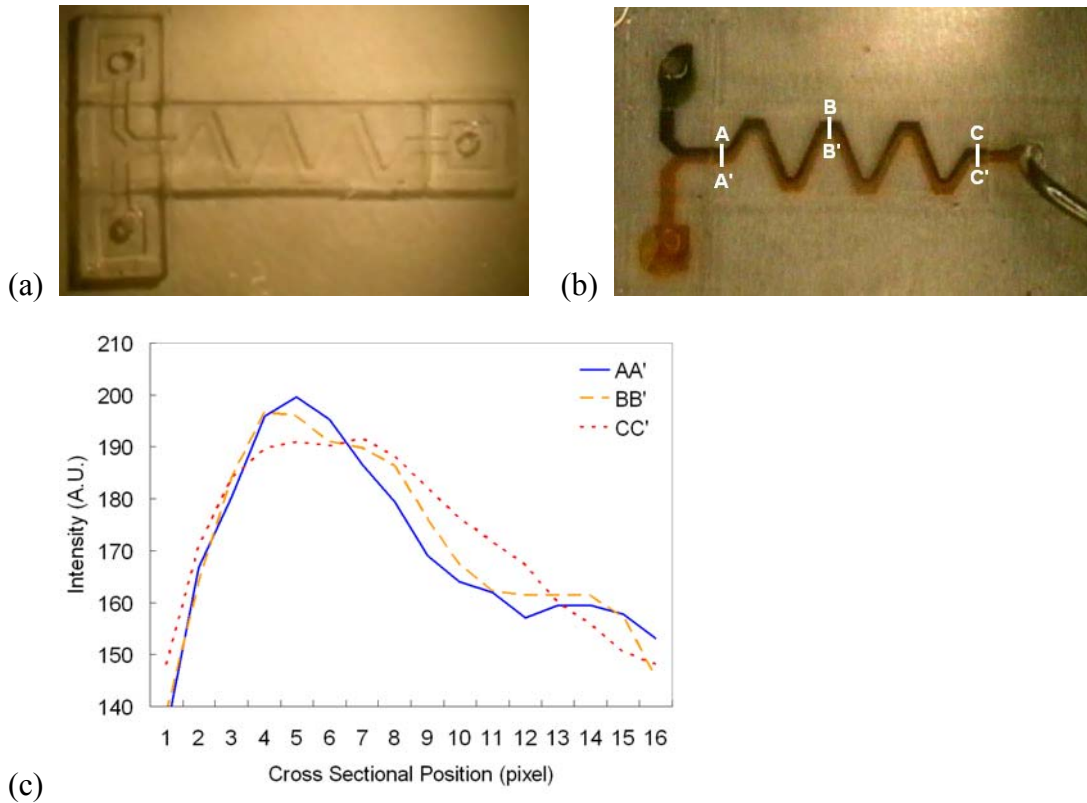


Figure 4-S8. Demonstration of diffusive mixing in laminar flows. (a) A photo of zigzag channel network device. Each square block is 6mmx6mm. The width of embedded channel is 1mm. (b) The blue and orange solutions merge and form two laminar flows ( $Re \sim 4.7$ ). (c) The progress of diffusive mixing. The zigzag channel shows limited diffusive mixing progress at this low Reynolds number.

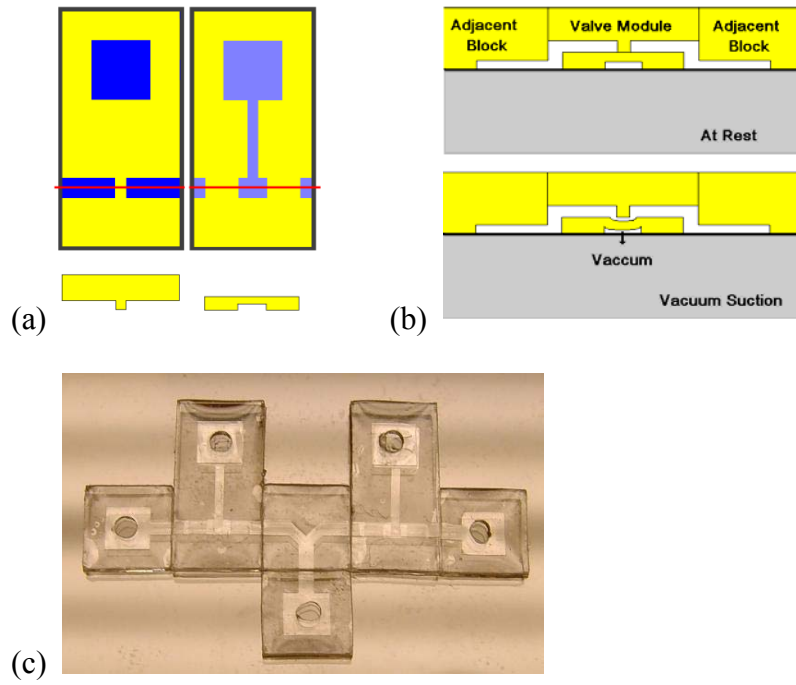


Figure 4-S9. (a) The design of the two-layer valve module. (b) A side view of the working valve module. (c) A device assembled with two valves.

## References

1. J. El-Ali, P. K. Sorger and K. F. Jensen, *Nature*, 2006, **442**, 403.
2. M. A. Burns, *Science*, 2002, **296**, 1818.
3. D. R. Meldrum and M. R. Holl, *Science*, 2002, **297**, 1197.
4. M. A. Burns, B. N. Johnson, S. N. Brahmamandra, K. Handique, J. R. Webster, M. Krishnan, T. S. Sammarco, P. M. Man, D. Jones, D. Heldsinger, C. H. Mastrangelo and D. T. Burke, *Science*, 1998, **282**, 484.
5. R. Pal, M. Yang, R. Lin, R., B. N. Johnson, N. Srivastava, S. Z. Razzacki, K. J. Chomistek, D. C. Heldsinger, R. M. Haque, V. M. Ugaz, P. K. Thwar, Z. Chen, K. Alfano, M. Yim, M. Krishnan, A. O. Fuller, R. G. Larson, D. T. Burke and M. A. Burns, *Lab Chip*, 2005, **5**, 1024.
6. G. M. Whitesides, *Nature*, 2006, **442**, 368.
7. D. C. Duffy, J. C. McDonald, O. J. A. Schueller and G. M. Whitesides, *Anal. Chem.*, 1998, **70**, 4974.
8. A. M. Tan, K. Rodgers, J. P. Murrhy, C. O'Mathuna and J. D. Glennon, *Lab Chip*, 2001, **1**, 7.
9. A. L. Liu, F. Y. He, K. Wang, T. Zhou, Y. Lu and X. H. Xia, *Lab Chip*, 2005, **5**, 974.
10. J. C. McDonald, M. L. Chabinyc, S. J. Metallo, J. R. Anderson, A. D. Stroock and G. M. Whitesides, *Anal. Chem.*, 2002, **74**, 1537.
11. A. Grimes, D. N. Breslauer, M. Long, J. Pegan, L. P. Lee and M. Khine, *Lab Chip*, 2008, **8**, 170.
12. K. A. Shaikh, K. S. Ryu, E. D. Goluch, J. M. Nam, J. W. Liu, S. Thaxton, T. N. Chiesl, A. E. Barron, Y. Lu, C. A. Mirkin and C. Liu, *Proc. Natl. Acad. Sci. U. S. A.*, 2005, **102**, 9745.
13. P. Grodzinski, J. Yang, R. H. Liu and M. D. Ward, *Biomed. Microdevices*, 2003, **5**, 303.
14. Y. N. Xia and G. M. Whitesides, *Annu. Rev. Mater. Sci.*, 1998, **28**, 153.
15. J. I. Ju, J. M. Ko, S. H. Kim, J. Y. Baek, H. C. Cha and S. H. Lee, *Bioprocess Biosyst. Eng.*, 2006, **29**, 163.
16. J. R. Anderson, D. T. Chiu, R. J. Jackman, O. Cherniavskaya, J. C. McDonald, H. K. Wu, S. H. Whitesides and G. M. Whitesides, *Anal. Chem.*, 2000, **72**, 3158.
17. W. J. Chang, D. Akin, M. Sedlak, M. R. Ladisch and R. Bashir, *Biomed. Microdevices*, 2003, **5**, 281.
18. N. Z. Li, C. H. Hsu and A. Folch, *Electrophoresis*, 2005, **26**, 3758.

19. B. H. Jo, L. M. Van Lerberghe, K. M. Motsegood and D. J. Beebe, *J. Microelectromech. Syst.*, 2000, **9**, 76.
20. M. Rhee and M. A. Burns, *Langmuir*, 2008, **24**, 590.

## **Chapter 5**

# **Digital Pneumatic Microprocessors for Microfluidic Large-Scale Integration**

### **5.1 Introduction**

Since the early 1990's, many innovative microfluidic lab-on-a-chip devices have been developed that analyze picoliters of fluid under controlled reaction conditions (1, 2). However, little of the anticipated impact of microfluidics has been realized possibly due to the gap between technology developers and technology users (3, 4) or to the complexity of the constructed devices. Many potential microfluidic applications often require the integration of a large number of valves, pumps, and other components, many of which need additional off-chip control equipment. Although recent technical advances in pneumatic microvalves (5) have enabled large-scale integration of microfluidic devices to perform hundreds of microfluidic operations in parallel by multiplexing control of embedded operational valves (5-8), the need for a large number of dedicated external control lines imposes practical limits on the portability and scalability of integrated microfluidic systems.

The complex valve control can be simplified by integrating microfluidic devices



using on-chip fluidic logic networks (9), significantly reducing the number of required off-chip controllers. In electronics, large circuits performing complex operations are built from various networks of logic gates. Although analogous macroscale fluidic logic gates were developed back in the 1960s (10, 11), the nonlinearity from turbulent flows is not applicable to microfluidic systems (12). Various microfluidic logic gates operated on Boolean rules have been proposed to direct internal flows in complex networks and perform simple on-chip calculations (13-17). Although conceptually powerful, these microfluidic logic gates rely on different input/output types and, therefore, the output cannot be used as an input to directly actuate subsequent logic gates. This non-cascadable nature inhibits further scaling and feedback routing for more complex circuits. A more recent system using transistor-like pneumatic valves to form on-chip pneumatic demultiplexer circuits have been presented (9, 18). These structures do perform digital operations but decreases in the signal strength can be observed during signal transportation and the calculations cannot be repeatedly performed without appropriate venting each time. Other approaches utilizing droplet-based input/output for logic gates (13, 14) exhibit excellent cascability but construction of control platforms from these systems is difficult since the trajectories or existences of droplets cannot be used for actuation of active control components. Most importantly, no parallel operations have been achieved from serial input signals, resulting in lack of programmability.

## **5.2 Concepts**

This chapter presents microfluidic digital pneumatic circuits that operate on

serially encoded command signals. Digital pneumatic components such as flip-flops, logic gates, and shift registers are integrated to form advanced microprocessors capable of performing complex parallel operations of numerous individually addressable valves while the number of control inputs is fixed at one. In comparison with their electronic counterparts, several straightforward analogies are available such as in resistance (ohmic/flow), current (electrons/fluid), and driving forces (voltage-ground/vacuum-atmosphere). For these pneumatic circuits, two distinct pressure levels are used for the digital information: atmospheric pressure (bit value = 0) and vacuum (bit value = 1) (Fig. 5-1A). The fundamental building unit in our system is the asymmetric microfluidic inverter or NOT gate (Fig. 5-1B) employing a two-layered PDMS microvalve that is normally closed with an atmospheric input signal but opens with a vacuum signal (6). This microfluidic inverter is “powered” by the vacuum source connected to one end and “grounded” through an open hole to atmosphere at the other end. When the two pressure sources are connected, pressure gradients will be generated in the channel due to the different pressure levels at two ends. The pressure drop is proportional to the flow resistance. Application of a vacuum input signal with sufficient strength causes the input microvalve to open, resulting in an increase in pressure in the chamber labeled “output” (Fig. 5-1C and D, left), thus closing the output valve. For an atmospheric input signal, the input valve is closed and the output chamber returns to a vacuum state (Fig. 5-1C and D, right).

The signal strength required to operate the input valve depends on valve geometry. The pneumatic valve in the inverter has a thin membrane shared by the upper flow channel and the lower valve-operating channel (Fig. 5-1E). The membrane may be pulled toward either the upper channel (closed) or the lower channel (open) depending on

the pressures in the two channels. Thus, the fraction of membrane area (shaded) that the upper flow channel covers is a nontrivial design parameter. Fig. 5-1F shows the output pressure variation of the inverter when opening and closing the input valve. Once the input signal strength is beyond the required level (threshold), the valve experiences almost instant state changes; there has been no meta-stable transitional state observed. Fig. 5-1G shows the threshold) as a function of the area fraction covered by the upper channel in the valve diaphragm membrane.

### **5.3 Materials and Methods**

The PDMS circuit devices were constructed using three separate layers. The first thin ( $\sim 300\mu\text{m}$ ) “control” layer is situated at the bottom, containing valve displacement chambers, valve diaphragms ( $\sim 100\mu\text{m}$  thick) above the chamber, channels delivering operand signals to the valves, and interlayer connecting holes. One obvious advantage from constructing the valves in the thin bottom layer is easier visualization of the valve state. Since the thin bottom layer collapses more due to its flexibility, the open valve exhibits stronger reflection of light and the valve collapse will be easily visualized. The second “flow” layer harbors the channel network for control with various flow resistances. Finally, the optional third “supply” layer is composed of a large vacuum reservoir to supply vacuum to multiple vacuum ports in the second layer simultaneously without an external manifold.

The devices were manufactured using the standard soft-lithographic technique (19). The SU-8 master molds were fabricated by spinning the SU-8 2025 (MicroChem)

resist on a bare silicon wafer and pre-baked on the hot plate for 5 min at the 65°C and for 20 min subsequently at the 95°C. Approximately 150 µm thick patterns could be obtained when the spin coating was done twice. After the exposure to 365 nm UV light, the coated wafer was post-exposure baked for 1 min at the 65°C and for 10 min subsequently at the 95°C. The successive development in SU-8 developer solution (MicroChem) resulted in the channel patterns with desired thickness. The thicknesses of channels and membranes were measured with a mechanical height gauge (Mitutoyo).

Although all devices presented here were made of PDMS, they can be fabricated in a wide variety of materials to suit specific needs, including silicon and glass, especially for the tasks involved with PDMS-incompatible solvents. The normally closed pneumatic valve can be also constructed with diaphragms of different elastomers (20), preferably exhibiting less air-permeability. In our systems, each component takes an old signal as an input and produces a new full strength signal to be transferred, which makes air leaking through the diaphragm membranes less important. However, such airtight diaphragms will allow for development of more diverse and powerful pneumatic components since there will be no unfavorable signal loss.

## **5.4 Results and Discussion**

### **Signal Transfer**

To build complex logic circuits, there should be no signal loss during transmission from one logic unit to the next so that cascades of logic gates are possible. In other words, it is necessary that the strength of input signals should be maintained at

any output ports so that the output signals can be used as inputs to operate other units. Unlike the previous design of similar microfluidic inverters (9), the inverters presented here are asymmetric with different flow resistances to vacuum and atmospheric sources. Computational fluid dynamic simulations (Fig. 5-1C) show that when the input valve is open, the main channel exhibits pressure gradients due to the pressure difference between the two ends. The channel connecting the vacuum source holds much more flow resistance (typically, an order of magnitude) than the channel open to atmosphere. This asymmetric nature enables the resulting output signals to hold more than 90% of the strength of the atmospheric pressure, which is sufficient to operate an input valve in the successive logic gate. Each logic gate is a closed system where its output signal is always boosted from its own vacuum or atmospheric source, thus eliminating the possibility of undesirable signal loss. Note that, with simple modification of the asymmetric inverter, the NOR gate (Fig. 5-2A) and the NAND gate (Fig. 5-2B) can be constructed. The NOR gate is operated by two parallel input valves such that, when either valve opens, air flows into the main channel and generates an atmospheric output signal. For the NAND gate, both of the two serial valves must open together to produce an atmospheric output.

### **Pneumatic Logic Gates**

With these cascadable universal gates (i.e., NAND and NOR) along with the NOT gate, any complex logic gate and circuit can be formed. For example, two regular inverters connected in series become a buffer element (Fig. 5-2C) that helps maintain or amplify signals during the long course of signal transfer. An XNOR gate can be constructed from four NOR gates (Fig. 5-2D), and an XOR gate can be built by adding an inverter to an XNOR gate (Fig. 5-2E). Other gates such as AND, OR, three input gates,

etc., can also be constructed (data not shown).

Such pneumatic logic gates comprise the building blocks for more advanced logic circuits. A pneumatic bistable flip-flop has been built by employing two regular inverters with each output fed backed to the other input (Fig. 5-3A). For the two input valves, only one valve can be open at a time. Once one valve is open, both valves maintain their states indefinitely, remaining ‘latched’ in the absence of external perturbation such as a strong opposite input signal to either feedback loop or a mechanically forced closure of an open valve. Due to the elasticity of PDMS, the open valve can be forcedly closed by softly pressing the top of the open valve. It is thus possible to manually operate the flip-flops to produce alternating pressure controls without any electrical power. Such bistable flip-flops can be an essential element of microfluidic memory devices, which memorize valve operational commands for current or later uses.

### **Latching Circuits**

Pneumatic circuit components that have such latching capability are indispensable for the development of a large scale integrated microfluidic system that can address hundreds of individual valves independently. A latching inverter or buffer can be constructed from a pneumatic bistable flip-flop (Fig. 5-3B). Besides its core flip-flop for signal maintenance, the latching circuit has a latchable input and two outputs (buffered and inverted). When the latch valve is open, the input is transferred to the flip-flop and the flip-flop changes its state accordingly within milliseconds. The feedback route at the input side has an increased flow resistance in order to avoid any possible compromise between the new input signal and the previous flip-flop feedback signal. When the latch

valve is closed, the circuit returns to a regular flip-flop and maintains the signals at both output ports. While previous pneumatic latching valves can retain the signal only for minutes (18), the output from our latching circuits persists without any loss of signal strength as long as the latching valve is closed. Fig. 5-3C shows a positive edge detector that produces short true signals whenever a pneumatic signal rises. The device makes use of the difference in signal transportation time between the two inputs of a NOR gate. One input signal directly from the first inverter reaches the NOR gate faster than the other input signal via the second inverter. Thus, for a short time ( $<200\text{ms}$ ), the NOR gate is fed with two false signals that produces a true signal at the output. As soon as the later input reaches the NOR gate, the output loses its temporary true signal. The toggle (Fig. 5-3D) uses such an edge detector in conjunction with a flip-flop to build a clock cycle doubler that takes clock pulses as the input and produces clock pulses with a doubled cycle.

### **Micropneumatic Shift Registers**

To process sequential data, shift registers are necessary to take the series of information contained in each sequential bit and decode them. Shift registers act as critical data processing units for serial data since a shift register can, essentially, parallelize serial information by spatially separating temporal signals. Fig. 3E illustrates the micropneumatic shift register (MSR) that consists of two consecutive latching inverters separated by clock valves. The pneumatic clock signal for these valves consists of pulses oscillating between two distinct pressure levels. The clock pulses can be generated within the pneumatic circuit by employing a regular inverter that uses its own output as its input, only with a long path of feedback containing resistance and capacity (Fig. 5-3F). Fluidic resistance ( $R$ ) and capacitance ( $C$ ) determines the clock frequency

that is proportional to the inverse of the time constant,  $\omega=RC$ .

## **Applications**

Pneumatic serial-to-parallel converters are built by connecting multiple shift registers together. With  $n$  shift registers concatenated in series,  $n+1$  bits of information out of the original serial input data are available at the parallel outputs after  $n$  clock cycles. Note that we can collect the  $(n+1)th$  bit from the original input data before it enters the first shift register. Fig. 5-4A shows the 4-bit digital pneumatic processor capable of converting serial input data operations to control four individual command valves independently. The processor is comprised of three shift registers to spatially separate the four serial bits of command information during three clock cycles; four latching buffers to memorize the operational instructions and maintain the output signals to actuate the final command valves; triggering valves that determines when the command information will be transferred to the latching buffers that function as instruction registers; and finally four target command valves that perform the desired operation. The four command valves are individually and independently accessible to control fluid channels. Since the commands are executed based on the signals in the latching buffers, they will persist continuously until the instruction registers get a new set of commands. In the exemplary application, four different color dyes are selectively controlled for mixing depending on their corresponding serial input commands. Such individually accessible command valves can be also used for multiplexing (Fig. 5-4B). Employing  $n$  shift registers in the serial-to-parallel converter,  $2^{(n+1)}$  flow channels can be individually addressed. Eight different flow channels are selectively accessed by the 3-bit multiplexer.



Adding combinatorial circuits, more complex computing capabilities can be realized in digital pneumatic processors. For instance, instead of using a separate trigger signal to initiate signal transfer from shift registers to instruction registers, we can program a command termination code in the original serial input data. The processor in Fig. 5-5A was devised to take one legitimate command bit every two clock cycles and recognize the termination code consisting of two consecutive true bits. To detect the termination code, a pneumatic AND gate (a NAND gate followed by an inverter) was used. An edge detector finds the true signal from the AND gate output and automatically produces a short triggering signal. Since one can continuously send commands to the serial input after each termination code, the device can work as a multipurpose programmable microfluidic platform. A pneumatic clock pulse generator can be also embedded to eliminate the need for external solenoid clocking (Fig. 5-5B). While the previous microprocessors ultimately control target command valves, pumping or routing is also achievable with such microprocessors (Fig. 5-6A), where eight final output signals are used to control membranous bypasses for sample positioning (21). Finally, Fig. 5-6B shows multiplexing by manually-operable flip-flops. This multiplexer operates without any electrical power and the status of flip-flops will continue as long as vacuum is appropriately connected to the device.

## 5.5 Conclusions

The miniaturization and on-chip integration of control elements in microfluidic systems has the potential to reduce the complexity of interconnections and auxiliary

equipment. Regardless of the number of final output targets to control, the proposed digital pneumatic microprocessors can operate with only one input line for serial data; clock pulses and a trigger signal can be generated using pneumatic logic circuits. Also, there is no theoretical limit to the number of target parallel outputs although physical limitations will certainly exist. The challenge is rather, as we noticed from the computer industry in 1960s, to devise a practical scaling-down method for very small pneumatic valves and corresponding inverters. By standard soft-lithography, we were able to construct a latching circuit at one fourth the size without any change in design; larger decreases in size are possible although optimized design will be necessary. Considering that a shift register with associated channel networks takes up 3-4 times more area than a latching circuit, it is plausible to build >50 shift registers in a 10 cm diameter wafer-size device. With only 15 shift registers, the device could produce 16 independently accessible signals that can control  $2^{16}=65,536$  individual flow channels within the multiplexing scheme. Also, our pneumatic microprocessors have operated at low clock speed (<0.5 Hz). In terms of computational power, such pneumatic microprocessors cannot compete with their electronic counterparts but they offer an additional control axis (i.e., mechanical vs. electrical) as well as the potential for increased speed.

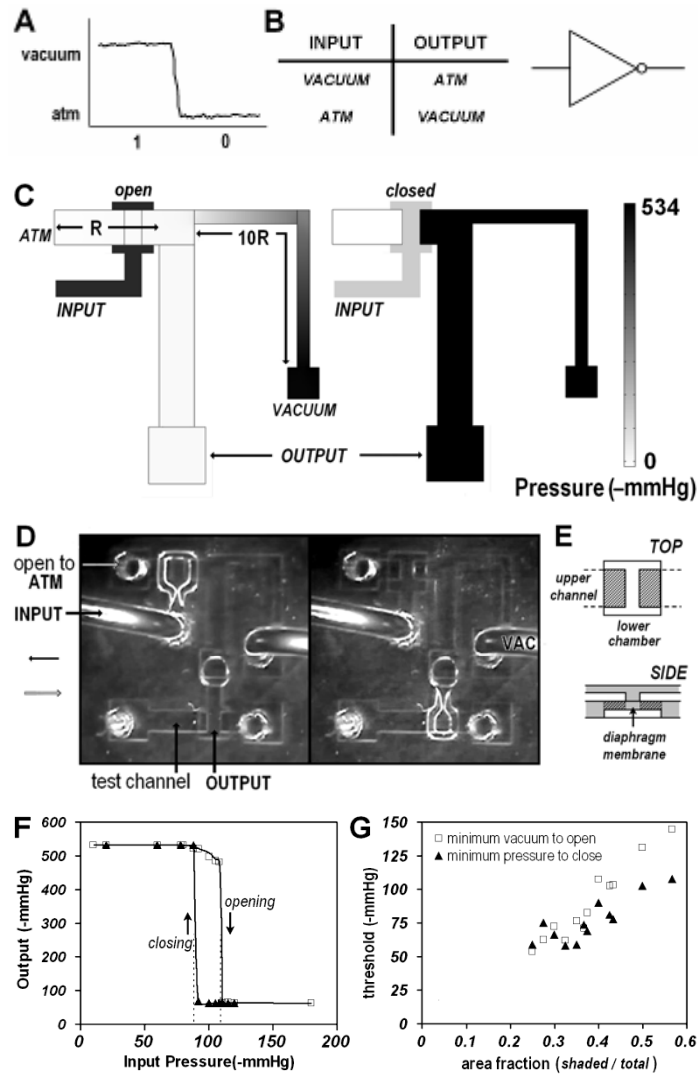


Fig. 5-1. Concepts and the fundamental pneumatic inverter. (A) Digitally conceptualized pressure levels. (B) The truth table of a pneumatic inverter and its corresponding electronic symbol. (C) Schematics and Computational pressure analysis in the inverter by simulations. Vacuum (left) and atmosphere (right) inputs are supplied. The channel connecting vacuum has  $\sim 10$  times more flow resistance ( $10R$ ) than that connecting the pressure source ( $R$ ). (D) The asymmetric microfluidic inverter operating on the inputs of vacuum (left) and atmosphere (right), respectively. The open valve exhibits stronger reflection of light due to the collapsed channel. (E) Top and side-views of the input valve. Shaded area represents the area fraction covered by the upper channel in the diaphragm membrane (F) Pressure variation during operation of the inverter. Threshold pressures to open/close the input valve are displayed in dotted lines (area fraction=0.4). (G) Plot of the threshold pressure levels as a function of the area fraction occupied by the upper flow channels in the valve diaphragm.

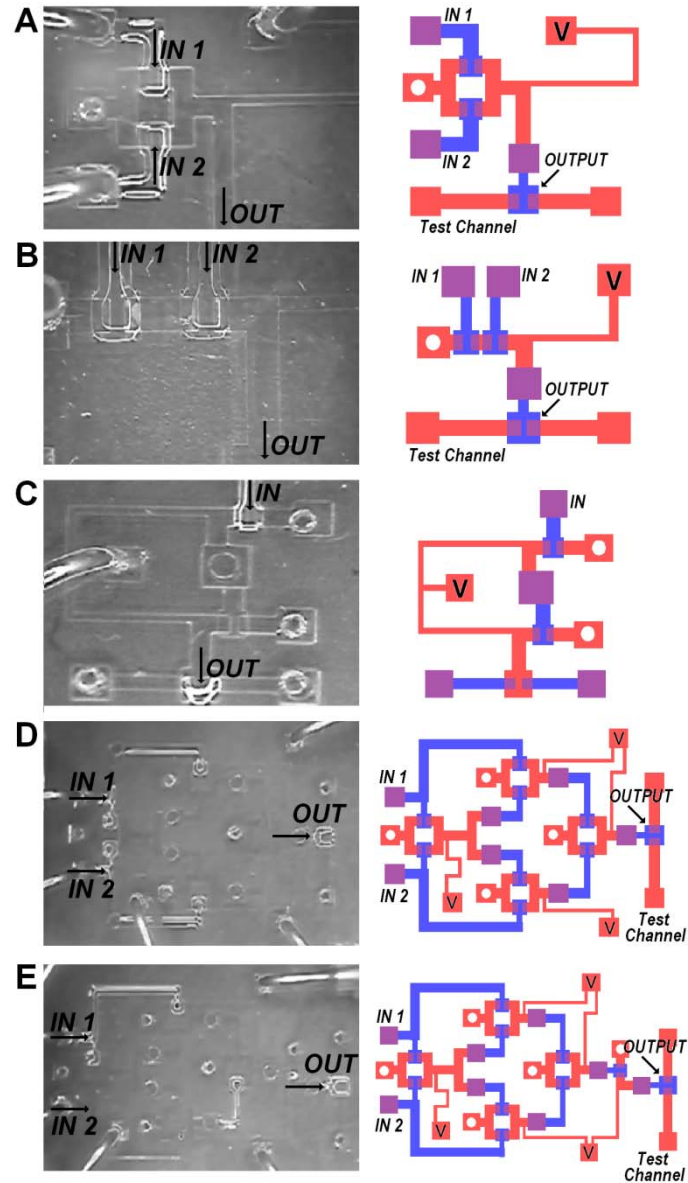


Fig. 5-2. Various pneumatic logic gates. In the schematics, white circles indicate holes open to atmosphere and 'V's represent connections to vacuum reservoir. Violate squares designate inter-layer connections between the valve and channel layers. (A) NOR gate at both inputs of 1, producing the output of 0. (B) NAND gate at both inputs of 1, producing the output of 0. (C) Buffer gate at the input of 1, producing the same output of 1. (D) XNOR gate at both inputs of 1, producing the output of 1. (E) XOR gate at the inputs of 1 and 0, producing the output of 1.

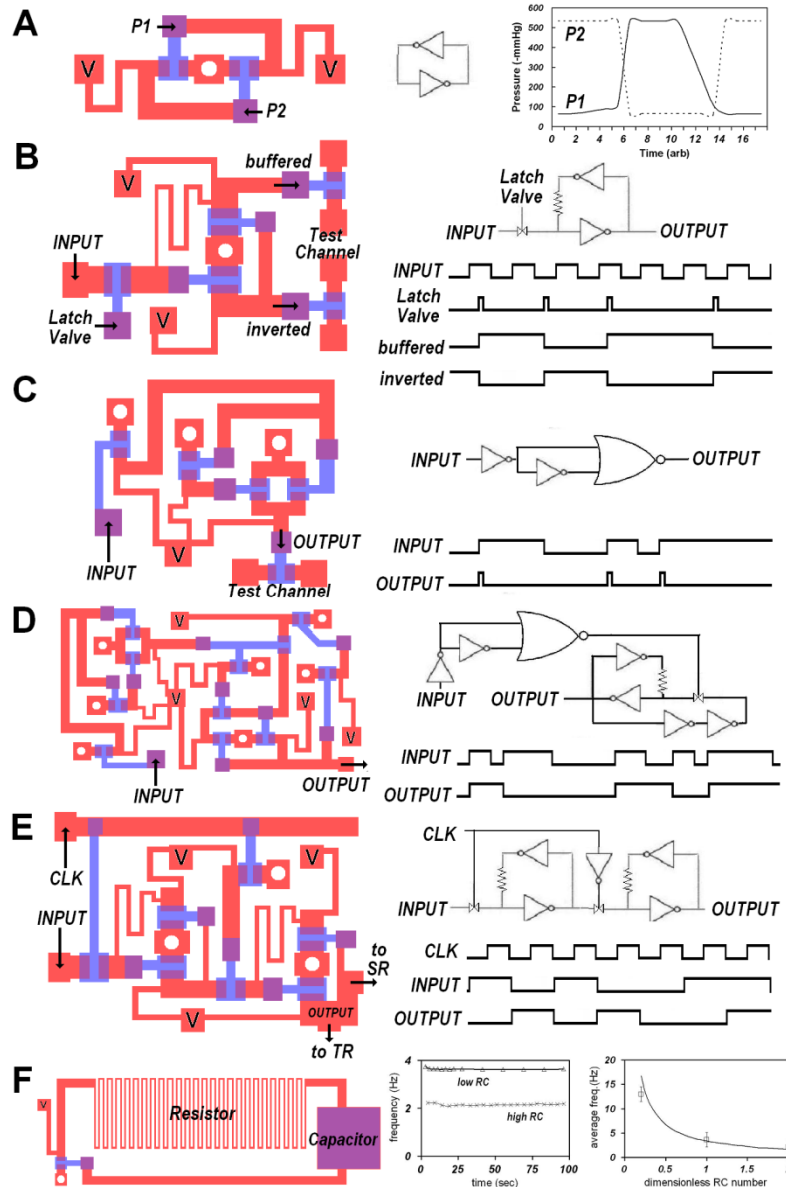


Fig. 5-3. Advanced pneumatic circuits. (A) Pneumatic bistable Flip-flop. The pressure levels of P1 and P2 are opposite to each other and change by external perturbations. The plot shows how P2 changes depending on the controlled P1. (B) Latching circuits. When the latch valve is open, the circuit accepts the input. When the valve is closed, it maintains two different outputs; buffered and inverted, respectively. (C) Positive edge detector. It detects positive rises of pneumatic signals and produce a short (<200ms) pulse at every rises. (D) Toggle. Every positive input toggles the sign of output. (E) Shift register. It takes a series of bits from the input and shifts the bits along one clock cycle. (F) Pneumatic Clock generator. The circuit produces oscillating pneumatic pulses. The clock frequency will be determined by the embedded resistor and capacitor. High resistance and capacitance yields pulses of low frequency.

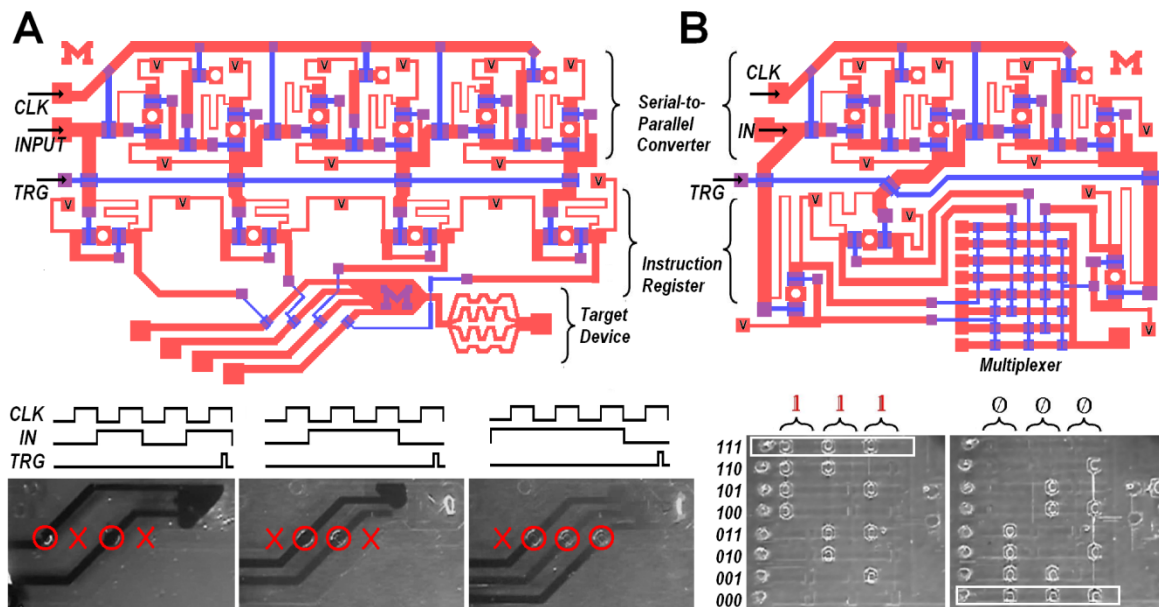


Fig. 5-4. Various digital pneumatic microprocessors. (A) The 4-bit processor takes serially encoded input along accompanying clock pulses, generating four independent parallel outputs to control the corresponding four command valves in the mixing device. (B) The 3-bit processor generates three independent outputs from serial input to address eight individual channels by multiplexing.

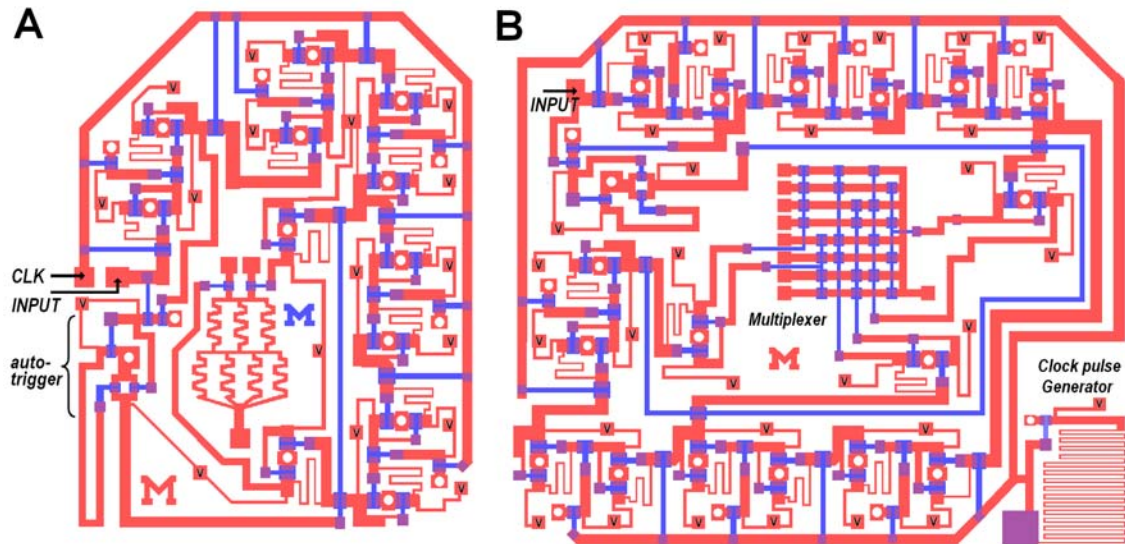


Fig. 5-5. Programmable digital pneumatic microprocessors (A) This programmable processor takes serially encoded input with the auto-triggering code embedded, and produces two independent parallel outputs to control the corresponding two command valves in the molecular gradient generating device. (B) Auto-clocking and auto-triggering 3-bit microprocessor. This processor runs from the encoded input signals based on the embedded clock pulses. Three parallel outputs allow for multiplexing eight individual channels.

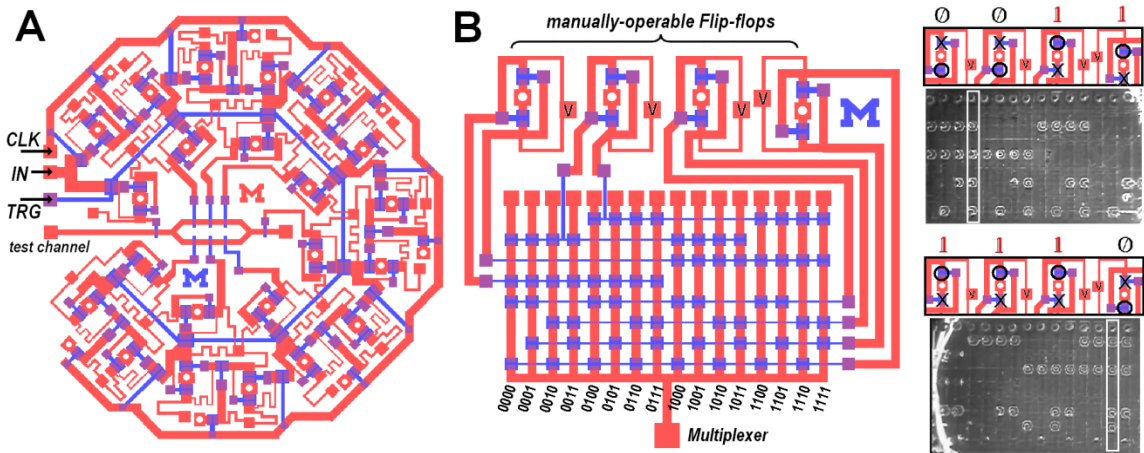


Fig. 5-6. Specialized microprocessors (A) The 8-bit microprocessor produces eight parallel outputs from a single serial input. The outputs act as membranous pumps to position, direct, and route fluid flows in the test channel. (B) Manually operable multiplexer. Four flip-flops are generating four manually controllable out



## **Appendix**

Logic Pumping and Routing

Portability

Table 5-S1. Truth Table for Pneumatic NOR Logic Gate

Table 5-S2. Truth Table for Pneumatic NAND Logic Gate

Table 5-S3. Truth Table for Pneumatic XNOR Logic Gate

Table 5-S4. Truth Table for Pneumatic XOR Logic Gate

### **Logic Pumping and Routing**

While the output from pneumatic circuits can be used either as the input to the successive circuits or used to control final target valves, Fig. 5-S1 shows another useful employment of the output as a pumping or routing element. The pumping chamber consists of the upper chamber for fluid flow and the lower chamber for vacuum supply that are separated by thin PDMS membrane. When vacuum output is supplied to the lower chamber, due to the air-permeability of the membrane, the pressure in the upper chamber can slowly decrease and the liquid sample is drawn to the chamber. Such air-bypass membranes can be constructed anywhere in the channel network to position a drop of liquid sample or to route fluid flow in the network.

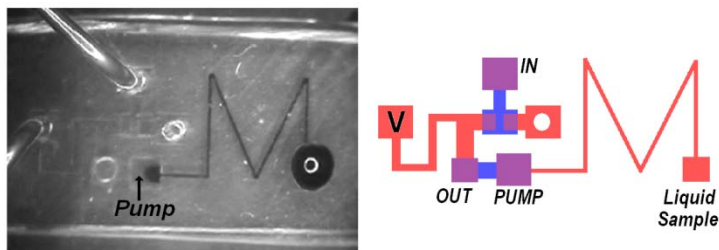


Fig. 5-S1. Membranous Pump operated based on the output from the inverter. At the output of 1, the blue dye is drawn to the pump while no pumping appears at the output of 0.

### **Portability**

The miniaturization and on-chip integration of control elements makes possible the development of truly portable lab-on-a-chip devices. Consequently, these structures can significantly reduce power consumption, cumbersome off-chip control and cost, making microfluidic analysis devices more accessible for various applications at remote sites. Since our pneumatic microprocessors basically run by driving force of pressure difference between vacuum and atmosphere, no electrical power will be required. If necessary, the serial data input and clock pulses are manually generated from a vacuum manifold with one end open to atmosphere. In addition, with appropriate tubing, strong enough vacuum can be always obtained anywhere one can turn on water in the aspirator.

Table 5-S1. Truth Table for Pneumatic NOR Logic Gate

INPUT 1	INPUT 2	OUTPUT
Atmosphere	Atmosphere	Vacuum
Atmosphere	Vacuum	Atmosphere
Vacuum	Atmosphere	Atmosphere
Vacuum	Vacuum	Atmosphere

Table 5-S2. Truth Table for Pneumatic NAND Logic Gate

INPUT 1	INPUT 2	OUTPUT
Atmosphere	Atmosphere	Vacuum
Atmosphere	Vacuum	Vacuum
Vacuum	Atmosphere	Vacuum
Vacuum	Vacuum	Atmosphere

Table 5-S3. Truth Table for Pneumatic XNOR Logic Gate

INPUT 1	INPUT 2	OUTPUT
Atmosphere	Atmosphere	Vacuum
Atmosphere	Vacuum	Atmosphere
Vacuum	Atmosphere	Atmosphere
Vacuum	Vacuum	Vacuum

Table 5-S4. Truth Table for Pneumatic XOR Logic Gate

INPUT 1	INPUT 2	OUTPUT
Atmosphere	Atmosphere	Atmosphere
Atmosphere	Vacuum	Vacuum
Vacuum	Atmosphere	Vacuum
Vacuum	Vacuum	Atmosphere

## References:

1. R. Pal, M. Yang, R. Lin, B. N. Johnson, N. Srivastava, S. Z. Razzacki, K. J. Chomistek, D. C. Heldsinger, R. M. Haque, V. M. Ugaz, P. K. Thwar, Z. Chen, K. Alfano, M. B. Yim, M. Krishnan, A. O. Fuller, R. G. Larson, D. T. Burke, M. A. Burns, *Lab chip* **5**, 1024 (2005).
2. M. A. Burns, B. N. Johnson, S. N. Brahma Sandra, K. Handique, J. R. Webster, M. Krishnan, T. S. Sammarco, F. P. Man, D. Jones, D. Heldsinger, V. Namasivayam, C. H. Mastrangelo, D. T. Burke, *Science* **282**, 484 (1998).
3. J. W. Hong, S. R. Quake, *Nat. Biotechnol.* **21**, 1179 (2003).
4. M. Rhee, M. A. Burns, *Lab Chip* **8**, 1365 (2008).
5. M. A. Unger, H. -P. Chou, T. Thorsen, A. Scherer, S. R. Quake, *Science* **288**, 113 (2000).
6. E. T. Lagally, J. R. Scherer, R. G. Blazej, N. M. Toriello, B. A. Diep, M. Ramchandani, G. F. Sensabaugh, L. W. Riley, R. A. Mathies, *Anal. Chem.* **76**, 3162 (2004).
7. T. Thorsen, S. J. Maerkl, S. R. Quake, *Science* **298**, 580 (2002).
8. W. H. Grover, A. M. Skelley, C. N. Liu, E. T. Lagally, R. A. Mathies, *Sens. Actuators B, Chem.* **89**, 315 (2003).
9. W. H. Grover, R. A. Mathies, *J. Micromech. Microeng.* **16**, 1378 (2007).
10. C. A. Belsterling, *Fluidic Systems Design*. Wiley-Interscience, New York (1971)
11. K. Foster and G. A. Parker, *Fluidics: Components and Circuits*, Wiley-Interscience, New York (1970)
12. A. Groisman, M. Enzelberger, S. R. Quake. *Science* **300**, 955 (2003).
13. L. F. Cheow, L. Yobas, D. -L. Kwong, *Appl. Phys. Lett.* **90**, 054107 (2007).
14. M. Prakash, N. Gershenfeld, *Science* **315**, 832 (2007).
15. T. Vestad, D. W. M. Marr, T. Munakata, *Appl. Phys. Lett.* **84**, 5074 (2004).
16. M. W. Toepke, V. V. Abhyankar, D. J. Beebe, *Lab Chip* **7**, 1449 (2007).
17. W. Zhan and R. M. Crooks, *J. Am. Chem. Soc.* **125**, 9934 (2003).
18. W. H. Grover, R. H. C. Ivester, E. C. Jensen, R. A. Mathies, *Lab Chip* **6**, 623 (2006).
19. Y. N. Xia and G. M. Whitesides, *Annu. Rev. Mater. Sci.* **28**, 153 (1998).
20. P. A. Willis, B. D. Hunt, V. E. White, M. C. Lee, M. Ikeda, S. Bae, M. J. Pelletier, F. J. Grunthaler, *Lab Chip* **7**, 1469 (2007).
21. M. Rhee, M. A. Burns, *Sensors and Transducers: Special Issue on Microsystems: Technology and Applications* **3**, 37 (2008).

## **Chapter 6**

### **Conclusions**

The main goals of this dissertation were developing unique and novel advanced components and platforms for widespread use of microfluidic lab-on-a-chip devices. As addressed in the previous chapters, the impact of the microfluidics technology has been anticipated over two decades. Nonetheless, the field is arguably not where it was envisioned at the beginning. To make microfluidics evolve to a real scientific revolution, two different solutions are addressable. One is to discover and realize high impact applications in microfluidic environments and the other is seeking more user-friendly methodologies for a widespread routine use of microfluidic devices. Likewise, microfluidic devices typically require a roomful of external control and monitoring equipment. Potential users in the life sciences are usually not trained for fluid manipulations in channels and physical measurements. The need for expensive off-chip controllers is thus another barrier for potential non-expert users.

Throughout this dissertation, practical and effective solutions were sought. In Chapter 2, discrete droplet mixing in microchannels was thoroughly investigated to attain a better understanding of microfluidics fundamentals. Three different mixing regimes (diffusion-dominated, dispersion-dominated, and convection-dominated) were discovered for the first time. By mathematical modeling, simulations, and experimental verifications,

precise prediction of discrete drop mixing was possible for lab-on-a-chip systems. In the following chapter 3, unique bypass valve components was investigated to facilitate drop mixing in lab-on-a-chip systems. In lab-on-a-chip systems, merging two drops separated by trapped air is a challenging task. The membranous air bypass valve structures were constructed in either 2D or 3D. Using the MBVs, the trapped air between the discrete drops was successfully removed and the fused drop was set to move at a desirable velocity to achieve effective mixing. Such membrane valves were also developed to act as fluidic diodes for uses to control various microfluidic directional flows. This unique functionality enabled various flow network designs including droplet routing and positioning.

In Chapter 4, a direct solution to bridge the disconnect between developers and users was introduced with a user-friendly device fabrication methodology. This unique assembly methodology was proposed with microfluidic assembly blocks and the MAB system provided a simple way for non-fluidic researchers to build custom, complex microfluidic devices. The developers of MAB can manufacture a standard set of MABs in large volume that can be supplied to frequent users so that the blocks can be assembled into various custom devices. The MAB allowed for full flexibility in planar configuration. The exemplary assembled devices demonstrated that the technology can be able to be used in a wide variety of applications. Consequently, the proposed MAB methodology would provide a powerful assembly strategy to meet the recent needs since such devices with a simple configuration can be constructed without any complicated fabrication procedures in very low cost.

In the last chapter 5, an ultimate solution for the intricate control systems of current microfluidic devices was demonstrated. The digital pneumatic microprocessors

were capable of various computational tasks with microfluids. Equipped with computational capability, the processors accepted serially encoded commands as inputs and produce parallel outputs to address multiple valves, pumps, channels, or chambers, independently. The miniaturization and on-chip integration of control elements in microfluidic systems significantly reduced the complexity of interconnections and auxiliary equipment. Consequently, these structures can significantly reduce power consumption, cumbersome off-ship control and cost, making microfluidic analysis devices more accessible for various applications, even at remote sites.



## **Appendices**

## **Appendix A**

### **Nanopore Sequencing Technology: Research Trends and Applications**

#### **A.1 Introduction**

DNA sequencing techniques have benefited a large number of scientific fields including genetics, computational biology, biomedical science, clinical diagnostics, molecular biology, anthropology, archaeology and forensic sciences [1]. Despite the large amount of information that has become available from the Sanger sequencing method [2] employed in the Human Genome Project (HGP), it is clear that the future demand for sequence information will keep increasing. Although the Sanger method has become more cost-effective through the parallelization, automation and refinement of established methods, the time and cost still remains a barrier to growing sequencing needs and has fueled the demand for faster and cheaper sequencing technology [3, 4].

Several academic and commercial efforts are developing new sequencing technologies that aim to reduce the cost of DNA sequencing by several orders of magnitude [5]. Such new technologies include the Pyrosequencing based on the detection of the pyrophosphate (PPi) released during the DNA polymerization reaction [6, 7, 8], and hybridization sequencing from microfabricated arrays of immobilized

oligonucleotide probes [9, 10]. Furthermore, the need for the tedious preparation work would be obviated through direct analysis of single DNA molecules. Many approaches to single-molecule analysis have been explored, including flow cytometry [11], optical mapping [12], exonuclease digestion [13, 14] and capillary electrophoresis (CE) separation with single-molecule detection [15]. Nevertheless, none of these single-molecule methods to date has been capable of sequencing significant numbers of nucleotides on single DNA molecules [4].

More recently, nanometer-scale pores have been investigated for single-molecule sequencing and analysis [16]. The concept of using small pores to analyze biological particles was inspired by the working principle of a Coulter counter [17], which is used to count particles ranging from sub-micron to millimeters: Particles suspended in an electrolyte solution are drawn through a small channel, separating two reservoirs. When a particle enters the channel, it increases the electrical impedance of the channel. By applying a voltage over the channel, the passing particles are detected as current drops. Microsecond-time scale characterization of nucleic acids is possible through such measurements without the need for complicated preparation such as amplification, chemical modification, or probe/intercalator binding [18].

As of today, there are two general classes of methodology to prepare nanometer-scale pores. The first attempts to produce nanopores were made with alpha-hemolysin, a transmembrane protein, inserted in a lipid bilayer [16, 19]. Beyond alpha-hemolysin, the use of other membrane-bound proteins has been also investigated in order to seek for various size organic pores that might exhibit even better applicability [20-23]. Although most of the experimental work in nanopore-based nucleic acid analysis is based on alpha-hemolysin, these protein pores in lipid bilayers have limitations in size, variation and

stability [24]. To overcome these difficulties, there have been several reports that various synthetic nanopores have been fabricated and used for basic DNA analysis using various means [25-29]. Successes in fabrication of such synthetic nanopores also shed light on the use of fully integrated microfabricated systems including microfluidics, analysis, and electrical detection for nanopore sequencing [30]. Such miniaturization through microfabricated systems will further improve the cost effectiveness of sequencing devices [31].

It is noteworthy that this chapter would not cover the field comprehensively and thus did not treat the advances in nanopore preparation such as synthetic nanopore fabrications. This chapter rather will present current nanopore technologies, focusing on recent developments of nanopore applications.

## **A.2 Molecular Discrimination using Nanopores**

### **Discrimination between ssDNA and dsDNA**

Kasianowicz et al. [16] first reported that a large number of transient ionic current blockades occurred in nanopores when single-stranded nucleic acid homopolymers were present, indicating that individual molecules were translocating through the small alpha-hemolysin pore and blocking ionic current produced by electrical field. It has been long known that the inherent structure of alpha-hemolysin nanopores is ideal for discriminating 150-nt single-stranded DNA from 100-bp double-stranded DNA because of the pore size [16, 32]. The confirmation from quantitative PCR revealed that only ssDNA were translocated through the alpha-hemolysin pore [4], and that the resulting ionic current blockades could be used to garner information about the molecules.

Their report verifies that nanopores can be used for discrimination of DNA molecules by their size, when the size of pores has been carefully chosen.

More recently, Heng et al. demonstrated that synthetic silicon nitride nanopores could be used as well to selectively isolate ssDNA from dsDNA [26]. Implementing gel electrophoresis verification, they determined that dsDNA cannot translocate through the 1 nm diameter pore. The distribution of transient durations from 50-bp dsDNA was distinctly different from that found when 50-mer ssDNA interacts with the same pore even though the physical length of the strands is comparable (about 17 nm). The frequency of long duration events observed for dsDNA was significantly low which indicates that most of the events were indeed unsuccessful translocation attempts.

### **Discrimination among homopolymeric RNA/DNA molecules**

In order to investigate the possibility that a nanopore can be used to discriminate different homopolymeric DNA or RNA molecules, a single-channel recording of the translocation time and blockade current drop during translocation of individual polynucleotides has been performed [19, 33]. This recording yielded a unique pattern of events for each of the several polymers tested. Akesson et al. compared the patterns of current blockade events in an alpha-hemolysin nanopore among homopolymers of polycytidylic acid (poly C), polyadenylic acid (poly A), and polyuridylic acid (poly U) with the same length [19]. These RNA molecules were initially chosen because they have a minimal tendency to form secondary structures that might block the pore instead of translocating. The blockade patterns of the different molecules could be statistically distinguished from one another by current blockade amplitude and translocation duration.

In a successive study, Meller et al. extended the previous observations to ssDNA

molecules [34]. Patterns for a given DNA molecule were uniquely characterized using three statistical parameters representing the most probable translocation current, the most probable translocation duration, and the characteristic dispersion of values for individual translocation durations. Because each type of polynucleotide produces specific values of the three parameters, different types of polynucleotides in a mixed sample could be discriminated statistically. Starting with the comparison between poly(dC)<sub>100</sub> and poly(dA)<sub>100</sub>, they investigated and differentiated several DNA molecules of different compositions as shown in Table A-1. Meller et al. also examined the temperature dependence of translocation events and found that translocation duration scales as  $\sim T^{-2}$ . This strong temperature dependence opened the possibility of controlling the translocation speed and enhancing the differences among various types of polymers. Such data derived from the pattern of events demonstrated that in several cases a nanopore can distinguish between polynucleotides of similar length and composition that differ only in sequence. Additionally, the average repetition rate of the polymer entering the pore is directly proportional to the concentration of the polymer in the bulk solution [35]. It is thus suggested that direct counting of translocation events would allow analyte quantitation.

### **Assessment of nucleic acid preparation**

Traditional techniques for assessment of DNA or RNA sample purity and chemical integrity such as electrophoresis, chromatography, and mass spectrometry have sensitivity limitations in the relative size and quantity of contaminating nucleic acids. In order to overcome such limitations, Wang et al. showed that the alpha-hemolysin nanopore could evaluate both short and long polynucleotides in a mixture of sample [36].

The individual interaction between the polynucleotides and the nanopore was analyzed from the translocation data as scatter plots showing each translocation event's normalized average current ( $I/I_0$ ) as a function of that event's translocation duration. In the scatter plots, for most of the polynucleotide sequences, the data points were consistently separated into two clusters [19, 34, 36]. It was suggested that the more densely populated cluster represented translocation events initiated by the 5' end whereas the less densely populated cluster represented translocation events initiated by the 3' end [36].

Furthermore, because translocation duration can reflect the molecule's sequence, data points outside of the expected target clusters can reveal sample heterogeneity. The nanopore discriminated a sample of pure dA<sub>100</sub> doped with trace amounts of dC<sub>100</sub> (3 molecules of dC<sub>100</sub> to 97 molecules of dA<sub>100</sub>) [36]. Conversely, the heterogeneity of the same mixture was not visible in the isotope-labeled electrophoretograms [37]. The level of breakdown of a homogeneous sample was also clearly measurable by comparing the translocation profile of freshly prepared sample and the same molecule after storage, dephosphorylation, phosphorylation, or phenol extractions. Chemical integrity investigation with the nanopore requires fewer sample manipulations and has no known length limitations to detect the few variably degraded molecules in a DNA sample, whereas evaluating chemical quality by gel electrophoresis or chromatography is constrained by polynucleotide length.

### **Length discrimination**

Nanopores can also be used to differentiate the length of DNA molecules [26, 27, 38]. Using alpha-hemolysin nanopores, Kasianowicz et al. observed that the number of blockades per minute produced by short DNA molecules was significantly greater than

the number produced by equivalent concentrations of longer molecules [16]. On the contrary, Meller et al. focused on the physics governing the motion of DNA through narrow pores and measured the translocation velocity of ssDNA molecules as a function of their length [38]. They concluded that the velocity of molecules shorter than the pore length depends strongly on length, whereas this velocity is independent of length for molecules longer than the pore length. Synthetic solid-state nanopores have also been used for length differentiation. Li et al. demonstrated that 10-nm silicon nitride pores can discriminate 3-kb and 10-kb dsDNA molecules with a 120-mV bias [25]. The 10-kbp dsDNA takes three times longer to negotiate the pore than the 3-kbp dsDNA at the same voltage bias. Heng et al. also reported the distribution of transients associated with separate measurements of 100 bp, 600 bp, and 1500 bp dsDNA using the 2.4 nm diameter silicon nitride nanopore [26].

Storm further confirmed the previous observations with longer dsDNA molecules and a 10 nm diameter silicon oxide pore [27]. Two sets of experiments were performed, one on 11.5-kbp DNA and one using 48-kbp DNA. For the 48-kbp DNA they found typical translocation times between 1 ms and 2 ms, about 7 times longer than the 150  $\mu$ s to 350  $\mu$ s observed for the 11.5-kbp molecules. This difference is probably caused by the difference in contour length of the two molecules. Considering that the difference in contour length of these two molecules is about a factor of 4, the long molecules thus appear to translocate with a lower average velocity than the short ones. Overall, these observations provide strong evidence that each simple single-level event corresponds to a DNA molecule translocating in a linear fashion through the nanopore under the influence of electrophoretic forces.



### **A.3 Modifications of Nanopore Detection**

#### **Investigation of translocation dynamics**

To interpret the complex signals from translocation events, many researchers have investigated the interactions between molecules, nanopores, and membranes [25-29, 39-47]. Most of their recently published work has shown a good agreement with previous experimental data and demonstrated the potential of such nanopore system not only as a stochastic sensor but also in advancing to DNA sequencing devices [48, 49]. Bates et al. demonstrated that the transport of single DNA molecules can be controlled by varying the transmembrane electric potential during the passage of the molecule [50]. Interactions before and during translocation have been separately investigated to explain two distinct timescales: a slow timescale associated with molecules that enter and bind to the pore and a fast timescale associated with molecules that escape without binding [50, 51]. Consistently, Butler et al. studied the directionality of  $A_{25}C_{50}$  and  $C_{50}A_{25}$  RNA molecules that pass through the pore and observed unique bilevel current blockages that can be inferred to two independent current blockage levels of  $A_{50}$  and  $C_{50}$  [52]. Such translocation phenomena have been further investigated in depth using various synthetic nanopores. Li et al. attributed the spread of events to strands of DNA that are partially folded back on themselves during translocation [25]. As overlapping folded parts of a molecule pass through the pore they increase the current blockade during that part of the event. More confirmation of such folding effects was provided by Storm in a closer inspection of the current data for 48-kbp dsDNA [27]. He suggested that on many occasions, single events consist of one or more plateaus at discrete current levels, and they can be classified into several types including linear straight translocation and

folding-involved translocation.

Subsequently, Heng et al. have discussed the variety of transients and experimentally observed that the level of the blocking current changes during the translocation of short dsDNA molecules [26]. On the contrary, Aksimentiev et al. conducted molecular dynamics simulations of DNA translocation through the nanopore [53]. The simulations indicate that the level of current blockade is correlated to the velocity of the molecule in the pore and with the bulk electrolyte flow accompanying the translocation event. Consequently, they concluded that interactions between the molecule and the pore give rise to a nonuniformity of molecular velocity and electrolyte flow that is manifested as variations in the blocking current during a single translocation. The simulation also shows that hydrophobic interactions between DNA bases and the pore surface can slow down translocation of ssDNA and might favor unzipping of dsDNA inside the pore, which is consistent with the previous calculations [38, 41]. Overall, these efforts may help understand how even a simple homopolynucleotide can cause seemingly complex signals that have so far been accessible only through advanced algorithms [54]. Accordingly, understanding the complex nature of translocation directed the research toward several clever modifications of the system.

### **Discrimination among individual DNA hairpin molecules**

From the measured velocities of translocation through a nanopore, a major factor limiting single-base resolution is the time available to detect current drop by a single nucleotide [55]. A single nucleotide passes through the pore in only a few microseconds, and in that same time interval, only about 100 ions contribute to the difference between bases, which might be easily lost in the noise. At least an order of magnitude more ions

would be required to sufficiently discriminate between single purine and pyrimidine bases. Vercoutere et al. used DNA hairpins to increase the translocation duration of a single molecule of DNA in the alpha-hemolysin channel up to relatively long (milliseconds to seconds) time intervals [56]. Hairpins fold back on themselves to form a blunt end and a double-stranded stem [57]. Their expectation was that a hydrogen-bonded hairpin structure might enter the relatively big vestibule of the channel but would not pass through the alpha-hemolysin pore because of its size until the hairpin structure broke and was released as a single-stranded molecule (Figure A-1a, 1b).

In their experiments, a DNA hairpin with a six-base-pair stem and a four-deoxythymidine loop caused a partial current blockade lasting hundreds of milliseconds, followed by a rapid downward spike, indicating an initial capture of a hairpin stem and simultaneous dissociation of the stem [56]. They also found that single-nucleotide differences between otherwise identical DNA hairpins could produce different signatures that would be classified by a following support vector machine (SVM) [58]. For example, a 5 base pair hairpin with a 4-deoxythymidine loop was discriminated from that with a 3-deoxythymidine loop. Similarly, they reported that each base-pair addition produced a marked increase in average blockade translocation time (Figure A-1c).

### **Detection of complementary polynucleotides from modified nanopore**

By covalently tethering a DNA oligonucleotide molecule near the entrance of the alpha-hemolysin pore, Howorka et al. implemented a biosensor that can distinguish between polynucleotides whose sequence perfectly complements that of the tethered oligomer and those whose sequence does not complement the tethered oligomer [59] (Figure A-2). The principle underlying this sensor is that, when a short complementary

polynucleotide is drawn into the lumen of the nanopore, it is likely to form a DNA duplex with the tethered oligomer producing a current reduction that may last longer than when it does not form a duplex. The complementary polynucleotide stayed tens of milliseconds whereas a polynucleotide that does not complement the tethered oligomer is rapidly translocated, producing an ephemeral but obvious current reduction. They showed that even a single-base mismatch can influence the duration times due to different duplex formation.

Based on these experiments, two different methods were proposed for sequencing an unknown molecule [59]. When an oligonucleotide with an unknown sequence is tethered to the nanopore and analyzed by the application of a series of different free polynucleotides of known sequence, the unknown codon sequence of the tethered molecule can be determined. Alternatively, if an array of nanopores with various known tethered oligonucleotides could be implemented, such an array could replace the surface-mounted microarrays to identify unknown sequence variations in a solution of free polynucleotides. The second method is arguably simpler and more cost-effective than surface-mounted microarrays and thus possesses a potential application in the identification of gene variants or the screening of single-nucleotide polymorphisms (SNPs) in human genes.

### **Translocation of modified analyte polynucleotides**

Although previous attempts to increase translocation duration for improved resolution involve genetically engineered or otherwise modified channels [60, 61], more recent approaches are attaching blocking elements to analytes that otherwise thread through a nanopore quickly [62-65]. The elements are covalently linked to one [62, 65] or

both ends of the polynucleotide forming a dumbbell-shaped DNA-polymer complex [63, 64]. Kasianowicz et al. demonstrated analyte quantitation by using biotinylated single-stranded DNA (bT-DNA) as the pore-permeant polymer [62]. This biotinylated DNA strand can be used for a novel sensor design [66]. When another macromolecule is attached at the other end of this strand, a dumbbell-like molecule can be trapped within the alpha-hemolysin channel, forming a rotaxane (a system of interlocked molecules). It was also suggested that moving this type of dumbbell molecule back and forth through a nanopore might increase the signal to noise ratio of the current blockade and thereby increase the chance of reliably sequencing long strands of DNA with a nanopore [63].

Sanchez-Quesada et al. first demonstrated that a hybrid polymer of neutral poly(ethylene glycol) (PEG) and a negatively charged DNA strand could form rotaxanes by threading the hybrid polymer through the alpha-hemolysin channel. Whereas the PEG chain has a biotin unit at the 5' end, a DNA strand has a hairpin structure or a complementary base-paired DNA segment at the other end. The hairpin structure can also obstruct the transport of the polymer through the alpha-hemolysin channel [56]. They demonstrated that the PEG–DNA hybrid polymer can be locked within the nanopore by the addition of streptavidin (Figure A-3). Once a rotaxane has been formed inside the pore, the relative position of the molecule can be switched simply by controlling the sign and magnitude of the transmembrane potential. By keeping the hybrid polymer inside the nanopore, they showed that this method might be useful for testing the possibility of individual base discrimination in DNA [64]. In a successive study, they manufactured a single alpha-hemolysin-DNA pseudorotaxane, employing DNA molecules that have a long ssDNA segment for analysis and a 12bp terminal hairpin structure for entrance blocking [67]. When threading molecules stop at the pore entrance because of wider

hairpin, they found that a nucleotide is distinguishable between adenine and cytosine at the site 20 nucleotides away from the hairpin edge.

Likewise, Nakane et al. also proposed a nanosensor using a DNA probe with an avidin anchor at the 5' end and a nucleotide sequence designed to noncovalently bind a specific single-stranded oligonucleotide at the 3' end [65]. The 3' end of the DNA molecule is driven through the channel to the other chamber where it can specifically bind to oligonucleotides. On applying the reverse electric potential, the DNA molecule escapes from the pore as it dissociates from the bound oligonucleotide. The time required for this dissociation yields identifying characteristics of the oligonucleotide. Accordingly, they demonstrated that such sensors could discriminate between oligonucleotides differing by a single base and investigate the relationship between dissociation time and hybridization energy. Overall, with aforementioned modifications in detection schemes, it is probable that more detailed information could be harvested from the same electrical signals.

#### **A.4 Conclusion**

For a decade, there have been high expectations for the advent of new and non-conventional methods of DNA sequencing that would replace the Sanger sequencing. The discovery that an electrical voltage gradient can drive RNA or DNA molecules through a nanopore and produce unique signals has opened up the possibility of detecting and characterizing polynucleotide molecules without labeling at very low copy number by using single-channel recording techniques. Although the future of such nanopore devices is still not clear, this approach has been attracting much attention because of the

possibility to make a direct and fast alternative for linear sequencing of long single molecules.

Although the nanopore sequencing technology is among the more promising future techniques currently in development, most applications reviewed here are still at their initial proof-of-principle stage. Given the current state of technology, it is unlikely that we can make conjectures about when such new sequencing techniques will be realized beyond their preliminary stage. In addition, there is no doubt that several years of a long adoption period for these new sequencing technologies will be necessary from laboratory proof-of-concept to development of robust commercial systems [68]. Thus, significant advances in both material processing and experimental methods are still needed to expand applications based on single nanopores. Moreover, the realization of more robust technology will require further development of synthetic nanopores in various materials where unfavorable interaction between molecules and the pore walls would be minimized. However, little is known about the heterogeneity of these structures at nanometer resolution or about their noncovalent interactions with DNA.

Although the empirical and theoretical applications reviewed here may produce valuable information on the analyses of DNA molecules, further investigations are needed to explain the physical basis for characteristic signatures of different current blockage levels and translocation rates. Resolving the different current signatures of individual nucleotides in the nanopore may require better understanding of the factors that regulate polymer translocation through a pore [70]. In addition, scalable computational methods will also be required in the future nanopore sequencing devices for real time discrimination [69, 71]. Alternatively, a more complex, interacting pore could be constructed in different ways that would yield a more easily discernable

electronic signal.



Table A-1. Summary of the statistical translocation properties of six polymers characterized at 25.0°C [34].

Polymer	$I_P$	$t_P$	$\tau_T$
(dA) <sub>100</sub>	0.126 ± 0.012	192 ± 10	55 ± 3
(dC) <sub>100</sub>	0.134 ± 0.010	74 ± 4	15 ± 1
(dA) <sub>50</sub> (dC) <sub>50</sub>	0.128 ± 0.010	136 ± 7	32 ± 2
(dAdC) <sub>50</sub>	0.141 ± 0.011	177 ± 9	38 ± 2
(dC) <sub>50</sub> (dT) <sub>50</sub>	0.140 ± 0.011	137 ± 7	25 ± 1
(dCdT) <sub>50</sub>	0.144 ± 0.012	82 ± 4	91 ± 5

The most probable translocation current,  $I_P$ , the most probable translocation duration,  $t_P$ , and the temporal dispersion of translocation duration,  $\tau_T$ .

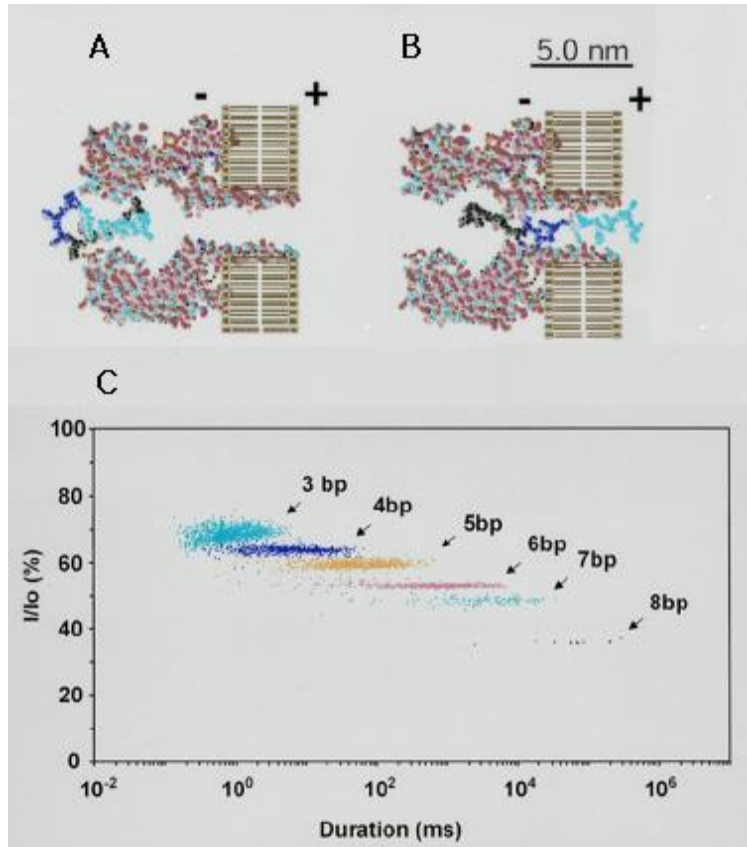


Figure A-1. A molecular model of translocation events [56]. Cross section of the  $\alpha$ -hemolysin heptamer (a) Capture of a 6-bp DNA hairpin in the channel causes an abrupt current reduction (b) Translocation of the DNA through the limiting aperture of the channel. (c) An event diagram for DNA hairpins with 3- to 8-bp stems. Each point represents the duration and amplitude of a current blockade caused by one DNA hairpin captured in the pore vestibule.

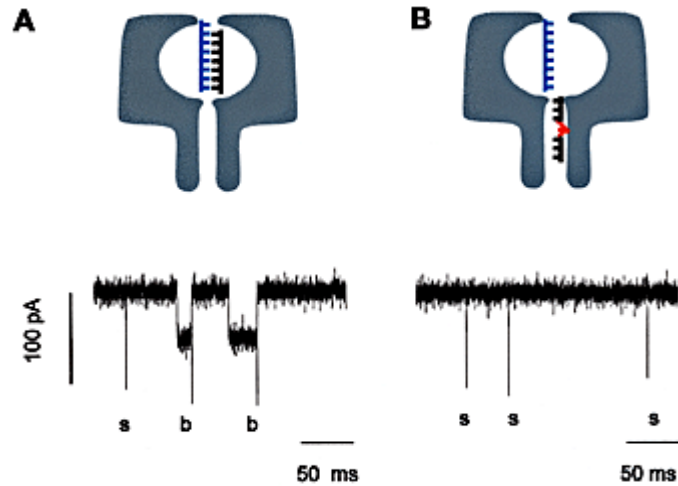


Figure A-2. A single-base mismatch abolishes the binding of an oligonucleotide to a tethered DNA strand within the engineered nanopore [59]. (A) Negative current deflections **b** are individual binding events of oligo-2G (black; 3'-TAAGTGG-5') to the tethered oligo-1 (blue; 5'-CATTACAC-3'). The short downward spike **s** in the trace is a translocation event of oligo-2G that did not bind to the tethered oligonucleotide. (B) Representative trace of the same channel as in (A) after perfusion of the *cis* chamber and the addition of oligo-2C (black with a red peak; 3'-TAACTGG-5'). Only short translocation events **s** were observed.

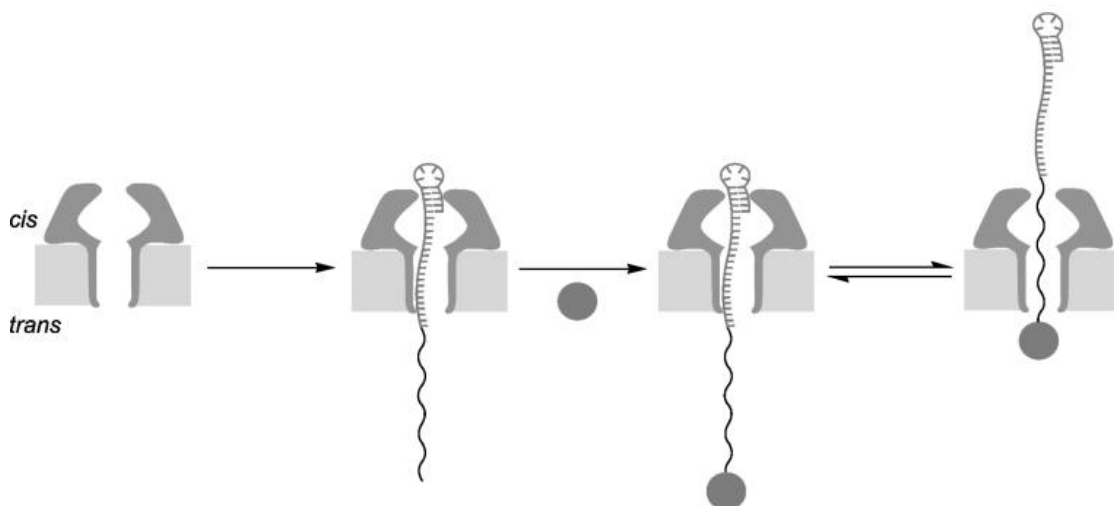


Figure A-3. Schematic representation of the molecular components and processes employed for synthesis of transmembrane protein rotaxanes [64]. (a) System employed for rotaxane formation through capture by streptavidin on the cis side of the pore. (b) Thread molecule with a DNA hairpin for rotaxane formation by capture with streptavidin on the trans side.

## References

1. França, L. T. C., Carrilho, E., and Kist, T. B. L. (2002) A review of DNA sequencing techniques. *Quarterly Reviews of Biophysics* **35**, 169-200.
2. Sanger, F., Nicklen, S., and Coulson, A. R. (1977). DNA sequencing with fluorescent chain-terminating inhibitors. *Proceedings of the National Academy of Sciences, USA*, **74**, 5463.
3. Collins, F. S., Morgan, M. and Patrinos, A. (2003) The human genome project: lessons from large-scale biology. *Science* **300**, 286–290.
4. Nakane, J. J., Akeson, M. and Marziali, A. (2003) Nanopore sensors for nucleic acid analysis. *J. Phys. Condens. Matter*. **15**, R1365-R1393.
5. National Human Genome Research Institute. (2004) Revolutionary Genome Sequencing Technologies — The \$1000 Genome, <<http://grants1.nih.gov/grants/guide/rfa-files/RFA-HG-04-003.html>>.
6. Nyren, P. and Lundin, A. (1985) Enzymatic method for continuous monitoring of inorganic pyrophosphate synthesis. *Anal. Biochem.* **151**, 504-509.
7. Hyman, E. D. (1988) A new method of sequencing DNA. *Anal. Biochem.* **174**, 423-436.
8. Ronaghi, M. (2001) Pyrosequencing sheds light on DNA sequencing. *Genome Res.* **11**, 3-11.
9. Drmanac, S. (1998) Accurate sequencing by hybridization for DNA diagnostics and individual genomics. *Nature Biotechnol.* **16**, 54–58.
10. Drmanac, R. Drmanac, S., Baier, J., Chui, G., Coleman, D., Diaz, R., Gietzen, D., Hou, A., Jin, H., Ukrainczyk, T. *et al.* (2001) DNA sequencing by hybridization with arrays of samples or probes. *Methods Mol. Biol.* **170**, 173–179.
11. Goodwin, P. M., Johnson, M. E., Martin, J. C., Ambrose, W. P., Marrone, B. L., Jett, J. H., and Keller, R. A. (1993) Rapid sizing of individual fluorescently stained DNA fragments by flow cytometry. *Nucl. Acids Res.* **21**, 803–806.
12. Schwartz, D. C. Li, X., Hernandez, L. I., Ramnarain, S. P., Huff, E. J., and Wang, Y. K. (1993) Ordered restriction maps of *Saccharomyces-cerevisiae* chromosomes constructed by optical mapping. *Science* **262**, 110–114.
13. Keller, R. A. Ambrose, W. P., Arias, A. A., Cai, H., Emory, S. R., Goodwin, P. M., and Jett, J. H. (2002) Analytical applications of single-molecule detection. *Anal. Chem.* **74**(11), 316A-324A.
14. Werner, J. H., Cai, H., Jett, J. H., Reha-Krantz, L., Keller, R. A., and Goodwin, P. M. (2003) Progress towards single-molecule DNA sequencing: a one color demonstration. *Journal of Biotechnology* **102**, 1-14.

15. Haab, B. B. and Mathies, R. A. (1999) Single-molecule detection of DNA separations in microfabricated capillary electrophoresis chips employing focused molecular streams *Anal. Chem.* **71**, 5137–45.
16. Kasianowicz, J. J., Brandin, E., Branton, D. and Deamer, D. W. (1996) Characterization of individual polynucleotide molecules using a membrane channel. *Proc. Natl. Acad. Sci. U.S.A.* **93**, 13770-13773.
17. DeBlois, R. W. and Bean, C. P. 1970. Counting and sizing of submicron particles by resistive pulse technique. *Rev. Sci. Instrum.* **41**, 909.
18. Wang, H. and Branton, D. (2001) Nanopores with a spark for single-molecule detection. *Nature Biotechnology* **19**, 622-623.
19. Akeson, M., Branton, D., Kasianowicz, J. J., Brandin, E. and Deamer, D. W. (1999) Microsecond Time-Scale Discrimination Among Polycytidylic Acid, Polyadenylic Acid, and Polyuridylic Acid as Homopolymers or as Segments Within Single RNA Molecules. *Biophys. J.* **77**, 3227-3233.
20. Szabo, I., Bathori, G., Tombola, F., Coppola, A., Schmehl, I., Brini, M., Ghazi, A., De Pinto, V., and Zoratti, M. (1998) Double-stranded DNA can be translocated across a planar membrane containing purified mitochondrial porin. *FASEB* **12**, 495–502.
21. Rostovtseva, T. K., Komarov, A., Bezrukov, S. M. and Colombini, M. (2002) Dynamics of nucleotides in VDAC channels: structure-specific noise generation. *Biophys. J.* **82**, 193–205.
22. Song, J., Midson, C., Blachly-Dyson, E., Forte, M., and Colombini, M. (1998) The topology of VDAC as probed by biotin modification. *J. Biol. Chem.* **273**, 24406–24413.
23. Szabo, I., Bathori, G., Tombola, F., Brini, M., Coppola, A., and Zoratti, M. (1997) DNA translocation across planar bilayers containing *Bacillus subtilis* ion channels. *J. Biol. Chem.* **272**, 25275–25282.
24. Deamer, D. W. and Branton, D. (2002) Characterization of Nucleic Acids by Nanopore Analysis. *Acc. Chem. Res.* **35(10)**, 817-825.
25. Li, J., Gershow, M., Stein, D., Brandin, E. and Golovchenko, J. A. (2003) DNA molecules and configurations in a solid-state nanopore microscope. *Nature Materials* **2**, 611-615.
26. Heng, J. B., Ho, C., Kim, T., Timp, R., Aksimentiev, A., Grinkova, Y. V., Sligar, S., Schulten, K., and Timp, G. (2004) Sizing DNA Using a Nanometer-Diameter Pore. *Biophys. J.* **87**, 2905-2911.
27. Storm, A. J. (2004) Single molecule experiments on DNA with novel silicon nanostructures. Ph.D. Thesis, the Delft University of Technology, Netherlands.

28. Heng, J.B., Aksimentiev, A., Ho, C., Marks, P., Grinkova, Y.V., Sligar, S., Schulten, K., and Timp, G. (2005) Stretching DNA using the electric field in a synthetic nanopore, *Nano Letters*. **5**, 1883-1888.
29. Heng, J.B., Aksimentiev, A., Ho, C., Marks, P., Grinkova, Y.V., Sligar, S., Schulten, K., Timp, G. (2006) The Electromechanics of DNA in a Synthetic Nanopore. *Biophys. J.* **90**, 1098-1106
30. Burns, M. A. Johnson, B. N., Brahmasandra, S. N., Handique, K., Webster, J. R., Krishnan, M., Sammarco, T. S., Man, P. M., Jones, D., Heldsinger, D. *et al.* (1998) An Integrated Nanoliter DNA Analysis Device. *Science* **282**, 484-487.
31. Burns, M. A. (2002) Everyone's a (future) chemist. *Science* **296**, 1818-1819.
32. Song, L., Hobaugh, M. R., Shustak, C., Cheley, S., Bayley, H., and Gouaux, J. E. (1996) Structure of Staphylococcal Alpha-Hemolysin, a Heptameric Transmembrane Pore. *Science* **274**, 1859-1865.
33. Kasianowicz, J.J., Henrickson, S. E., Weetall, H. H. and Robertson, B. (2001) Simultaneous Multianalyte Detection with a Nanometer-Scale Pore. *Anal. Chem.* **73**, 2268-2272.
34. Meller, A., Nivon, L. Brandin, E., Golovchenko, J. and Branton, D. (2000) Rapid nanopore discrimination between single polynucleotide molecules. *Proc. Natl. Acad. Sci. U.S.A.* **97**, 1079-1084.
35. Henrickson, S. E., Misakian, M., Robertson, B. and Kasianowicz, J. J. (2000) Driven DNA Transport into an Asymmetric Nanometer-Scale Pore. *Phys. Rev. Lett.* **85**, 3057-3060.
36. Wang, H., Dunning, J. E., Huang, A. P. –H., Nyamwanda, J. A. And Branton, D. (2004) DNA heterogeneity and phosphorylation unveiled by single-molecule electrophoresis. *Proc. Natl. Acad. Sci. U.S.A.* **101**, 13472-13477.
37. van Houten, V., Denkers, F., van Dijk, M., van den Brekel, M. and Brakenhoff, R. (1998) Labeling efficiency of oligonucleotides by T4 polynucleotide kinase depends on 5'-nucleotide *Anal. Biochem.* **265**, 386–389.
38. Meller, A, Nivon, L. and Branton, D. (2001) Voltage-Driven DNA Translocation through a Nanopore. *Phys. Rev. Lett.* **86**, 3435-3438.
39. Keyser, U.F., Krapf, D., Koeleman, B.N., Smeets, R.M.M., Dekker, N.H., and Dekker, C. (2005) Nanopore Tomography of a Laser Focus, *Nano Letters*. **5**, 2253-2256.
40. Ito, T, Sun, L, and Crooks, R.M. (2003) Observation of DNA transport through a single carbon nanotube channel using fluorescence microscopy. *Chem. Commun.* 1482-1483

41. Sauer-Budge, A.F., Nyamwanda, J.A., Lubensky, D.K. and Branton, D. (2003) Unzipping kinetics of double-stranded DNA in a nanopore. *Phys. Rev. Lett.* **90**, 238101.
42. Nakane, J., Akeson, M. and Marziali, A. (2002) Evaluation of nanopores as candidates for electronic analyte detection. *Electrophoresis* **23**, 2592-2601.
43. Aksimentiev, A. and Schulten, K. (2005) Imaging  $\alpha$ -Hemolysin with Molecular Dynamics: Ionic Conductance, Osmotic Permeability, and the Electrostatic Potential Map. *Biophys J.* **88**, 3745-3761.
44. Fologea, D., Gershow, M., Ledden, B., McNabb, D.S., Golovchenko, J.A. and Li, J. (2005) Detecting single stranded DNA with a solid state nanopore. *Nano Letters.* **5**, 1905-1909.
45. Chen, Z. and Zhang, H. (2005) Mechanisms for formation of a one-dimensional horizontal anodic aluminum oxide nanopore array on a Si substrate. *J. Electrochem. Soc.* **152**, 1-5.
46. Yeh, I.-C. and Hummer, G. (2004) Nucleic acid transport through carbon nanotube membranes. *Proc. Natl. Acad. Sci. U.S.A.* **101**, 12177-12182.
47. Yeh, I. -C and Hummer, G. (2004) Diffusion and electrophoretic mobility of single-stranded RNA from molecular dynamics simulations. *Biophys. J.* **86**, 681-689.
48. Bezrukov, S. M. (2000) Ion Channels as Molecular Coulter to Probe Metabolite Transport. *J. Membrane Biol.* **174**, 1-13
49. Bayley, H. and Martin, C. R. (2000) Resistive-pulse sensing – From microbes to molecules. *Chem. Rev.* **100**, 2575-2594
50. Bates, M., Burns, M. and Meller, A. (2003) Dynamics of DNA Molecules in a Membrane Channel Probed by Active Control Techniques. *Biophys. J.* **84**, 2366-2372.
51. Meller, A. and Branton, D. (2002) Single molecule measurements of DNA transport through a nanopore. *Electrophoresis* **23**, 2583-2591.
52. Butler, T. Z, Gundlach, J. H., and Troll, M. A. (2006) Determination of RNA Orientation during Translocation through a Biological Nanopore, *Biophys. J.* **90**, 190-199.
53. Aleksij Aksimentiev, A., Heng, J. B., Timp, G., and Schulten, K. (2004) Microscopic Kinetics of DNA Translocation through Synthetic Nanopores. *Biophys. J.* **87**, 2086–2097.
54. Bokhari, S. H., and Sauer, J. R. (2005) A parallel graph decomposition algorithm for DNA sequencing with nanopores. *Bioinformatics.* **21**, 889-896.
55. Deamer, D. W. and Akeson, M. (2000) Nanopores and nucleic acids: prospects for ultrarapid sequencing. *Trends Biotech.* **18**, 147-151.



56. Vercoutere, W., Winters-Hilt, S., Olsen, H., Deamer, D., Haussler, D., and Akeson, M. (2001) Rapid discrimination among individual DNA hairpin molecules at single-nucleotide resolution using an ion channel. *Nature Biotechnology* **19**, 248-252.
57. Erie, D. A., Suri, A. K., Breslauer, K. J., Jones, R. A. and Olson, W. K. (1993) Theoretical predictions of DNA hairpin loop conformations: Correlations with thermodynamics and spectroscopic data. *Biochemistry* **32**, 436-454.
58. Burges, C. J. C. (1998) A Tutorial on Support Vector Machines for Pattern Recognition. *Data Mining and Knowledge Discovery* **2**, 121-167.
59. Howorka, S., Cheley, S. and Bayley, H. (2001) Sequence-specific detection of individual DNA strands using engineered nanopores. *Nature Biotechnology* **19**, 636-639.
60. Kasianowicz, J. J., Burden, D. L., Han, L. C., Cheley, S. and Bayley, H. (1999) Genetically Engineered Metal Ion Binding Sites on the Outside of a Channel's Transmembrane  $\beta$ -Barrel. *Biophys. J.* **76**, 837-845.
61. Gu, L., Braha, O., Conlan, S., Cheley, S. And Bayley, H. (1999) Stochastic sensing of organic analytes by a pore-forming protein containing a molecular adapter. *Nature* **398**, 686-690.
62. Kasianowicz, J. J., Henrickson, S. E., Weetall, H. H. and Robertson, B. (2001) Simultaneous Multianalyte Detection with a Nanometer-Scale Pore. *Anal. Chem.* **73**, 2268-2272.
63. Kasianowicz, J. J. (2004) Nanopores: Flossing with DNA. *Nature Materials* **3**, 355-356.
64. Sanchez-Quesada, J., Saghatelian, A., Cheley, S., Bayley, H. and Ghadiri, M. R. (2004) DNA Rotaxanes of a Transmembrane Pore Protein. *Angew. Chem. Int. Ed.* **43**, 3063-3067.
65. Nakane, J., Wiggin, M. and Marziali, A. (2004) A Nanosensor for Transmembrane Capture and Identification of Single Nucleic Acid Molecules. *Biophys. J.* **87**, 615-621.
66. Di Marzio, E. A. and Kasianowicz, J. J. (2003) Phase transitions within the isolated polymer molecule: coupling of the PTM transition to the helix-random coil, the collapse, the adsorption, and the equilibrium polymerization transitions. *J Chem. Phys.* **119**, 6378-6387.
67. Ashkenasy, N., Sanchez-Quesada, J., Bayley, H., and Ghadiri, M. R. (2005) Recognizing a Single Base in an Individual DNA Strand: A Step Toward DNA Sequencing in Nanopores. *Angew. Chem. Int. Ed.* **44**, 1401-1404.
68. Shendure, J., Mitra, R. D., Varma, C. and Church, G. M. (2004) Advanced sequencing technologies: Methods and goals. *Nature Reviews Genetics* **5**, 335-344.

69. Vercoutere, W. and Akeson, M. (2002) Biosensors for DNA sequence detection. *Curr. Opin. Chem. Biol.* **6**, 816-822.
70. Wang, H., Lewis, J. P., and Sankey, O. F. (2004) Band-Gap Tunneling States in DNA, *Phys. Rev. Lett.* **93**, 016401
71. Winters-Hilt, S. and Akeson, M. (2004) Nanopore Cheminformatics. *DNA and Cell Biology* **23**, 675-683.

## **Appendix B**

### **Nanopore Sequencing Technology: Nanopore Preparations**

#### **B.1 Introduction**

Nanometer-scaled pores have been widely investigated for various applications in nanobiotechnology [1, 2]. In particular, researchers have noticed the simple application of nanopores as stochastic sensors for biological molecules, sensors that can identify and quantify analytes based on the passage of current through the pore [3-5]. Given that the scale of such nanopores is comparable with the macromolecules of interest, molecules entering the pore can be easily monitored and analyzed individually. For instance, the diameter of stretched single-stranded DNA (ssDNA) is approximately 1.3 nm whereas the diameter of alpha-hemolysin nanopores is 1.5 nm [6]. Thus, the ssDNA is straightened from its randomly coiled state as it passes through the pore, making nanopores attractive for *de novo* DNA sequencing because they enable nucleotides to be examined in a serial manner.

The principle underlying such nanopore sensors is simple and straightforward. Nanopores can act as Coulter counters [7], in which molecules carrying a net electrical charge are electrophoretically driven through the pore by an applied electric potential.

Molecules then physically block the pore and produce measurable changes of ionic conductivity [8]. This analytical technique has proven effective in determining the concentration and size distribution of particles down to sub-micrometer size [4]. Various nanopore applications have adopted and extended this concept of a Coulter counter, from simple counting of bypassing molecules to analyzing resultant electrical signals for further information such as base discrimination. General uses of such nanopores are summarized in Box 1. A more detailed review on nanopore modifications and applications is explored elsewhere [2].

Up until now, there have been two general approaches to prepare nanopores for DNA analysis. The first approach to produce nanopores was using well known organic membrane proteins, initially done with alpha-hemolysin protein [8]. The alpha-hemolysin pore has been especially well explored and even modified to tailor specific needs for various analytes [5], mainly because of the ideal pore size, low level noise, and well-established preparation protocol [1, 9]. Besides alpha-hemolysin, other membrane-bound proteins of various size and functionality have been also investigated [10-13]. Although the majority of nanopore DNA analysis to date has been done with organic nanopores, various synthetic nanopores have been developed independently using conventional or non-conventional fabrication techniques [14-18].

This chapter will present current nanopore technologies, ranging from organic pore preparations to recent developments of synthetic nanopore fabrications. A more thorough look at the organic pore and its applications can be found in excellent review articles by Nakane et al. [1] and Schmidt [3].

## **B.2 Protein Nanopore Preparation**

### ***The Alpha-Hemolysin Pore***

The first attempts to produce nanopores to detect single DNA polynucleotides were made with alpha-hemolysin, a transmembrane protein, inserted in a lipid bilayer [8, 19]. Alpha-hemolysin is a monomeric 33-kD, 293-residue protein that is secreted by the human pathogen *Staphylococcus aureus*. These monomers self-assemble as a heptamer on synthetic lipid bilayers to form a 1.5 nm diameter aqueous channel through the membrane [6]. Kasianowicz *et al.* found that the alpha-hemolysin pore remains open at neutral pH and high ionic strength [8]. Furthermore, alpha-hemolysin passes a steady ionic current in a detectable range, whereas most membrane channels exhibit unstable 7-current level due to their high sensitivity and spontaneous gating. This steady current flow in a relatively large range ensures low level background electrical noise and thus keeps electrical signals of interest from being hidden by unwanted noise. Crystallography has revealed the structure of the alpha-hemolysin pore to 1.9Å resolution [6]. The resulting image shows a 100 Å long mushroom-shaped homo-oligomeric heptamer of which the pore has a limiting aperture of 1.5 nm (Figure B-1). The transmembrane domain of the channel comprises a 14-strand beta barrel that is primarily hydrophilic inside and hydrophobic outside.

To produce a nanopore, alpha-hemolysin subunits are introduced into a buffered solution that is in contact with a planar lipid bilayer separating solution into two compartments (designated cis and trans). The head of the alpha-hemolysin molecule will be frequently referred to as the cis side, and the stem end as the trans side. The assembled heptameric complex inserts into the cis side of the bilayer to produce a pore that can carry an ionic current of approximately 120 pA with an applied voltage of 120 mV. The lipid

bilayer containing a protein nanopore also influences the function of the pore as an ion channel. Such bilayers are suited for single-channel recording of ionic current and can also be incorporated on a silicon chip for miniaturization and automated operation [20, 21].

### ***Other Organic Pores***

Beyond alpha-hemolysin, the use of other membrane-bound proteins has been investigated as their structures and properties have been studied. Such proteins have been isolated and assembled into artificial lipid bilayers for similar DNA analysis based on DNA translocation. The voltage-dependent mitochondrial ion channel (VDAC), or mitochondrial porin, is a highly conserved monomeric protein located in the mitochondrial outer membrane [22]. Each VDAC channel consisting of a single 30-kDa polypeptide forms an aqueous pore ~3 nm in diameter [23]. Different from alpha-hemolysin pores, the pore size of the VDAC is large enough for double-stranded DNA to translocate through it. VDAC pores are produced in a planar lipid bilayer using a technique similar to that of the alpha-hemolysin method [10].

Bacterial pore proteins are often considered as promising alternatives to alpha-hemolysin. The bacterial ion channels from the membrane vesicles of *Bacillus subtilis* have also been incorporated into phospholipid bilayers. Those ion channels were found to be large enough to translocate 4.2 kb double-stranded plasmids [11]. This translocation yielded a measurable reduction of the ionic current and was verified by the following standard PCR of the trans-chamber solution. Similarly, OmpF porins from the outer membranes of *E. Coli* have been also investigated with regard to transport process [12, 13, 24]. OmpF channels comprise homotrimeric units when reconstituted into planar lipid

bilayers. A diameter of 1.0 –1.2 nm for OmpF pore was proposed, which may be large enough for translocation of single-stranded DNA strands [13]. Although initial work with OmpF has reported detection of water-soluble polymers such as poly(ethylene glycol)s [12], detection of DNA molecules through the pore has not been reported to date [3].

For single-stranded DNA analyses, the use of a nucleic acid binding/channel protein (NAC) has been proposed [25, 26]. Hanss *et al.* identified a 45-kDa protein purified from rat renal brush border membrane (BBM) that binds oligonucleotide sequences [25]. With a single NAC incorporated into an artificial lipid membrane, the presence of oligonucleotides is indispensable for channel activity; the addition of oligonucleotides to the solution activates the gate opening process and yields a detectable current rise with explicit transitions between the closed and open state of the channel. Another application of nanopores used for analyte detection includes the use of very small gramicidin pores, which are mini-proteins composed of two tryptophan-rich subunits. Wright-Lucas and Harding modified gramicidin pores by adding streptavidin binding sites and attaching biotinylated oligonucleotide probes [27]. Given that gramicidin pores are not large enough to translocate even ssDNA directly, a different detection scheme has been adopted using tethered probe molecules. When the sequence between the target and the probe perfectly matches, the ionic current through the gramicidin pores suddenly vanishes, acting as a switch biosensor. Based on this detection mechanism, real-time measurement of the reaction rates of oligonucleotide hybridization has been performed [27].

The reasons to investigate proteins other than alpha-hemolysin are not limited in seeking for various size organic pores. It is very likely that other proteins can be prepared with less laborious procedures and can be used with less modification. Furthermore, other

proteins might exhibit a simpler structure, more robustness, and even better reproducibility [3].

### **B.3 Synthetic Nanopore Fabrications**

Protein nanopores have been serving as functioning electronic sensors to identify single molecules. However, these nanopores in lipid bilayers have limitations in size, variation and stability: proteins are usually labile, the lipid membranes are fragile, the pore diameter is fixed, and the range of safe electrical operation is narrow [15, 16, 28]. Although alpha-hemolysin self-assembles with high fidelity and reproducibility, the physical, chemical, and electrical properties of this protein nanopore pose limitations on the experimental possibilities. For instance, the high temperatures and/or strong denaturants required to maintain polynucleotides in a single-stranded state may disrupt the fragile alpha-hemolysin protein-lipid assembly [17]. In addition, a detailed understanding of the signals obtained empirically has been complicated by the complex charge distribution of the channel. Moreover, considering that a passing molecule is present throughout the 5 nm long pore [6], the conductance changes reflect the presence of up to 10-15 nucleotides altogether that cover the pore length. This duplicated occupation of the pore by multiple nucleotides hinders single nucleotide resolution by changes in electrical signals.

To overcome these difficulties, solid-state synthetic nanopores are being fabricated using various means [28]. The surface properties of a nanopore must be carefully selected to sensitively respond to the molecules that are to be detected [29]. Present state-of-the-art semiconductor fabrication techniques using photolithography are



limited to feature sizes of the order of tens of nanometers [1]. This feature size is larger than would be typically required for detection of individual DNA molecules using the Coulter counter effect. In order to achieve much smaller feature sizes on the scale required for detection of biomolecules, other specialized fabrication techniques must be applied. These techniques will be presented in the following sections and summarized in Table B-1.

### ***Ion Beam Sculpting***

Massive ions with energies of several thousand electron-Volts cause nanometer scale atomic rearrangements when fired at material surfaces. When an ion beam impacts a material surface, an erosion process called sputtering occurs as the ion beam removes atoms from the outermost layers. Li *et al.* prepared a flat Si<sub>3</sub>N<sub>4</sub> surface containing a bowl shaped cavity on one side and let argon ion beams impinge on its opposite surface [30] (Figure B-2a). As material is removed from the flat Si<sub>3</sub>N<sub>4</sub> surface, the surface will ultimately intercept the bottom of cavity, causing a pore to open. By implementing a feedback-controlled ion sputtering system, they could extinguish the erosion process upon breakthrough and thus create a molecular-scale pore as small as 1.8 nm (Figure B-2b). The feedback-controlled system controls other important parameters including sample temperature, beam cycle, and ion beam flux [31, 32].

Although a nanopore can be created from a cavity in the membrane under conditions in which the sputtering erosion process dominates, the ion beam can also be used to stimulate the lateral transport of matter, causing a pre-existing larger pore such as a FIB drilled pore to close [33-35]. At room temperature, the transmitted ion counting rate decreases with increasing ion beam exposure. By changing the sample temperature

or ion beam parameters during the process, it is possible to control whether pore opening or closing dominates. At temperatures below 5°C the sputtering process dominates whereas above 5°C the lateral mass transport process dominates. This ion-beam induced pore closing phenomenon was closely monitored by Mitsui *et al.* and it is argued that matter accretion might be influenced by surface electric field and pore wall geometry [36].

Schenkel *et al.* fabricated a  $\sim 4$  nm wide hole in a silicon nitride membrane with a dual-beam focused ion beam system [18]. Low stress silicon nitride membranes on silicon frames were coated with a very thin gold/palladium layer to minimize charging effects during exposure to ion beams. Initially, a  $\text{Ga}^+$  beam with a high intensity was used to drill from 50 to 600 nm diameter holes. The ion beam was further used to deposit thin a platinum film to slowly close the hole. Similarly, Lo *et al.* recently manufactured nanopores with diameters smaller than 5nm, following the ion beam sculpting technique; however, they used a commercial FIB system equipped with a scanning electron microscope (SEM), which enables a convenient visual feedback control during the size-tuning process [37].

Chen *et al.* suggested that atomic layer deposition (ALD) can afford a finishing step to fine-tune the sizes of nanopores fabricated by ion beam sculpting [29]. ALD from the vapor phase was proved to be highly conformal [38, 39] and as layers are deposited inside the pore, the pore maintains its initial shape and only reduces its size. Because of this uniform and incremental ALD, the sidewalls lining the diameter of a nanopore can be fashioned with atomic precision, shrinking an oversized pore to a preferred smaller diameter. Using this technique, they easily produced nanopores with various diameters based upon the calibrated deposition rate of  $0.099 \pm 0.012$  nm per reaction cycle [29].

Depending on the choice of the coating material, atomic layer deposition also tunes the surface properties of nanopores. Aluminum oxide can be used as the coating material to overcome not only electrostatic repulsion inside the pore but also any electroosmotic flow caused by the sidewalls [29]. Moreover,  $\text{Al}_2\text{O}_3$  is a thermally and chemically stable insulating dielectric material that inhibits direct electron tunneling.

### ***Micromolding***

Saleh and Sohn reported a fundamentally different artificial nanopore that can be fabricated using micromolding techniques [40, 41]. The pore is of length 3  $\mu\text{m}$  and diameter 200 nm and connects two large electrolyte reservoirs. Conventional lithographic techniques are used to create a negative master of the pore and reservoirs that is subsequently cast into a poly(dimethylsiloxane) (PDMS) slab. The master is produced in two steps: first, electron-beam lithography is used to pattern a 200-nm-wide, 200-nm-thick polystyrene line on a silicon substrate, forming the negative of the pore. Next, photolithography is used to create the negatives of the reservoirs. The durability of both polystyrene and SU-8 resists allows for repeated uses of the master. The created master is then cast into a slab of PDMS and electrodes are patterned onto a glass slip anchored by metal deposition. These steps lead to the creation of much larger channels that serve as a detector for large molecules.

The minimum achievable pore diameter with PDMS was reported as small as 80 nm by the recent work by Schmid and Michel [42]. Regardless of its relatively large minimal feature size, the ease and simplicity of micromolding meaningfully enhances the capabilities of various synthetic nanopores for molecular sensing, especially for the coarse sizing of large DNA molecules. Moreover, this approach allows rapid and

reproducible fabrication of sub-micrometer-scale pores and is easy to modify structurally and chemically for various detection applications. Note that arrays of pores can be created by this technique for the simultaneous measurement of many different molecules by relying on common microfabrication techniques.

### ***Latent Track Etching***

In recent studies, a single conical nanopore was created in a polymer substrate by chemically etching the latent track of a single energetic heavy ion [43, 44]. Fabrication of the nanopore by the track-etching technique is based on irradiation of a polymer film with nuclear fragments of total kinetic energy from hundreds to thousands of MeV, and subsequent chemical etching of the latent ion tracks. Each ion produces an etchable track in a polymer foil, forming a one-pore membrane [45]. The size and axial uniformity of the pore can be customized with nanometer precision by controlling the type and concentration of etchant, temperature, and etching duration. To obtain a conical shape, foil was placed between two chambers and etched from one side whereas the other chamber was filled with a stopping, neutralizing medium. The etching then stops when an increase of the current is detected, indicating the moment of break-through. To form a very low density of pores, the flux of nuclear fragments must be controlled on the membrane surface, enabling localization of individual tracks by limiting the contact area of the electrolyte to the membrane. In an alternative way, a single pore can be isolated by physically blocking all other pores with an epoxy coating or a tape mask [46].

Smaller pore diameters and lengths can be attained by using track-etched polycarbonate membranes as templates for gold nanotubules. The nanotubules are formed by plating in gold solution using a chemical reduction process that deposits gold without

the use of an externally applied electric potential [47]. This technique coats the pore walls and membrane faces with a thin (a few nm) layer of gold, decreasing the small opening of the pore to 2 nm.

### ***Electron Beam Induced Fine-Tuning***

More recently, nanopores in various materials were fabricated by advanced nanofabrication techniques such as FIB drilling and E-Beam Lithography, followed by E-beam-assisted fine-tuning techniques [16, 32, 48]. Since Storm *et al.* pioneered the use of high energy electron beams to fine-tune the size of silicon oxide nanopores [48], it has become one of the most popular methodologies in the field to fabricate very small nanopores [37, 49-54]. As a starting material, silicon-on-insulator (SOI) wafers with a top single-crystal-silicon layer of 340 nm were used to fabricate free-standing silicon membranes [48]. A thermal oxidization process was then used to produce a 40 nm thick SiO<sub>2</sub> layer on both sides of membranes. They first opened squares in the SiO<sub>2</sub> mask layer at the top using electron-beam lithography and reactive-ion etching, and subsequently pyramid-shaped holes were etched using anisotropic KOH wet etching. Finally, the holes were thermally oxidized to form a SiO<sub>2</sub> surface layer with a thickness of 40 nm (Figure B-3).

To fine-tune the size of pores with a precision of nanometers, they used a commercial transmission electron microscope (TEM), operated at a voltage of 300kV. The high electron intensity deforms the material surface, modifying the dimensions of the silicon oxide nanopores in a well-controlled way. With appropriate electron beam intensity and initial diameter, pores tend to shrink. The change in pore diameter is monitored in real-time using the imaging mechanism of the microscope, providing a

feedback mechanism to switch off the electron beam so that the material can quench and retain its shape. They reported that the diameter of the pore shrinks at a rate of about 0.3 nm per minute, slow enough to stop at any desired dimension [48].

Keyser *et al.* and Heng *et al.*, independently, adopted a similar strategy to fabricate nanopores in ultra-thin membranes [16, 32, 49, 51]. Heng *et al.*, produced 1-nm diameter pores with subnanometer precision in robust metal oxide semiconductor (MOS)-compatible membranes by using a tightly focused, high-energy electron beam from TEM. Likewise, conventional semiconductor microfabrication techniques allowed Ho *et al.* to form very robust Si, SiO<sub>2</sub>, and Si<sub>3</sub>N<sub>4</sub> free standing membranes that could withstand hundreds of electrolyte immersion and emersion cycles without failing [52]. Successive tightly focused TEM operation resulted in membrane surface decomposition and sputtering, and thus formulated a single nanopore in the membrane. Likewise, Keyser *et al.* produced a 4-nm nanopore in 20-nm thin low-stress silicon nitride membranes [49].

Based on the concept of E-beam fine-tuning, there have been different approaches towards the final pore dimension. Chang *et al.* used a field emission scanning electron microscope (FESEM) as an electron beam source and reported different pore shrinking behavior [54]. They found that pore shrinkage from FESEM E-beam was independent of the initial pore size, and pore enlargement did not occur. In contrast, Lo *et al.* suggested a combinational method of ion beam sculpting and E-beam fine-tuning. They first reduced the diameter of SiN nanopores down to 10 nm or less and then applied a TEM fine-tuning technique to further shrink the pore to 1 nm [37].

This lithography strategy to produce synthetic pores in ultra-thin membranes has obvious superiorities over ion beam sculpting [30] or ion-track etching [43] because of the tight focus and high flux of the electron beam. Direct visual feedback for fine-tuning

and the use of a wide variety of membrane materials are additional advantages [53]. However, despite the extensive use of this technique, the understanding of atomic flow on the surface induced by E-beam impingement is very limited [55]. Storm *et al.* performed a set of TEM tuning experiments with their silicon oxide nanopores and concluded that the shrinking process was driven by surface tension minimization [56]. They also suggested that the electron beam break chemical bonds at low temperature and the surface change into glasslike material, which eventually flows and deforms. Nevertheless, in order to assure a reproducible control of pore tuning on various materials the underlying physics must be further explored.

### ***Inorganic Nanotubes***

Instead of fabricating silicon-based nanopores, Crooks and his collaborators showed that carbon nanotubes might be also suitable for Coulter counting [57]. Figure B-4 illustrates the proposed procedures to prepare single-channel membranes embedding multiwall carbon nanotubes (MWNTs). They first sealed a stretched single MWNT within liquid epoxy. After polymerization, the polymeric monolith containing a MWNT was sectioned using a microtome. The resulting fabricated nanotube channels ranged from 50 to 160 nm in diameter [58, 59].

There are several advantages for using carbon nanotubes over other synthetic nanopores. First, carbon nanotubes exhibit uniform and well-defined chemical and structural properties compared to nanopores treated by high energy beams [60]. Second, various size nanotubes are obtainable ranging from one to hundreds of nanometers; thus it is easier to tailor the channel size to potential analytes. Third, the surface charge of the MWNT channel is known to be effectively zero [61], indicating that electrophoretic

transport becomes simple enough that electrically driven mobility of particles can be predicted without complicated assumptions.

Recently, Fan et al. fabricated silica nanotubes directly integrated with microfluidic systems to form a nanoparticle sensing device [62]. After silicon nanowires were synthesized by  $\text{SiCl}_4$  chemical vapor deposition, the wires were translated into silica nanotubes through an oxidation/etching process with controlled pore size down to 10 nm. Such nanotubes present their unique aspect ratio and provide a new platform for Coulter counter as well with the potential for easy integration into nanofluidic circuits.

#### **B.4 Conclusion**

Despite the evolving developments of synthetic nanopore fabrications, the majority of DNA analyses to date has been performed using alpha-hemolysin protein pores, partly because alpha-hemolysin pores have almost ideal characteristics for detection and identification of ssDNA. However, considering today's technical achievements, it is very likely that synthetic nanopores will replace their biological counterparts in the near future as the underlying complication with synthetic nanopores such as atomic flow phenomena is investigated and clarified. Furthermore, the use of synthetic pores will allow for fully integrated microfabricated systems based on nanopore detection [63], and thus will accelerate an advancing step toward *de novo* sequencing.



Table B-1. Nanopores from various preparation procedures.

	Protein		Synthetic			
	$\alpha$ -hemolysin Assembly	Ion Beam Sculpting	Micro- molding	Latent Track Etching	E-Beam Fine-tuning	Nanotubes
Minimal Pore Diameter reported, nm	1.5 (fixed)	1.8	80	2.0	1.0	50
Membrane Material	Lipid Bilayer	Si <sub>3</sub> N <sub>4</sub>	PDMS	Poly- carbonate	Si, SiO <sub>2</sub> , Si <sub>3</sub> N <sub>4</sub>	Epoxy, Si <sub>3</sub> N <sub>4</sub>
Pore Material	$\alpha$ -hemolysin	Si <sub>3</sub> N <sub>4</sub> , Al <sub>2</sub> O <sub>3</sub>		gold layer		MWNT
Remarks	mass production	size tuning	easy fabrication	conical shape	visual fine-tuning	stable, uncharged

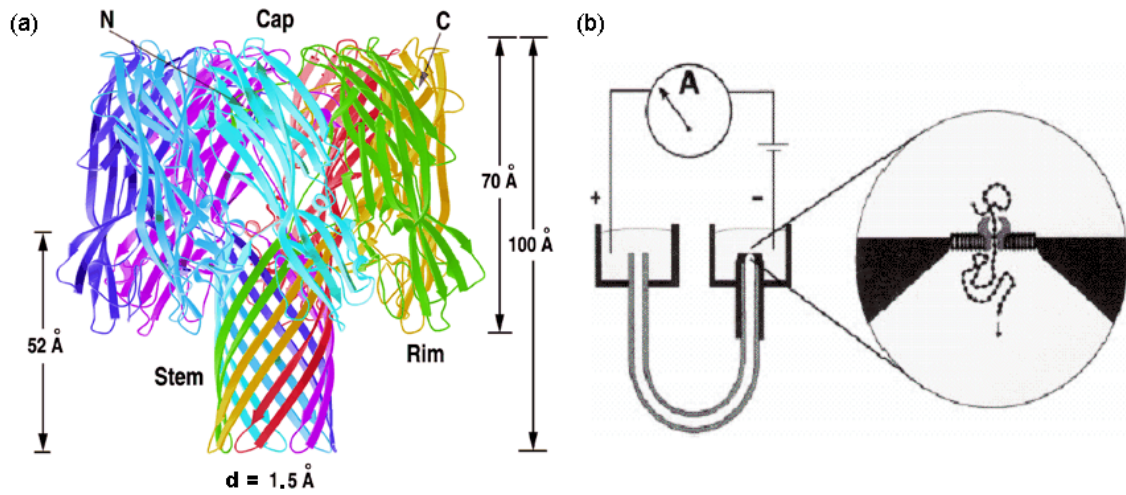


Figure B-1. (a) Ribbon representation of the alpha-hemolysin heptamer. Each color represents a different protomer [6]. (b) An early prototype nanopore device. A U-shaped tube connects two reservoirs filled with ion buffer (left). The reservoirs are connected to an ammeter by Ag-AgCl electrodes. Nucleic acids are driven through the alpha-hemolysin pore by an applied voltage (right) [19].

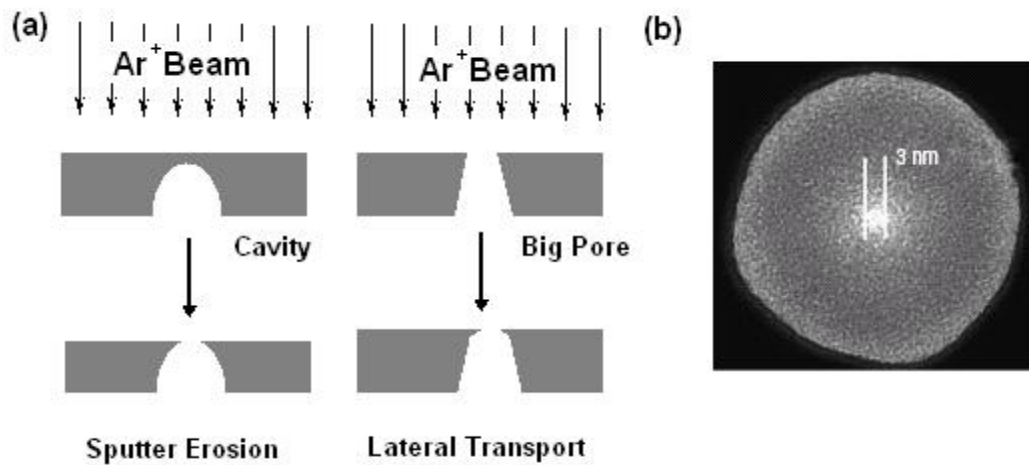


Figure B-2. (a) Ion beam sculpting to make nanopores from a cavity (left) or from a through hole (right). Either sputter erosion or lateral transport processes dominate, depending on the selected conditions used in the ion beam sculpting apparatus [30] (b) TEM image of a 3-nm silicon nitride nanopore produced by ion beam sculpting [14]

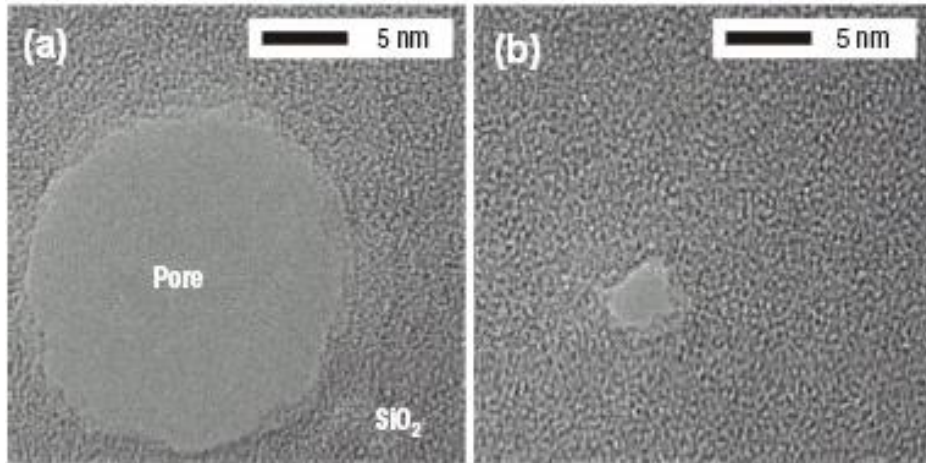


Figure B-3. TEM images of a silicon oxide nanopore of the starting size (a) and the final size (b) during imaging in a TEM microscope. The electron irradiation causes a 6 nm pore to shrink gradually down to a size of about 2 nm [48].

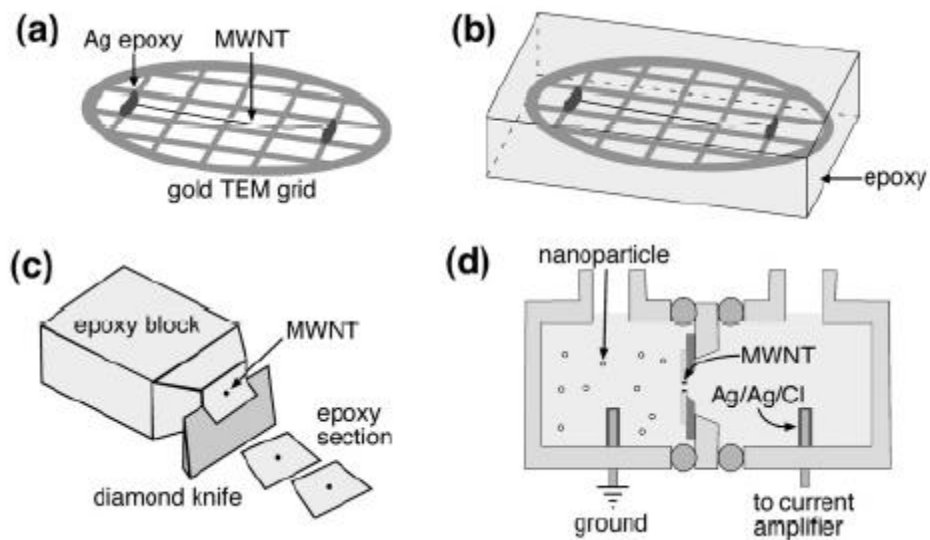


Figure B-4. Illustration of the method for fabrication of MWNT membranes. (a) The extracted nanotube is stretched and affixed to a TEM grid. (b) The MWNT-containing grid is encased within a liquid epoxy. (c) The resulting monolith is sectioned from the epoxy block. (d) A support structure immobilizes the membrane and separates two chambers [59].

## References

1. Nakane, J. J., Akeson, M. and Marziali, A. (2003) Nanopore sensors for nucleic acid analysis. *J. Phys. Condens. Matter.* **15**, R1365-R1393.
2. Rhee, M. and Burns, M. A. (2006) Nanopore sequencing technology: research trends and applications, *Trends Biotechnol.* In press.
3. Schmidt, J. (2005) Stochastic sensors, *J. Mater. Chem.* **15**, 831-840.
4. Bezrukov, S. M. (2000) Ion Channels as Molecular Coulters to Probe Metabolite Transport. *J. Membrane Biol.* **174**, 1-13
5. Bayley, H. and Cremer, P. S. (2001) Stochastic Sensors Inspired by Biology. *Nature*, **413**, 226-230.
6. Song, L., Hobaugh, M. R., Shustak, C., Cheley, S., Bayley, H., and Gouaux, J. E. (1996) Structure of Staphylococcal Alpha-Hemolysin, a Heptameric Transmembrane Pore. *Science* **274**, 1859-1865.
7. DeBlois, R. W. and Bean, C. P. 1970. Counting and sizing of submicron particles by resistive pulse technique. *Rev. Sci. Instrum.* **41**, 909.
8. Kasianowicz, J. J., Brandin, E., Branton, D. and Deamer, D. W. (1996) Characterization of individual polynucleotide molecules using a membrane channel. *Proc. Natl. Acad. Sci. U.S.A.* **93**, 13770-13773.
9. Winters-Hilt, S., (2006) Nanopore Detector based analysis of single-molecule conformational kinetics and binding interactions. *BMC Bioinformatics.* **7**(Suppl 2), S21
10. Szabo, I., Bathori, G., Tombola, F., Coppola, A., Schmehl, I., Brini, M., Ghazi, A., De Pinto, V., and Zoratti, M. (1998) Double-stranded DNA can be translocated across a planar membrane containing purified mitochondrial porin. *FASEB* **12**, 495-502.
11. Szabo, I., Bathori, G., Tombola, F., Brini, M., Coppola, A., and Zoratti, M. (1997) DNA translocation across planar bilayers containing *Bacillus subtilis* ion channels. *J. Biol. Chem.* **272**, 25275-25282.
12. Rostovtseva, T.K., Nestorovich, E.M. and Bezrukov, S.M. (2002) Partitioning of Differently Sized Poly(ethylene glycol)s into OmpF Porin. *Biophys J.* **82**, 160-169.
13. Nestorovich, E.M., Rostovtseva, T.K., and Bezrukov, S.M. (2003) Residue Ionization and Ion Transport through OmpF Channels. *Biophys J.* **85**, 3718-3729.
14. Li, J., Gershow, M., Stein, D., Brandin, E. and Golovchenko, J. A. (2003) DNA molecules and configurations in a solid-state nanopore microscope. *Nature Materials* **2**, 611-615.
15. Wang, H. and Branton, D. (2001) Nanopores with a spark for single-molecule

- detection. *Nature Biotechnology* **19**, 622-623.
16. Heng, J. B., Ho, C., Kim, T., Timp, R., Aksimentiev, A., Grinkova, Y. V., Sligar, S., Schulten, K., and Timp, G. (2004) Sizing DNA Using a Nanometer-Diameter Pore. *Biophys. J.* **87**, 2905-2911.
  17. Chen, P., Gu, J., Brandin, E., Kim, Y., Wang, Q., and Branton, D. (2004) Probing Single DNA Molecule Transport Using Fabricated Nanopores. *Nano Letters* **4**, 2293-2298.
  18. Schenkel, T., Radmilovic, V., Stach, E.A., Park, S.J. and Persaud, A. (2003) Formation of a few nanometer wide holes in membranes with a dual beam focused ion beam system. *J. Vac. Sci. Technol. B.* **21**(6), 2720-2723.
  19. Akeson, M., Branton, D., Kasianowicz, J. J., Brandin, E. and Deamer, D. W. (1999) Microsecond Time-Scale Discrimination Among Polycytidylic Acid, Polyadenylic Acid, and Polyuridylic Acid as Homopolymers or as Segments Within Single RNA Molecules. *Biophys. J.* **77**, 3227-3233.
  20. Mayer, M., Terrettaz S., Giovannardi, L., Stora, T. and Vogel, H. (2003) Functional analysis of ion channels: planar patch clamp and impedance spectroscopy of tethered lipid membranes”, in *Biosensors – A practical approach*, 2nd ed., Oxford University Press, Oxford, UK.
  21. Mayer, M., Kriebel, J. K., Tosteson, M. T. and Whitesides, G. M. (2003) Microfabricated Teflon Membranes for Low-noise Recordings of Ion Channels in Planar Lipid Bilayers. *Biophys. J.* **85**, 2684-2695
  22. Rostovtseva, T. K., Komarov, A., Bezrukov, S. M. and Colombini, M. (2002) Dynamics of nucleotides in VDAC channels: structure-specific noise generation. *Biophys. J.* **82**, 193–205.
  23. Song, J., Midson, C., Blachly-Dyson, E., Forte, M., and Colombini, M. (1998) The topology of VDAC as probed by biotin modification. *J. Biol. Chem.* **273**, 24406–24413.
  24. Danelon, C., Lindemann, M., Borin, C., Fournier, D., and Winterhalter, M. (2004) Channel-Forming Membrane Proteins as Molecular Sensors. *IEEE Transactions on Nanobioscience*, **3**(1), 46-48.
  25. Hanss, B., Leal-Pinto, E., Bruggeman, L. A., Copeland, T. D. and Klotman, P. E. (1998) Identification and characterization of a cell membrane nucleic acid channel. *Proc. Natl Acad. Sci. USA* **95**, 1921–1926.
  26. Leal-Pinto, E., Teixeira, A., Tran, B., Hanss, B., and Klotman, P.E. (2005) Presence of the nucleic acid channel in renal brush-border membranes: allosteric modulation by extracellular calcium. *Am. J. Physiol. Renal. Physiol.* **289**, F97–F106.

27. Wright-Lucas, S. and Harding, M. M. (2000) Detection of DNA via an ion channel switch biosensor *Anal. Biochem.* **282**, 70–79.
28. Deamer, D. W. and Branton, D. (2002) Characterization of Nucleic Acids by Nanopore Analysis. *Acc. Chem. Res.* **35(10)**, 817-825.
29. Chen, P., Mitsui, T., Farmer, D. B., Golovchenko, J., Gordon, R. G., and Branton, D. (2004) Atomic Layer Deposition to Fine-Tune the Surface Properties and Diameters of Fabricated Nanopores. *Nano Letters* **4**, 1333-1337.
30. Li, J., Stein, D., McMullan, C., Branton, D., Aziz, M. J., and Golovchenko, J. A. (2001) Ion-beam sculpting at nanometer length scales. *Nature* **412**, 166-169.
31. Stein, D., McMullan, C. J., Li, J. and Golovchenko, J. A. (2004) Feedback-controlled ion beam sculpting apparatus. *Review of Scientific Instruments* **75**, 900-905.
32. Heng, J.B., Aksimentiev, A., Ho, C., Marks, P., Grinkova, Y.V., Sligar, S., Schulten, K., and Timp, G. (2005) Stretching DNA using the electric field in a synthetic nanopore, *Nano Letters*. **5**, 1883-1888.
33. Stein, D., Li, J. and Golovchenko, J. A. (2002) Ion-Beam Sculpting Time Scales. *Phys. Rev. Lett.* **89**, 27-30.
34. Brongersma, M. L., Snoeks, E., van Dillen, T. and Polman, A. (2000) Origin of MeV Ion Irradiation-Induced Stress Changes in SiO<sub>2</sub>. *J. Appl. Phys.* **88**, 59-64.
35. Fologea, D., Gershow, M., Ledden, B., McNabb, D. S., Golovchenko, J. A., and Li, J. (2005) Detecting single stranded DNA with a solid state nanopore. *Nano Lett.* **5(10)**, 1905-1909.
36. Mitsui, T., Stein, D., Kim, Y. R., Hoogerheide, D., and Golovchenko, J. A. (2006) Nanoscale volcanoes: accretion of matter at ion-sculpted nanopores. *Phys Rev Lett.* **96(3)**, 036102.
37. Lo, C. J., Aref, T., and Bezryadin, A. (2006) Fabrication of symmetric sub-5 nm nanopores using focused ion and electron beams. *Nanotechnology* **17**, 3264–3267
38. Gordon, R.G., Hausmann, D., Kim, E. and Shepard, J. (2003) A Kinetic Model for Step Coverage by Atomic Layer Deposition in Narrow Holes or Trenches. *J. Chem. Vap. Deposition* **9**, 73-78.
39. Hausmann, D. M., Kim, E., Becker, J. and Gordon, R. G. (2002) Atomic Layer Deposition of Hafnium and Zirconium Oxides Using Metal Amide Precursors. *Chem Mater.* **14**, 4350-4358.
40. Saleh, O. A. and Sohn, L. L. (2003) An Artificial Nanopore for Molecular Sensing. *Nano letters* **3**, 37-38.
41. Saleh, O. A. and Sohn, L. L. (2004) Biological Sensing with an On-Chip Resistive Pulse Analyzer. *Proceedings of the 26th Annual International Conference of the IEEE*



*EMBS San Francisco, CA, USA, 2568-2570.*

42. Schmid, H. and Michel, B. (2000) Siloxane Polymers for High-Resolution, High-Accuracy Soft Lithography. *Macromolecules* **33**, 3042-3049.
43. Mara, A., Siwy, Z., Trautmann, C., Wan, J. and Kamme, F. (2004) An Asymmetric Polymer Nanopore for Single Molecule Detection. *Nano Letters* **4**, 497-501.
44. Siwy, Z. and Fulinski, A. (2002) Fabrication of a Synthetic Nanopore Ion Pump. *Phys. Rev. Lett.* **89**, 198103.
45. Heins, E.A., Siwy, Z.S., Baker, L.A., and Martin, C.R.. (2005) Detecting single porphyrin molecules in a conically shaped synthetic nanopore. *Nano Letters*. **5**, 1824-1829.
46. Harrell, C. C., Lee, S. B. and Martin, C. R. (2003) Synthetic Single-Nanopore and Nanotube Membranes. *Anal. Chem.* **75**, 6861-6867.
47. Harrell, C. C., Kohli, P., Siwy, Z. and Martin., C. R. (2004) DNA-Nanotube Artificial Ion Channels. *J. Am. Chem. Soc.* **126**, 15646-15647.
48. Storm, A. J., Chen, J. H., Ling, X. S., Zandbergen, H. W. and Dekker, C. (2003) Fabrication of solid-state nanopores with single-nanometre precision. *Nature Materials* **2**, 537-541.
49. Keyser, U.F., Krapf, D., Koeleman, B.N., Smeets, R.M.M., Dekker, N.H., and Dekker, C. (2005) Nanopore Tomography of a Laser Focus, *Nano Letters*. **5**, 2253-2256.
50. Smeets, R. M., Keyser, U. F., Krapf, D., Wu, M. Y., Dekker, N. H., and Dekker, C. (2006) Salt dependence of ion transport and DNA translocation through solid-state nanopores. *Nano Lett.* **6**(1), 89-95.
51. Heng, J.B., Aksimentiev, A., Ho, C., Marks, P., Grinkova, Y.V., Sligar, S., Schulten, K., Timp, G. (2006) The Electromechanics of DNA in a Synthetic Nanopore. *Biophys. J.* **90**, 1098-1106
52. Ho, C., Qiao, R., Heng, J. B., Chatterjee, A., Timp, R. J., Aluru, N. R. and Timp, G. (2005) Electrolytic transport through a synthetic nanometer-diameter pore. *Proc. Natl. Acad. Sci. U.S.A* **102**, 10445-10450.
53. Chang, H., Kosari, F., Andreadakis, G., Alam, M. A., Vasmatzis, G., and Bashir, R. (2004) DNA-Mediated Fluctuations in Ionic Current through Silicon Oxide Nanopore Channels. *Nano Letters* **4**, 1551-1556.
54. Chang, H., Iqbal, S. M., Stach, E. A., King, A. H., Zaluzec, N. J., and Bashir, R. (2006) Fabrication and characterization of solid-state nanopores using a field emission scanning electron microscope *Appl. Phys. Lett.* **88**, 103109.
55. Wu, M., Krapf, D., Zandbergen, M., Zandbergen, H., and Batson, P. E. (2005)

- Formation of nanopores in a SiN/SiO<sub>2</sub> membrane with an electron beam, *Appl. Phys. Lett.* **87**, 113106.
56. Storm, A. J., Chen, J. H., Ling, X. S., Zandbergen, H. W., and Dekker, C. (2005) Electron-beam-induced deformations of SiO<sub>2</sub> nanostructures *J. Appl. Phys.* **98**, 014307.
  57. Ito, T., Sun, L., Henriquez, R.R., and Crooks, R.M. (2004) A carbon nanotube-based coulter nanoparticle counter. *Acc Chem Res.* **37**(12), 937-945.
  58. Ito, T, Sun, L, and Crooks, R.M. (2003) Observation of DNA transport through a single carbon nanotube channel using fluorescence microscopy. *Chem. Commun.* 1482-1483
  59. Henriquez, R.R., Ito, T., Sun, L., Crooks, R.M. (2004) The resurgence of Coulter counting for analyzing nanoscale objects. *Analyst.* **129**(6), 478-482.
  60. Fan, S., Chapline, M.G., Franklin, N.R., Tomblor, T.W., Cassell, A.M., and Dai, H. (1999) Self-Oriented Regular Arrays of Carbon Nanotubes and Their Field Emission Properties, *Science.* **283**, 512-514.
  61. Sun, L. and Crooks, R. M. (2000) Single Carbon Nanotube Membranes: A Well-Defined Model for Studying Mass Transport through Nanoporous Materials. *J. Am. Chem. Soc.*, **122**, 12340-12345.
  62. Fan, R., Karnik, R., Yue, M., Li, D., Majumdar, A. and Yang, P. (2005) DNA Translocation in Inorganic Nanotubes. *Nano Letters*, **5**, 1633-1637.
  63. Burns, M. A. Johnson, B. N., Brahmasandra, S. N., Handique, K., Webster, J. R., Krishnan, M., Sammarco, T. S., Man, P. M., Jones, D., Heldsinger, D. *et al.* (1998) An Integrated Nanoliter DNA Analysis Device. *Science* **282**, 484-487.
  64. Meller, A., Nivon, L. Brandin, E., Golovchenko, J. and Branton, D. (2000) Rapid nanopore discrimination between single polynucleotide molecules. *Proc. Natl. Acad. Sci. U.S.A.* **97**, 1079-1084.
  65. Wang, H., Dunning, J. E., Huang, A. P. –H., Nyamwanda, J. A. And Branton, D. (2004) DNA heterogeneity and phosphorylation unveiled by single-molecule electrophoresis. *Proc. Natl. Acad. Sci. U.S.A.* **101**, 13472-13477.
  66. Vercoutere, W., Winters-Hilt, S., Olsen, H., Deamer, D., Haussler, D., and Akeson, M. (2001) Rapid discrimination among individual DNA hairpin molecules at single-nucleotide resolution using an ion channel. *Nature Biotechnology* **19**, 248-252.
  67. Howorka, S., Cheley, S. and Bayley, H. (2001) Sequence-specific detection of individual DNA strands using engineered nanopores. *Nature Biotechnology* **19**, 636-639.
  68. Kasianowicz, J. J. (2004) Nanopores: Flossing with DNA. *Nature Materials* **3**, 355-356.

69. Sanchez-Quesada, J., Saghatelian, A., Cheley, S., Bayley, H. and Ghadiri, M. R. (2004) DNA Rotaxanes of a Transmembrane Pore Protein. *Angew. Chem. Int. Ed.* **43**, 3063-3067.
70. Astier, Y., Braha, O., and Bayley, H. (2006) Toward single molecule DNA sequencing: direct identification of ribonucleoside and deoxyribonucleoside 5'-monophosphates by using an engineered protein nanopore equipped with a molecular adapter. *J Am Chem Soc.* **128**(5), 1705-1710.
71. Chang, H., Venkatesan, B. M., Iqbal, S. M., Andreadakis, G., Kosari, F., Vasmatzis, G., Peroulis, D., and Bashir, R. (2006) DNA counterion current and saturation examined by a MEMS-based solid state nanopore sensor. *Biomed. Microdevices.* **8**(3), 263-269